Centre Énergie Matériaux Télécommunications

Real-Time Optical Monitoring System Based on Dispersion-Induced Frequency-to-Time Mapping Concept

By

Afsaneh Shoeib

A thesis submitted in partial fulfillment of the requirements for the degree of

Master of Science, M.Sc.
in Telecommunications

Evaluation Jury

President of the jury and internal examiner	Jinyang Liang Insitut National de la Recherche Scientifique
External examiner	Shulabh Gupta Carleton University
Research Supervisor	José Azaña Insitut National de la Recherche Scientifique

To my parents for their everlasting love

ACKNOWLEDGEMENTS

I am truly honored to have had the opportunity to pursue my Master's degree at INRS-EMT, a journey that was remarkably enriched by the guidance and support I received.

First and foremost, I would like to express my sincere gratitude to my supervisor, Prof. José Azaña for his continued support, encouragement, and insightful guidance. He played a pivotal role in shaping the researcher I am today by challenging my understanding and encouraging me to approach problems from new angles. Besides being inspiring and supportive, José's friendly, calm, reverent, and easygoing attitude made my Master's experience an enjoyable and memorable one. His approach created an atmosphere of trust and encouragement, turning this challenging journey into a rewarding adventure. José, my heartfelt appreciation for all your supports and dedication.

I would like to extend my deepest appreciation to Dr. Reza Maram (from FONEX Data System Inc.) for his patience and unconditional support throughout my Master's journey. His instrumental guidance helped me navigate the various challenges I encountered along the way. I am immensely fortunate to have had the opportunity to work with Reza, whose generosity in sharing his knowledge through countless hours of insightful discussions has been invaluable. My gratitude also extends to Pasquale Ricciardi (from FONEX Data System Inc.) for his support and valuable feedback.

My sincere thanks to the jury members, Prof. Shulabh Gupta from Carleton University and Prof. Jinyang Liang from INRS, who agreed to evaluate this thesis. I also thank the Natural Sciences and Engineering Research Council of Canada (NSERC) and Fonex Data Systems Inc. for financial support.

I am deeply indebted to my friend and colleague Dr. Manuel P. Fernández, for introducing me to the lab facilities and his vital support throughout my experimental work. His insightful comments, constructive suggestions, and valuable feedback have been exceedingly beneficial. Similarly, I extend my heartfelt thanks to my friend, Connor Rowe, for his invaluable collaboration and constant support in the lab. The growth and success of this project owe much to their generous assistance and expert guidance. I also want to thank the other members of Photonic Signals and Systems Group —Dr. Saket Kaushal, Xinyi Zhu, Benjamin Crockett, and Geunweon Lim—for making the workplace brighter and for all the nice moments we have shared together.

Special thanks to my dear friends, Aline Favero and Mohsen Rezaei, who dedicated their precious time to proofread the French summary of this thesis.

Finally, my deepest gratitude goes to my parents, Hasan and Khatoon, for their endless love and kindness. To my siblings, who have always been supportive and heartwarming, even from thousands of miles away. Completing this journey without their unconditional love and support would have been impossible.

ABSTRACT

In today's world, optical networks serve as a cornerstone in the realm of modern communication and data exchange. These networks are crucial for maintaining high standards of quality of service (QoS) and adhering to service-level agreements (SLAs) as required by network service subscribers. Effective management, especially in performance management, is essential to assure signal integrity during transmission, switching, and routing. Traditionally, optical system performance management has relied on fundamental measurements such as optical power, wavelength, and noise levels. These parameters are analyzed using network management software to optimize system efficiency. However, the escalating demand for network bandwidth and advancements in optical technologies have driven data transmission rates on individual wavelength channels to exceed 40 Gb/s. Concurrently, wavelength-division multiplexing (WDM) has gained prominence, combining multiple wavelength channels on a single fiber link to substantially increase system's transmission capacity.

Yet, these high-speed optical signals are increasingly prone to a variety of system impairments. This vulnerability necessitates sophisticated optical signal processing techniques to precisely characterize signal quality and ensure the performance of high-speed optical signals in various modulation formats. Over the last decade, significant research efforts have been directed towards developing optical performance monitoring (OPM) methods for optical systems and networks, marking a major advancement in the field. Despite tremendous advancements in monitoring techniques, there remains a need for methods with faster response times and simpler implementation for successful applications.

Real-time optical monitoring of waveform frequency content with high speed is essential for ensuring reliable network operation and will play a key role in future optical communication systems. Dispersive Fourier transformation or dispersive frequency-to-time (D-FTM) mapping method enables real-time spectral analysis of short isolated pulse-like signals but cannot be applied to continuous waveforms. In this thesis, we propose for the first time a real-time optical monitoring system called RTOM for dynamic spectral analysis of incoming telecommunication data streams over broad frequency bands, employing a periodic temporal sampling and dispersive delay scheme. The periodic temporal sampling unit can be implemented through a EO intensity modulator, such as a Mach-Zehnder modulator (MZM) driven by a periodic radiofrequency (RF) pulse train with a repetition period of T_R. The proposed system's measurement update rate is ultimately limited by the inverse of the sampling period T_R. The sampling pulses have a full-width at half maximum (FWHM) time-width duration of Δt_p, which has to be sufficiently long such that to capture enough data signal information while satisfying the far-field condition for the chosen dispersion. The objective is to conduct a theoretical study and analysis of the proposed scheme, encompassing the derivation of essential design equations and the exploration of inherent trade-offs. We validate our approach through comprehensive numerical simulations as well as experimental demonstrations. A key advantage of our proposed scheme is that it offers orders-of-magnitude improvements in measurement speed (to the MHz update rate level), thus overcoming one of the main drawbacks of present WDM signal monitoring methods (slow update rates in the kHz range). In addition, this system provides a cost-effective approach with in-line integration capability for real-time spectral analysis of any dynamic broadband waveform.

Keywords: Optical monitoring, real-time spectral analysis, temporal sampling, time-frequency mapping, fiber optics, optical dispersion, wavelength-division-multiplexing (WDM)

RÉSUMÉ

Dans le monde d'aujourd'hui, les réseaux optiques constituent une pierre angulaire dans le domaine de la communication moderne et de l'échange de données. Ces réseaux sont cruciaux pour maintenir des normes élevées de qualité de service (QoS) et respecter les accords de niveau de service (SLA) requis par les abonnés des services de réseau. Une gestion efficace, en particulier dans la gestion de la performance, est essentielle pour assurer l'intégrité du signal lors de la transmission, de la commutation et du routage. Traditionnellement, la gestion de la performance des systèmes optiques s'est appuyée sur des mesures fondamentales telles que la puissance optique, la longueur d'onde et les niveaux de bruit. Ces paramètres sont analysés à l'aide de logiciels de gestion de réseau pour optimiser l'efficacité du système. Cependant, la demande croissante en bande passante du réseau et les avancées dans les technologies optiques ont poussé les taux de transmission de données sur des canaux de longueur d'onde individuels à dépasser les 40 Gb/s. Parallèlement, le multiplexage par répartition en longueur d'onde (WDM) a gagné en importance, combinant plusieurs canaux de longueur d'onde sur un seul lien en fibre pour augmenter considérablement la capacité de transmission du système.

Pourtant, ces signaux optiques à haute vitesse sont de plus en plus sujets à une variété de dégradations du système. Cette vulnérabilité nécessite des techniques sophistiquées de traitement des signaux optiques pour caractériser précisément la qualité du signal et assurer la performance des signaux optiques à haute vitesse dans divers formats de modulation. Au cours de la dernière décennie, des efforts de recherche significatifs ont été dirigés vers le développement de méthodes de surveillance de la performance optique (OPM) pour les systèmes et réseaux optiques, marquant une avancée majeure dans le domaine. Malgré des avancées considérables dans les techniques de surveillance, il reste un besoin de méthodes avec des temps de réponse plus rapides et une mise en œuvre plus simple pour des applications réussies.

La surveillance optique en temps réel du contenu en fréquence des formes d'onde avec une grande vitesse est essentielle pour assurer un fonctionnement fiable du réseau et jouera un rôle clé dans les futurs systèmes de communication optique. La transformation de Fourier dispersive ou la méthode de cartographie fréquence-temps dispersive (D-FTM) permet une analyse spectrale en temps réel de signaux pulsés isolés courts mais ne peut pas être appliquée à des formes d'onde continues. Dans cette thèse, nous proposons pour la première fois un système de surveillance optique en temps réel appelé RTOM pour l'analyse spectrale dynamique des flux de données de télécommunication entrants sur de larges bandes de fréquences, en utilisant un échantillonnage temporel périodique et un schéma de retard dispersif. L'unité d'échantillonnage temporel périodique peut être mise en œuvre par l'intermédiaire d'un modulateur d'intensité EO, tel qu'un modulateur Mach-Zehnder (MZM) piloté par un train d'impulsions radiofréquence (RF) périodique avec une période de répétition de T_R. Le taux de mise à jour des mesures du système proposé est ultimement limité par l'inverse de la période d'échantillonnage T_R. Les impulsions d'échantillonnage ont une durée de largeur à mi-hauteur (FWHM) de Δt_p, qui doit être suffisamment longue pour capturer assez d'informations sur le signal de données tout en satisfaisant la condition de champ lointain pour la dispersion choisie. L'objectif est de conduire une étude théorique et une analyse du schéma proposé, comprenant la dérivation des équations de conception essentielles et l'exploration des compromis inhérents. Nous validons notre approche à travers des simulations numériques complètes ainsi que des démonstrations expérimentales. Un avantage clé de notre schéma proposé est qu'il offre des améliorations de la vitesse de mesure, avec des taux de mise à jour atteignant le niveau des MHz. Cela surpasse l'un des principaux inconvénients des méthodes de surveillance des signaux WDM actuelles, caractérisées par des taux de mise à jour lents, se situant dans la gamme des kHz. De plus, ce système fournit une approche rentable avec la capacité d'intégration en ligne pour l'analyse spectrale en temps réel de toute forme d'onde large bande dynamique.

Mots-clés: Surveillance optique, analyse spectrale en temps réel, échantillonnage temporel, cartographie temps-fréquence, optique de fibre, dispersion optique, multiplexage par répartition en longueur d'onde (WDM)

Système de surveillance optique en temps réel basé sur le concept de cartographie fréquence-temps induite par dispersion

SOMMAIRE RÉCAPITULATIF

Cette section fournit un bref résumé des motivations de ce projet de master. Elle vise à introduire l'importance de la recherche menée sur le développement de méthodes de surveillance de la performance optique (OPM) dans les réseaux de fibres optiques. Un système de surveillance du spectre optique en temps réel, à la fois novateur et simple, compatible avec l'analyse spectrale dynamique des signaux de données de télécommunication, est proposé et développé. Ceci est suivi par une présentation des concepts et des principes opérationnels sous-jacents au système proposé. Ce résumé se termine par la présentation des résultats expérimentaux et une brève conclusion décrivant les avantages du système proposé.

0.1. Revue de context

Au cours de la dernière décennie, la communication par fibre optique a connu une croissance exponentielle, stimulée par une demande croissante pour une capacité supérieure afin de répondre à l'augmentation du trafic internet. Cette poussée a nécessité des avancées telles que la technique de multiplexage par répartition en longueur d'onde (WDM) et les amplificateurs à fibre dopée à l'erbium (EDFA), permettant la transmission simultanée de multiples flux de données sur une seule fibre. La Fig. 1 illustre la tendance actuelle dans les télécommunications à augmenter la bande passante d'une fibre optique unique en réduisant l'espacement entre les canaux et en augmentant les taux de transmission des données [1].

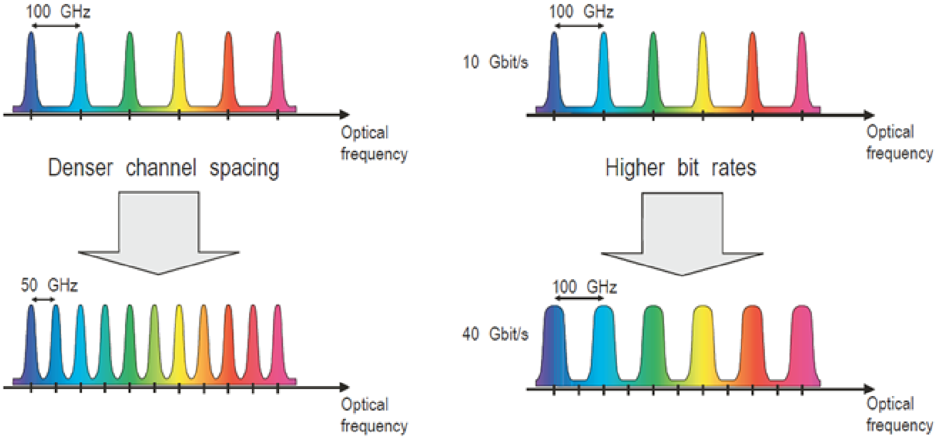

Fig. 1 La tendance dans les télécommunications pour répondre aux besoins en bande passante [1].

Malgré ces progrès technologiques, la complexité croissante du réseau introduit des défis dans la gestion des interruptions de service, des écarts de paramètres et dans l'assurance de la fiabilité du réseau. Au fur et à mesure que les réseaux de fibres optiques évoluent pour supporter des débits de données plus élevés et devenir plus dynamiques, l'importance d'une surveillance en temps réel et précise devient primordiale. Les dispositifs OPM traditionnels manquent de la capacité de fournir des aperçus en temps réel de l'état physique du réseau, conduisant à une sous-utilisation des ressources réseau. Ainsi, les technologies OPM avancées sont cruciales pour améliorer l'efficacité et la fiabilité des réseaux optiques de la prochaine génération.

Les techniques OPM doivent être rapides, précises, sensibles et capables de fonctionner sur plusieurs canaux avec une faible puissance d'entrée. Elles doivent également pouvoir surveiller simultanément plusieurs dégradations, s'adapter à divers débits de données et formats de modulation, tout en restant rentables sans impacter le fonctionnement normal du réseau. Dans ce travail de recherche, l'accent est mis sur la surveillance du spectre optique, qui implique la mesure de la puissance, de la présence et de la longueur d'onde des canaux WDM, comme le montre la Fig. 2. La puissance optique à une longueur d'onde spécifique est un paramètre fondamental dans tout réseau de fibres. Cette puissance peut diminuer considérablement en raison de facteurs tels que l'atténuation de la fibre et les pertes à divers points tels que les connecteurs de fibres, les épissures, les coupleurs ou en cas de rupture de la fibre [2]. La surveillance d'autres paramètres ou dégradations dépend de la mesure de la puissance optique. Dans les systèmes WDM, des informations concernant la puissance de chaque canal sont nécessaires pour égaliser dynamiquement la puissance à travers un mécanisme de rétroaction, assurant ainsi une performance stable du système [3]. De même, la mesure de la longueur d'onde fournit des informations cruciales sur le positionnement précis du signal optique au sein de son canal désigné. En fournissant des données en temps réel sur ces paramètres essentiels, l'OPM permet aux opérateurs de réseau de maintenir une performance optimale, de minimiser les temps d'arrêt, de réduire les coûts d'exploitation et de maintenance du réseau, et de gérer efficacement les complexités inhérentes aux réseaux de fibres optiques modernes. Les caractéristiques souhaitables d'une technique OPM donnée dépendent de divers facteurs, incluant le type de réseau optique où le module OPM sera déployé, la nature et l'étendue des dégradations dans le réseau, les débits de données, les coûts d'implémentation, et le niveau d'intelligence prévu pour être intégré dans les modules OPM. Certaines caractéristiques communes que l'on attend typiquement des techniques OPM incluent un temps de réponse rapide, la transparence par rapport au débit de données et au format de modulation, la rentabilité, etc.

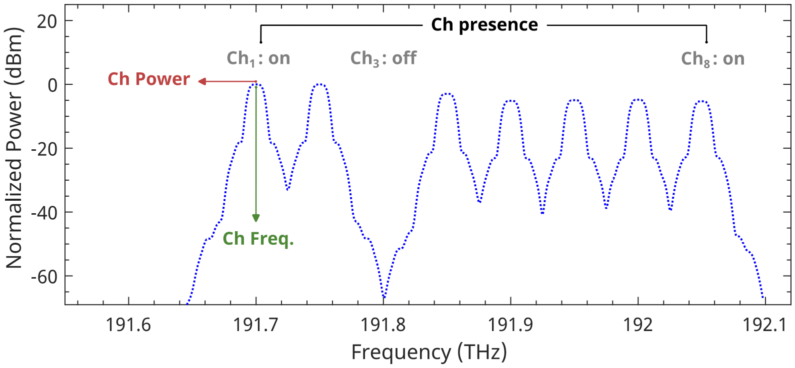

Fig. 2 Trace de l' analyseur de spectre optique des données transmises utilisée comme forme d'onde de référence pour obtenir des informations sur le signal telles que la puissance des canaux WDM, leur présence et leur longueur d'onde.

0.2. Transformation de Fourier dispersive

Les fondements de la transformation de Fourier dispersive, ou la cartographie fréquence-temps dispersive (D-FTM), sont basés sur l'analogie entre la diffraction de Fresnel et la dispersion temporelle, également connue sous le nom de dualité espace-temps [4]. En optique libre, la transformée de Fourier du profil transversal d'une onde peut être dérivée dans le contexte de la propagation en champ lointain. La dualité espace-temps permet un processus similaire dans le domaine temporel. Une fois qu'un signal donné se propage à travers un milieu présentant une certaine quantité de dispersion d'ordre deux, également appelée dispersion de vitesse de groupe (GVD), par exemple une fibre optique, le spectre de fréquence du signal lancé à l'entrée est directement cartographié le long du domaine temporal [5-7]. Ce processus est illustré dans la Fig. 3. Divers types de milieux dispersifs ont été utilisés pour l'implémentation de la D-FTM [7]. L'élément dispersif le plus simple et le plus couramment utilisé est les fibres monomodes (SMFs), présentant une GVD relativement modeste (~17 ps/nm/km à 1550 nm) [8, 9]. Les fibres compensatrices de dispersion (DCFs) peuvent fournir des valeurs de GVD plus élevées (par exemple, 120 ps/nm/km à 1550 nm) [10, 11], et les réseaux de Bragg à fibre à chirp linéaire (LC-FBGs) offrent une alternative compacte attrayante avec une grande quantité de GVD [7, 12, 13].

Un milieu dispersif peut être modélisé comme un système linéaire invariant dans le temps (LTI), avec sa fonction de transfert définie comme suit [5]:

$$H(\omega) = |H(\omega)|\exp(-j\phi(\omega)) \tag{1}$$

où $|H(\omega)|$ et $\phi(\omega)$ représentent respectivement l'amplitude et la réponse en phase spectrale du milieu dispersif à la fréquence angulaire ω. Sous l'approximation de la dispersion d'ordre deux, où les termes de phase au-dessus du second ordre sont négligés dans la largeur de bande spectrale d'intérêt, la fonction de transfert $H(\omega)$ prend la forme [5, 6]:

$$H(\omega') \cong |H(\omega)| \exp(-j\phi_0) \exp\left(-j\dot{\phi}_0\omega'\right) \exp\left(-j\frac{1}{2}\ddot{\phi}_0\omega'^2\right) \tag{2}$$

Où ϕ_0 est la constante de phase, $\dot{\phi}_0$ est le retard de groupe, and $\ddot{\phi}_0$ est le GVD. La D-FTM fonctionne lorsque le GVD est suffisamment fort, c'est-à-dire $|\ddot{\phi}| \gg \Delta t_p^2/2\pi$, où Δt_p est la durée totale du signal d'entrée. Dans une première approche, on peut considérer que le retard de groupe dépend linéairement de la fréquence dont la pente définit le GVD d'ordre deux, $\ddot{\phi}$. La caractéristique de retard de groupe du milieu fait que les différentes composantes fréquentielles du signal d'entrée se déplacent à des vitesses différentes, permettant à chaque composante spectrale d'être mappée sur un délai temporel différent à la sortie du milieu dispersive [5]. Ainsi, sous la condition d'inégalité $|\ddot{\phi}| \gg \Delta t_p^2/2\pi$, qui est également connue sous le nom de condition de Fraunhofer temporel ou de champ lointain temporel, le signal de sortie devient proportionnel à une réplique mise à l'échelle du spectre de fréquence (transformée de Fourier) du signal d'entrée, à l'exception d'un facteur de phase quadratique dépendant du temps [5]. Spécifiquement, le spectre de fréquence du signal est mappé le long du domaine temporel, avec une relation de mappage fréquence-temps donnée par [5]:

$$\omega = \frac{t}{\ddot{\phi}_0} \tag{3}$$

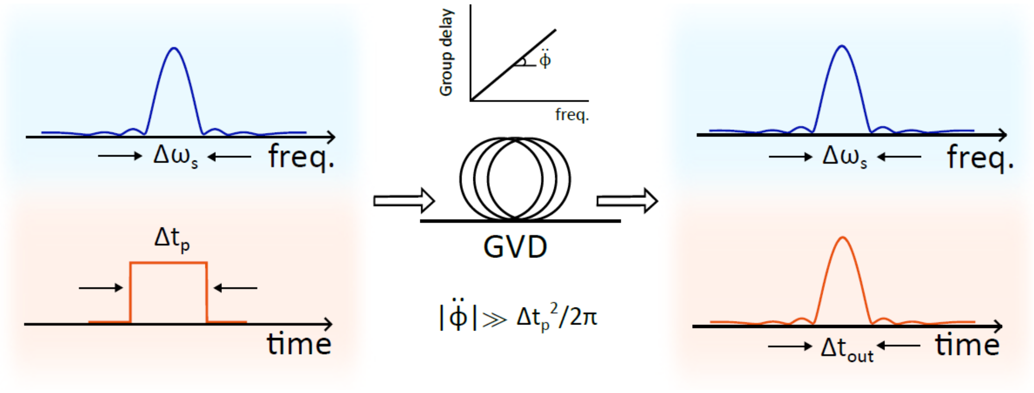

Fig. 3 Schéma illustrant la conversion fréquence-temps au sein d'un milieu dispersif.

Bien que le principe de la D-FTM ait été largement utilisé dans divers domaines de la science et de l'ingénierie, tels que la spectroscopie en temps reel [14], l'interférométrie [15, 16], la réflectométrie [17], la détection de spectre micro-ondes à haute vitesse [18], la métrologie et l'imagerie ultra-rapides [19, 20], et bien d'autres [6], son application pour la surveillance des signaux de données télécom n'a pas encore été explorée. Le principal défi réside dans la contrainte inhérente de la D-FTM d'analyser uniquement des formes d'onde de durée limitée dans le temps (Δt_p) (par exemple, des formes d'onde de type impulsion femtoseconde/picoseconde), imposée par la nécessité de la condition de champ lointain. En conséquence, cette méthode n'est pas adaptée pour l'analyse de signaux continus, tels que les flux de données de télécommunication. Cependant, dans ce travail, nous introduisons une approche simple mais innovante pour surmonter cette limitation, permettant l'utilisation efficace de la D-FTM pour l'analyse de signaux continus, dont les détails seront élaborés dans la section suivante.

0.3. Schéma proposé pour la surveillance du spectre optique

Dans ce travail, nous proposons un système de surveillance optique en temps réel (RTOM) basé sur des composants linéaires simples et pratiques de la fibre optique qui exploitent la D-FTM pour la surveillance en temps réel des signaux multiplexés par division de longueur d'onde dense (DWDM). Pour surmonter la limitation intrinsèque de la D-FTM, nous proposons d'incorporer un module de troncature temporelle conçu adéquatement avant le processus de cartographie fréquence-temps. Ce module sélectionne périodiquement une courte section du signal de données de télécommunication continu à chaque période de temps déterminée par modulation électro-optique (EO). Le schéma du design proposé pour le système RTOM est présenté dans la Fig. 4.

Il est composé de trois unités principales, à savoir (i) une unité d'échantillonnage temporel périodique, (ii) un élément dispersif de vitesse de groupe, et (iii) un dispositif de photodétection à haute vitesse. L'unité d'échantillonnage temporel périodique peut être mise en œuvre à travers des modulateurs d'intensité EO, tels qu'une configuration de modulateur Mach-Zehnder (MZM) [59]. Le signal de données dynamique entrant, désigné dans ce travail comme le signal sous test (SUT), est un signal de données télécom DWDM. Ce SUT peut englober à la fois les signaux montants et descendants au sein d'un lien de télécommunication, et est supposé être limité en bande avec une bande passante totale dénotée par $\Delta\omega_s$, comprenant toutes les canaux de longueur d'onde transmis à travers le lien. Dans l'analyse menée ici, nous supposons que le SUT couvre au moins la bande C entière sans perte de généralité. La durée temporelle du signal n'est soumise à aucune contrainte supplémentaire (par exemple, le SUT peut être infiniment long). Le SUT est d'abord échantillonné/tronqué en utilisant un MZM piloté par un train d'impulsions radiofréquence (RF) périodique avec une période de répétition de T_R, avant que la D-FTM soit effectuée. Les impulsions d'échantillonnage ont une durée de largeur à mi-hauteur (FWHM) de Δt_p, qui doit être suffisamment longue pour capturer assez d'informations sur le signal de données tout en satisfaisant la condition de champ lointain pour le GVD choisi. La bande passante du modulateur d'amplitude détermine la durée minimale en plein largeur des impulsions d'échantillonnage. Par la suite, le signal échantillonné se propage à travers l'unité dispersive de vitesse de groupe, mappant ainsi dans le temps le spectre de fréquence de chaque section de signal tronquée le long de la fenêtre d'analyse temporelle correspondante, chacune avec une durée ne dépassant pas la période d'échantillonnage T_R.

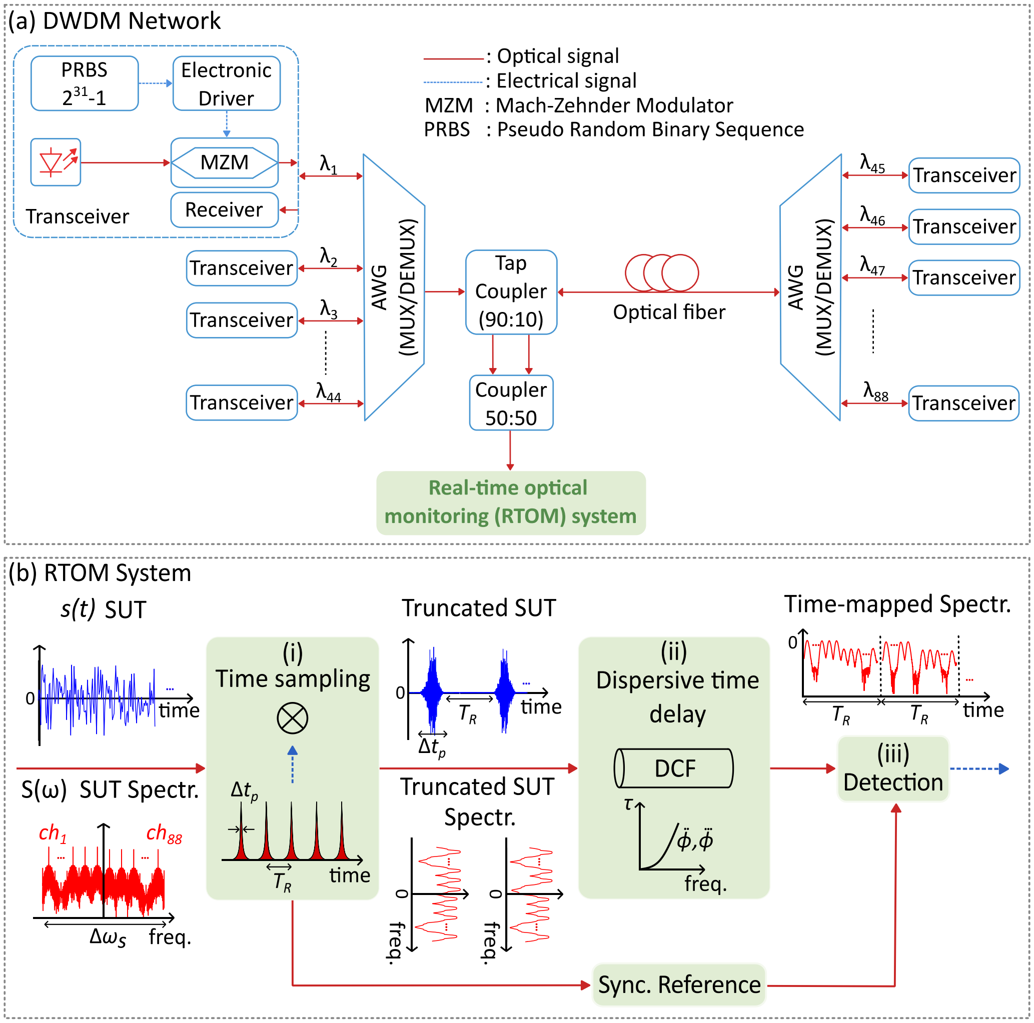

Fig. 4 (a) Un réseau DWDM. (b) Schéma du design proposé pour le système de surveillance optique en temps réel (RTOM).

Le système produit une forme d'onde en temps réel qui suit les spectres des SUT tronqués consécutifs mappés le long d'un créneau de durée T_R, qui est capturé avec un seul photodétecteur (PD) à haute vitesse attaché à un oscilloscope en temps réel (RTO). Deux figures de mérite pertinentes du système RTOM sont la résolution de fréquence réalisable et la bande passante de mesure. Considérant la loi de cartographie fréquence-temps, pour obtenir une résolution de fréquence cible $\delta\omega_r$, le système de détection RTOM doit être capable de capturer les formes d'onde temporelles de sortie avec une résolution d'au moins $\delta t_r \approx |\ddot{\phi}| \times \delta\omega_r$. La résolution $\delta\omega_r$ doit être suffisamment étroite pour discerner deux canaux DWDM adjacents dans le système analysé. De même, le spectre temporel mappé en sortie de chacune des sections échantillonnées du SUT s'étend sur une durée temporelle Δt_{out} comme suit :

$$\Delta t_{out} \approx \Delta\omega_s \times |\ddot{\phi}| \tag{4}$$

Une condition de conception fondamentale est que la période d'échantillonnage T_R doit être plus longue que la durée temporelle du spectre mappé dans le temps de chaque portion de SUT échantillonnée pour éviter le chevauchement entre les sections mappées consécutivement, c'est-à-dire, $T_R > \Delta t_{out}$. Le taux de mise à jour des mesures du système est ultimement limité par l'inverse de la période d'échantillonnage T_R. Cette période est directement proportionnelle à la magnitude du coefficient de dispersion et peut être personnalisée pour relâcher les exigences de la bande passante de détection. En particulier, $\delta t_r \approx |\ddot{\phi}| \times \delta\omega_r$ implique que l'on peut utiliser une bande passante de photodétection plus faible (δt_r plus long) en utilisant une plus grande quantité de dispersion ($|\ddot{\phi}|$) tout en maintenant la même résolution de fréquence. Cependant, il y a deux compromis essentiels à considérer. Le premier est que le spectre mappé dans le temps couvre un Δt_{out} plus large à mesure que la quantité de GVD augmente. Par conséquent, T_R doit être plus long pour séparer les sections mappées consécutivement, ce qui se traduit par un taux de mise à jour des mesures correspondant réduit. De plus, augmenter la dispersion dégrade également la gamme dynamique de la forme d'onde de sortie car chaque spectre mesuré est mappé sur une durée temporelle plus longue avec une intensité locale correspondamment plus faible. Ici, la gamme dynamique fait référence à la différence entre le maximum du signal et le minimum du signal juste au-dessus du plancher de bruit du système.

0.4. Résultats de simulations théoriques et numériques

0.4.1. Modélisation du système RTOM

Le modèle de simulation a été implémenté en utilisant la plateforme de simulation numérique MATLAB. Un flux de données WDM couvrant toute la bande C de télécom optique avec un espacement de canal de presque 50 GHz est considéré ici. Les canaux WDM sont modélisés comme non cohérents et asynchrones, ce qui signifie que les signaux sur chaque canal ne sont pas nécessairement en phase et ont un retard aléatoire les uns par rapport aux autres. Pour la génération de signal, 25000 symboles d'une séquence de bits pseudo-aléatoire binaire de 2^{31}-1 (PRBS) avec un débit de 25 Gb/s sont utilisés pour piloter le MZM de chacun des émetteurs WDM. Ce processus crée un signal non retour à zéro en modulation d'intensité (NRZ-OOK). La limitation de bande passante de l'émetteur est également considérée en utilisant un filtre passe-bas gaussien d'ordre quatre (LPF) avec une bande passante électrique de $0.8 \times bit\ rate$. L'unité d'échantillonnage temporel est mise en œuvre en utilisant un MZM électro-optique de 10 GHz polarisé à $V_\pi = 5\ \mathrm{V}$, tandis que les non-idéalités du MZM telles que le rapport d'extinction fini et la limitation de bande passante sont également prises en compte. En utilisant un générateur de formes d'onde arbitraires (AWG), des impulsions courtes sont générées périodiquement pour échantillonner le SUT. Les impulsions d'échantillonnage sont de forme gaussienne avec une largeur à mi-hauteur (FWHM) de temps de $\Delta t_p = 100\ \mathrm{ps}$ et une périodicité de T_R. Le spectre mappé dans le temps de chacun des SUT évalués couvre temporellement une certaine durée de sortie, Δt_{out}. En supposant le GVD maximal comme $\ddot{\phi} = \Delta t_p^2/2\pi = 1591.55\ \mathrm{ps}^2/\mathrm{rad}$, la durée temporelle de la forme d'onde de sortie est obtenue comme $\Delta t_{out} \approx 44\ \mathrm{ns}$. La valeur de la période d'échantillonnage temporel doit être supérieure à cet intervalle de temps, c'est-à-dire, $T_R > \Delta t_{out}$. Ainsi, la période d'échantillonnage est fixée à $T_R = 200\ \mathrm{ns}$ dans cette analyse. L'unité de retard dispersive est mise en œuvre en utilisant une fibre compensatrice de dispersion (DCF) pour fournir la quantité de dispersion d'ordre deux requise, dictée par la condition de conception dans $|\ddot{\phi}| \geq \Delta t_p^2/2\pi$. L'unité DCF est conçue pour correspondre à un paramètre de dispersion de $D =$ -16.8 ps/nm.Km et une pente de dispersion de $S =$ -0.058 $\mathrm{ps/nm^2.Km}$ [21]. La forme d'onde de sortie est capturée avec une photodiode à avalanche (APD) plus oscilloscope, la mise en œuvre impliquant un sous-ensemble récepteur optique APD (ROSA). L'APD-ROSA consiste en une APD et un amplificateur transimpédance (TIA). Il est supposé que l'APD a un gain de $\mathrm{M} = 10$ et sa bande passante à 3 dB est modélisée comme un filtre passe-bas Bessel d'ordre quatre. Le bruit de l'APD composé de bruit thermique et de bruit de grenaille avec un courant sombre de

$I_d = M \times 3 \times 10^{-9}$ A est également émulé. L'APD a une sensibilité minimale de -34 dBm et une surcharge maximale de -5 dBm. Le TIA est modélisé par un filtre passe-bas Butterworth d'ordre un ayant une transimpédance en courant alternatif de $Z_t = 2500\ \mathrm{ohm}$ ainsi qu'une densité de bruit de courant d'entrée équivalente de $IN = 7.5\ \mathrm{pA}/\sqrt{\mathrm{HZ}}$ [22]. Nous considérons ici les bandes passantes de l'APD et du TIA identiques pour simplifier, et nous référons à toutes les deux comme PD-BW par la suite. La perte d'insertion totale (IL_{max}) du système est attribuée à plusieurs composants: 4 dB du MUX/DEMUX, 10 dB du coupleur à prélèvement, 3 dB du coupleur 50/50, 3.5 dB du MZM, et 6.3 dB de la DCF pour une longueur d'environ ~80 Km.

0.4.2. Résultats de simulation

La Fig. 5 montre comment différents paramètres du système influencent la plage dynamique de la forme d'onde temporelle de sortie, définie comme la différence entre les niveaux maximum et minimum du signal juste au-dessus du plancher de bruit du système. La plage dynamique a été estimée ici en supposant un ratio de couplage de 100 % pour le coupleur.

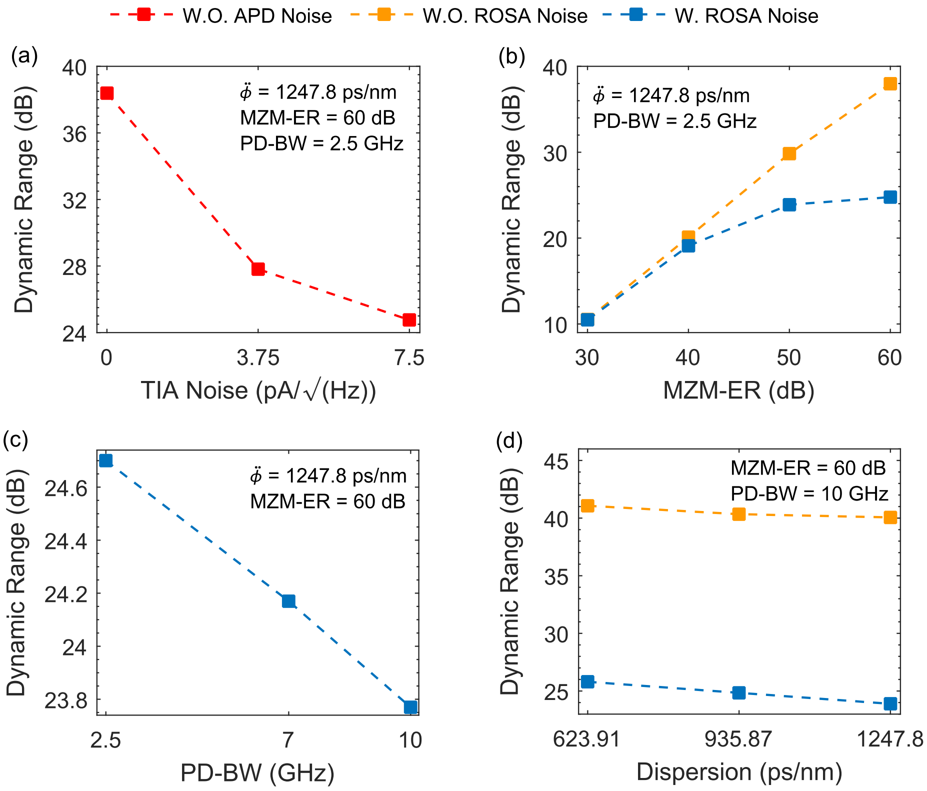

Fig. 5 L'influence de divers paramètres du système, y compris (a) le bruit du TIA, (b) le MZM-ER, (c) le PD BW, et (d) la valeur de dispersion du module DCF, sur la plage dynamique de la forme d'onde temporelle de sortie.

À partir de la Fig. 5(a), on peut déduire que le bruit du TIA joue un rôle crucial concernant la plage dynamique, de sorte que l'augmentation de la densité de courant de bruit d'entrée équivalente du TIA peut diminuer significativement la plage dynamique. Cet effet est attribué au bruit du TIA qui établit le plancher de bruit du système de photodétection (le bruit de l'APD est négligeable par rapport au bruit du TIA). Par conséquent, plus le TIA ROSA a de bruit, plus le plancher de bruit du système de photodétection est élevé, et plus la plage dynamique est limitée. La Fig. 5(b) souligne la relation entre le MZM-ER et la plage dynamique. Nous pouvons voir qu'une augmentation du MZM-ER conduit à une amélioration de la plage dynamique. En tenant compte du bruit du ROSA, la plage dynamique se sature autour de MZM-ER = 40 dB. L'effet du PD-BW est également illustré dans la Fig. 5(c). Étant donné la relation entre le bruit d'entrée équivalent du TIA et le PD BW, l'élargissement du BW amplifie le bruit d'entrée équivalent, réduisant ainsi la plage dynamique. Enfin, la Fig. 5(d) montre l'impact de l'augmentation de la dispersion introduite par la DCF sur la plage dynamique. L'augmentation de la dispersion dégrade la plage dynamique de la forme d'onde de sortie puisque chaque spectre mesuré est mappé sur une durée plus longue avec une intensité locale correspondante plus faible. Bien que cette réduction de la plage dynamique soit évidente, elle n'est pas aussi prononcée que les effets des autres paramètres.

Nous avons obtenu les paramètres de conception optimaux pour le système RTOM, incluant $\ddot{\phi} = 1591.55\ \mathrm{ps}^2/\mathrm{rad}$, MZM-ER = 40 dB, et PD-BW = 2,5 GHz, par des simulations numériques. Le système a ensuite été conçu pour une condition optimisée. À cette fin, nous avons conçu un SUT d'entrée spécifique pour démontrer la capacité unique du système RTOM à capturer en temps réel les changements survenant le long du signal d'entrée aussi rapidement qu'à l'échelle de la nanoseconde. Le tableau 1 documente ces modifications en détail. La Fig. 6 montre les formes d'onde de sortie du système RTOM, qui sont les spectres mappés dans le temps pour cinq échantillons consécutifs du SUT d'entrée, comparés à leurs formes d'onde de référence correspondantes. Chacun des spectres mappés s'étend sur une seule période d'échantillonnage temporel de 200 ns.

Table 1 Modification introduite aux canaux WDM au cours de chaque période d'analyse.

Analysis Period	Deactivated *C*hannels	Power Reduced *C*hannels	Power Reduction Amount (dB)
Sample 1 ($\boldsymbol{T_{R1}}$)	Ch_8, Ch_{55}	Ch_5, Ch_{10}	-10, -5
Sample 2 ($\boldsymbol{T_{R2}}$)	Ch_{65}, Ch_{85}	Ch_{20}, Ch_{50}	-7, -3
Sample 3 ($\boldsymbol{T_{R3}}$)	Ch_{35}, Ch_{36}	Ch_{40}, Ch_{70}	-7,-3
Sample 4 ($\boldsymbol{T_{R4}}$)	Ch_2, Ch_7	Ch_{25}, Ch_{30}	-10, -7
Sample 5 ($\boldsymbol{T_{R5}}$)	Ch_{26}, Ch_{86}	Ch_1, Ch_{88}	-5, -3

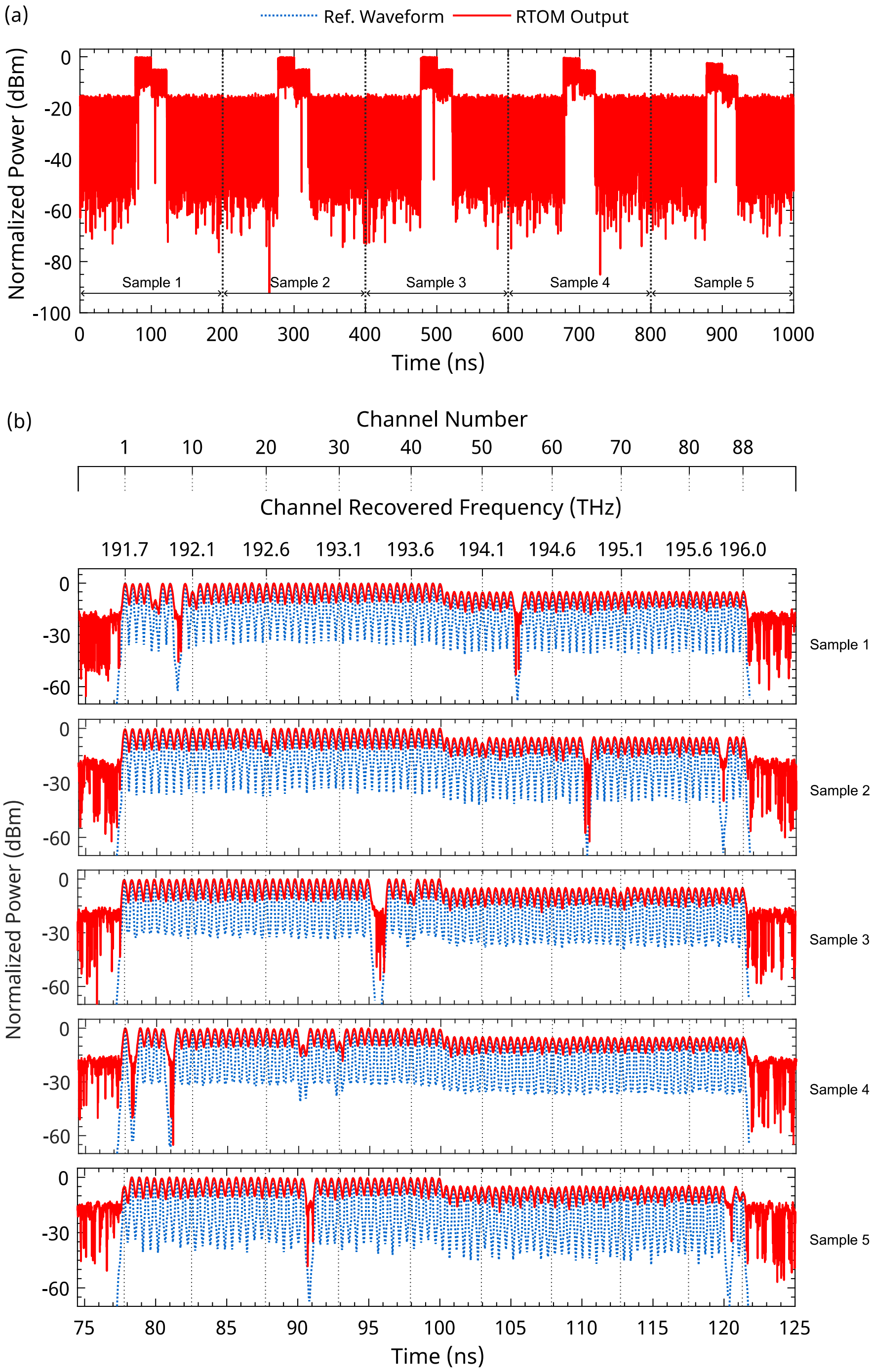

Fig. 6 Simulation numérique démontrant la performance du système RTOM lors de l'analyse d'un SUT d'entrée changeant dynamiquement qui varie à chaque période d'analyse. (a) Sortie globale du système pour le SUT variable, (b) Sortie du système pour chacun des cinq échantillons consécutifs.

On peut observer que la forme d'onde temporelle de sortie et la forme d'onde de référence sont en accord remarquable, prouvant la capacité du système à suivre avec précision et à refléter tous les changements introduits dans le SUT.

Nous illustrons la polyvalence du RTOM pour analyser des formats de modulation cohérente, tels que la modulation d'amplitude en quadrature (QAM), couramment utilisée dans les systèmes de communication optique à haute capacité. Le RTOM est plus efficace à des débits binaires plus élevés. Un seul échantillon d'un signal à taux de symboles plus élevé capture plusieurs symboles consécutifs, fournissant au schéma RTOM plus d'informations sur le signal de données. De plus, les systèmes à haute capacité ont une bande passante par canal plus élevée (~100 GHz). La capacité à résoudre des canaux de fréquence plus larges implique que le RTOM peut être conçu pour offrir une résolution de fréquence plus détendue, nécessitant moins de quantité de dispersion. La Fig. 7 présente l'analyse numérique pour le premier échantillon d'un signal 16-QAM de 100 Gb/s, couvrant toute la bande C avec un espacement de canal de 100 GHz et ~30 GHz de bande passante par canal. La quantité de dispersion est réglée à $\ddot{\phi} = 795.77\ \mathrm{ps}^2/\mathrm{rad}$. Les résultats rapportés corroborent que l'analyse RTOM est agnostique au format de modulation et au taux de symboles, tant que la bande passante par canal du signal de données est dans la résolution de fréquence de conception.

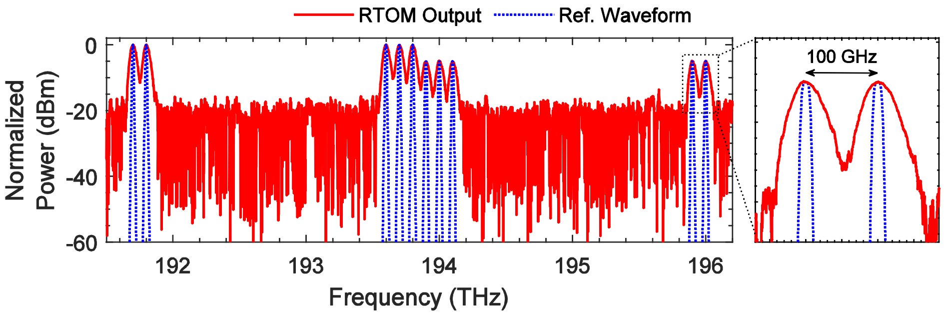

Fig. 7 Trace RTOM obtenue pour le SUT avec un format de modulation cohérente de 16-QAM et un débit binaire de 100 Gb/s, couvrant toute la bande C.

Pour explorer les capacités du RTOM dans des scénarios à débit binaire plus élevé (c'est-à-dire dépassant significativement 100 Gb/s), nous avons également mené une analyse sur un signal de données 16-QAM de 400 Gb/s avec un espacement de canal de 200 GHz à travers toute la bande C. La Fig. 8 présente le résultat du RTOM. Dans ce cas, le SUT est généré en utilisant 40000 symboles obtenus à partir d'une PRBS de longueur $2^{31} - 1$. Les débits binaires plus élevés impliquent typiquement des canaux de fréquence plus larges. Cet aspect joue en faveur de notre conception car elle nécessite une résolution de fréquence plus détendue. Le besoin d'une résolution plus élevée est directement lié à la quantité de dispersion requise dans le système – plus la résolution nécessaire est fine, plus la dispersion nécessaire est grande. Cependant, avec des canaux de fréquence plus larges associés à des débits binaires plus élevés, notre système peut fonctionner efficacement avec une quantité de dispersion plus faible. Par conséquent, la quantité de dispersion est maintenant encore réduite à $\ddot{\phi} = 477.46\ \mathrm{ps^2/rad}$. Cela réduit la complexité et (potentiellement) le coût du système, tout en atteignant toujours la performance désirée en termes d'analyse spectrale et de surveillance. De plus, avec cette dispersion réduite, le spectre mappé dans le temps de sortie de chaque section échantillonnée du SUT s'étend sur une durée temporelle plus courte (dénommée Δt_{out}). En termes pratiques, cela signifie que le système RTOM peut effectuer l'analyse du spectre du signal optique cible à un rythme plus rapide, améliorant ainsi son adéquation pour les applications de surveillance en temps réel où la vitesse est un facteur critique. Ce résultat démontre la capacité du système à surveiller et analyser avec précision des signaux avec des schémas de modulation complexes et des débits de données élevés, confirmant ainsi son applicabilité à des scénarios cohérents à haute capacité.

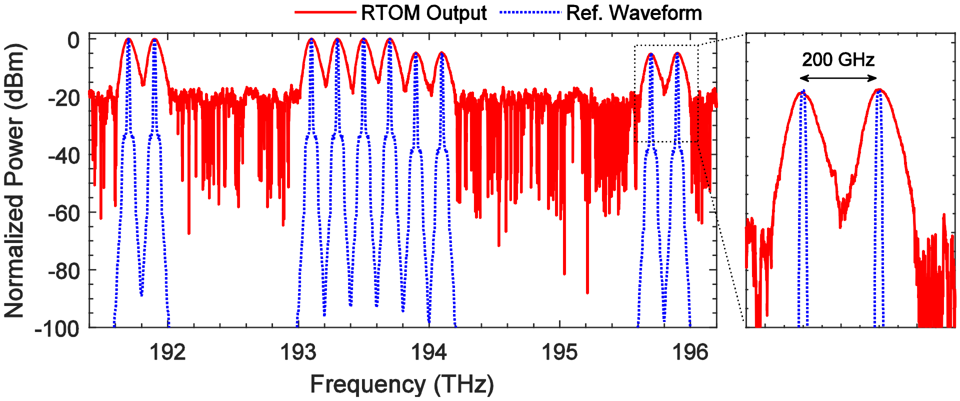

Fig. 8 Trace RTOM obtenue pour le SUT avec un format de modulation cohérente de 16-QAM et un débit binaire de 400 Gb/s, couvrant toute la bande C.

0.5. Résultats expérimentaux

Le dispositif expérimental utilisé pour les expériences de preuve de concept est montré dans la Fig. 9. Le dispositif du système est organisé en trois sections principales: le SUT, le module de transmission et le système RTOM. Le système RTOM est composé d'un MZM de 10 GHz avec un taux d'extinction d'environ 45 dB, piloté par un train d'impulsions d'échantillonnage avec une largeur de temps de $\Delta t_p = 100\ \mathrm{ps}$ générée à partir d'un générateur de formes d'onde arbitraires de 92 GSa/s (AWG, Keysight M8196A), et une fibre compensatrice de dispersion (DCF) avec une dispersion de $\ddot{\phi} = -1328\ \mathrm{ps/nm}$. Le système de détection consiste en un APD-ROSA de 7-GHz connecté à un RTO de 28 GHz (Agilent DSO-X 92804A). Les flux de données sont des signaux pseudo-aléatoires de séquence de bits (PRBS) non retour à zéro en modulation d'intensité (NRZ-OOK). Un laser à onde continue (CW) réglable fonctionnant dans la bande C (IDPHOTONICS CoBrite), un générateur de signaux de données et un émetteur-récepteur optique de petit format (SFP) ont été utilisés pour générer le SUT avec des débits binaires et des formats de modulation variés, incluant le modulateur Mach-Zehnder (MZM) et le laser modulé directement (DML). Pour moduler la forme d'onde de test sur les canaux du laser CW réglable, un MZM de 40 GHz piloté par un autre canal du AWG de 92-GSa/s a été employé. Le flux de données a été encodé simultanément sur les canaux laser CW en utilisant un seul MZM pour la commodité expérimentale. Les canaux du générateur de signaux de données avec le format MZM et l'émetteur-récepteur optique avec le format de modulation DML ont été combinés et amplifiés en utilisant un Amplificateur à Fibre Dopée à l'Erbium (EDFA PriTel). Ce signal a ensuite été fusionné avec deux autres canaux générés par le laser CW. Un EDFA a ensuite été utilisé pour amplifier les signaux combinés, formant le signal de données DWDM qui sert de SUT. Pour produire un SUT plus réaliste, ce signal de données DWDM amplifié a été en outre transmis à travers une fibre monomode de 2 km (module de transmission). Un analyseur de spectre optique (OSA) à haute résolution a été utilisé pour obtenir la forme d'onde de référence. Pour une comparaison plus significative, nous avons effectué un post-traitement du signal sur les résultats acquis. Spécifiquement, les réponses en fréquence de l'OSA ont été lissées en utilisant une convolution de masque gaussien pour atteindre une bande passante de résolution de 12.5 GHz.

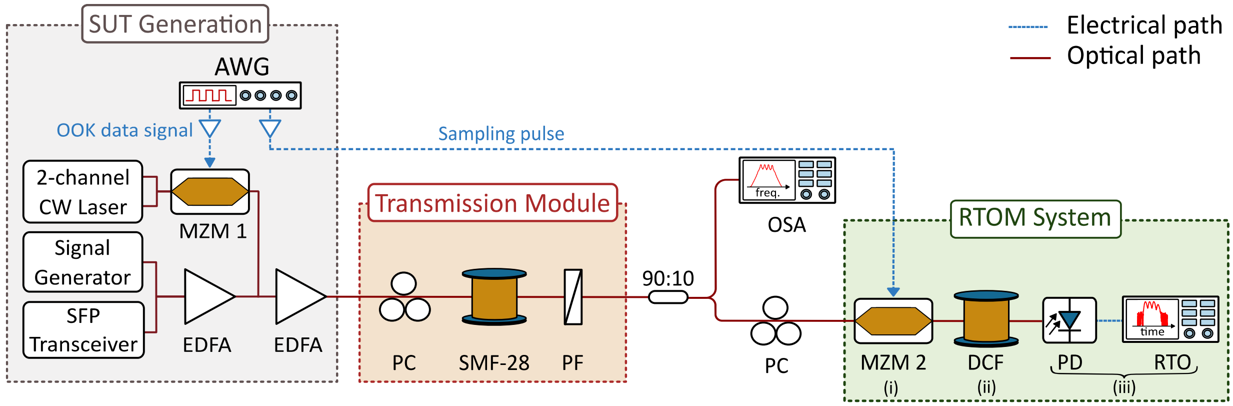

Fig. 9 Dispositif expérimental.

Les encarts montrent la génération du signal et le système RTOM. SUT: signal under test, AWG: arbitrary waveform generator, MZM: Mach Zehnder modulator (MZM 1: 40 GHz, MZM 2: 10 GHz), SFP: small form factor pluggable optical transceiver, EDFA: erbium doped fiber amplifier, PC: polarization controller, SMF-28: single mode fiber, PF: polarization filter, OSA: optical spectrum analyzer, DCF: dispersion compensating fiber, PD: photodetector, RTO: real-time oscilloscope.

De plus, les formes d'onde temporelles de sortie du système RTOM ont été filtrées à travers un filtre passe-bas gaussien. Ce processus de filtrage était nécessaire pour éliminer le bruit provenant du RTO de 28 GHz et pour adapter les formes d'onde à une largeur d'impulsion de 100 ps. Il convient également de mentionner que dans les résultats expérimentaux, l'effet de dispersion d'ordre trois (TOD) a été ignoré en raison de son impact négligeable.

Nous démontrons d'abord la fonctionnalité du système RTOM pour le suivi en temps réel simultané des multiples canaux de longueur d'onde d'un SUT possédant différents débits de données et formats de modulation sur une large bande de fréquence, couvrant presque entièrement la bande C complète. Nous analysons un signal (SUT_1) composé de quatre flux de données situés à quatre longueurs d'onde centrales différentes, à savoir, $\lambda_1 = 1565\ \mathrm{nm}$, $\lambda_2 = 1556.1\ \mathrm{nm}$, $\lambda_3 = 1541.33\ \mathrm{nm}$, $\lambda_4 = 1540.94\ \mathrm{nm}$ avec un format de modulation de DML pour Ch_2 et MZM pour les autres canaux. Les flux de données ont une longueur de $2^{13} - 1$, $2^{31} - 1$, $2^{13} - 1$, et $2^{31} - 1$ à des débits de données de 1 Gb/s, 25 Gb/s, 1 Gb/s et 25 Gb/s, respectivement (les spécifications sont résumées dans le Tableau 2). Le SUT_1 est introduit dans le système RTOM, où il subit un échantillonnage temporel utilisant les paramètres suivants: période $T_\mathrm{R} = 208.7\ \mathrm{ns}$ et largeur de temps $\Delta t_p = 100\ \mathrm{ps}$. La durée de largeur de temps des impulsions d'échantillonnage doit être suffisamment longue pour capturer assez d'informations sur le signal de données tout en satisfaisant la condition de champ lointain pour le GVD choisi. Comme démontré ici, les informations spectrales souhaitées peuvent être récupérées avec précision même lorsque la largeur de l'impulsion d'échantillonnage est considérablement plus courte que la période de bit des flux de données dans le SUT. Remarquez que la largeur de temps d'échantillonnage est environ 10 fois plus courte que la période de bit des flux à 1 Gb/s. La Fig. 10 montre la trace spectrale mesurée à l'aide du système RTOM, obtenue à partir de l'averaging de 239 échantillons consécutifs, où elle est comparée à la forme d'onde de référence obtenue à partir d'une mesure spectrale utilisant un OSA conventionnel avec une bande passante de résolution de 0.1 nm (~12.5 GHz). L'averaging de 239 échantillons consécutifs donne un taux de rafraîchissement de "208.7 ns×239", soit ~50 µs. L'encart fournit un regard plus attentif à la forme d'onde de sortie spécifiquement pour Ch_3 et Ch_4, séparés par 50 GHz. Il y a un assez bon accord entre le spectre mappé dans le temps obtenu et le spectre de référence, démontrant la précision et la fiabilité du système RTOM pour l'analyse du spectre optique sur une large gamme de fréquences et avec une résolution suffisante. Le système présente une gamme dynamique d'environ 18 dB. Le résultat obtenu confirme également la polyvalence du système dans l'analyse de divers formats de modulation et spécifications, incluant différents débits de données.

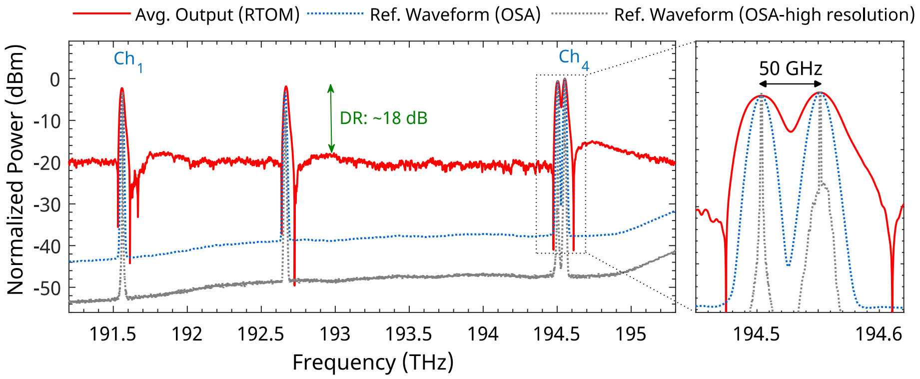

Fig. 10 Trace RTOM correspondant au SUT couvrant presque toute la bande C.

Le SUT se compose de quatre canaux WDM fonctionnant avec différents formats de modulation (Ch_2: DML, les autres canaux: MZM) et débits de données (Ch_1-Ch_3: 1 Gb/s, Ch_2-Ch_4: 25 Gb/s). Les paramètres d'échantillonnage temporel sont fixés à $T_R = 208.7$ ns et $\Delta t_p = 100$ ps. Le système fonctionne avec une quantité de dispersion de $\ddot{\phi} = -1328$ ps/nm.

Table 2 Spécifications des SUT conçus.

SUT	Channels Wavelength [nm]	Bit Rate [Gb/s]	Modulation Type	PRBS Length
SUT_1	$\lambda_1 = 1565$	1	MZM	$2^{13}-1$
	$\lambda_2 = 1556.1$	25	DML	$2^{31}-1$
	$\lambda_3 = 1541.33$	1	MZM	$2^{13}-1$
	$\lambda_4 = 1540.94$	25	MZM	$2^{31}-1$
SUT_2	$\lambda_1 = 1556.1$	25	DML	$2^{31}-1$
	$\lambda_2 = 1541.73$	1	MZM	$2^{13}-1$
	$\lambda_3 = 1541.33$	1	MZM	$2^{13}-1$
	$\lambda_4 = 1540.94$	25	MZM	$2^{31}-1$
SUT_3	$\lambda_1 = 1550.52$	1	MZM	$2^{11}-1$
	$\lambda_2 = 1550.12$			
	$\lambda_3 = 1549.72$			
SUT_4	$\lambda_1 = 1556.1$	2.5	DML	$2^{31}-1$
	$\lambda_2 = 1542.2$	25	MZM	$2^{17}-1$
	$\lambda_3 = 1541.6$	25	MZM	$2^{17}-1$
	$\lambda_4 = 1540.94$	2.5	MZM	$2^{31}-1$
SUT_5	$\lambda_1 = 1550.52$	10	MZM	$2^{15}-1$
	$\lambda_2 = 1550.12$			
SUT_6	$\lambda_1 = 1550.92$	10	MZM	$2^{15}-1$
	$\lambda_2 = 1550.12$			

La Fig. 11 illustre la capacité du système RTOM à capter les changements d'intensité dans les différents canaux DWDM avec une précision dans la gamme des dBm. Dans ce cas, nous traitons SUT_2 composé de quatre flux de données situés aux longueurs d'onde centrales de $\lambda_1 = 1556.1\ \mathrm{nm}$, $\lambda_2 = 1541.73\ \mathrm{nm}$, $\lambda_3 = 1541.33\ \mathrm{nm}$, et $\lambda_4 = 1540.94\ \mathrm{nm}$. En termes de formats de modulation, Ch$_1$ utilise DML, tandis que les autres canaux utilisent MZM. Les flux de données pour Ch$_1$ et Ch$_4$ ont une longueur de $2^{31} - 1$ et fonctionnent à un débit de 25 Gb/s. À l'inverse, Ch$_2$ et Ch$_3$ sont configurés avec une longueur de flux de données de $2^{13} - 1$, fonctionnant à un débit de 1 Gb/s. Ces spécifications et leur arrangement au sein du SUT sont détaillés de manière concise dans le Tableau 2. Les paramètres d'échantillonnage temporel sont la période $T_\mathrm{R} = 208.7\ \mathrm{ns}$ et la largeur de temps $\Delta t_p = 100\ \mathrm{ps}$. La Fig. 11(a) montre la sortie mesurée pour SUT_2 comparée à sa forme d'onde spectrale de référence (mesure OSA). Pour une meilleure visualisation, seule une vue rapprochée de Ch_2-Ch_4 est affichée dans la Fig. 11(b-d). Par la suite, dans la Fig. 11(b), la puissance de Ch_3 est réduite de 2 dB, suivie d'une réduction de 6 dB dans la Fig. 11(c), et enfin éteinte dans la Fig. 11(d).

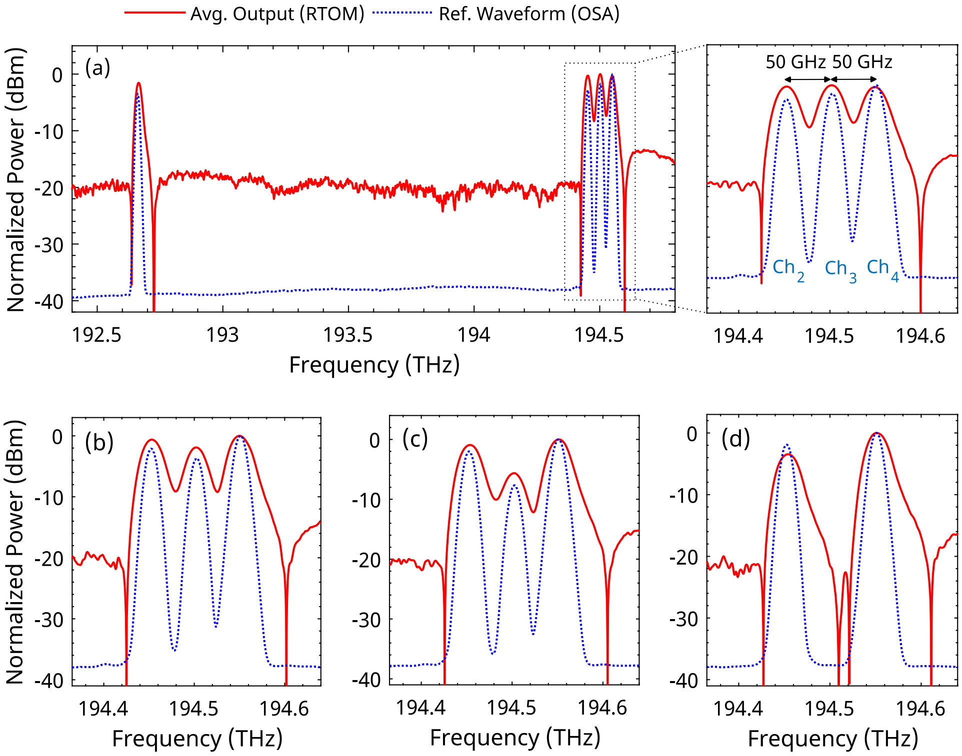

Fig. 11 Performance du système dans le cas du suivi des variations d'intensité dans Ch$_3$. (a) Aucun changement, (b) Atténuation de 2 dB, (c) Atténuation de 6 dB, (d) Extinction.

Comme prévu, les traces spectrales mesurées, obtenues en moyennant 239 échantillons consécutifs, suivent précisément la forme d'onde de référence mesurée avec l'OSA. Le résultat obtenu indique clairement que le système est capable de suivre les canaux de longueur d'onde avec la haute résolution requise, de manière à clairement résoudre la séparation des canaux DWDM de 50 GHz, comme indiqué par la flèche noire dans le zoom de la Fig. 11(a). La forte asymétrie dans les formes d'onde temporelles capturées par le RTOM pour chaque canal est principalement attribuée à la réponse temporelle irrégulière du système de détection limité en bande passante.

Pour atteindre une résolution de fréquence plus fine, comme approcher la précision de 0.1 nm offerte par l'OSA, une plus grande quantité de dispersion peut être utilisée. Pour démontrer cet effet, nous avons considéré SUT_3 composé de 3 canaux situés aux longueurs d'onde centrales de $\lambda_1 = 1550.52\ \mathrm{nm}$, $\lambda_2 = 1550.12\ \mathrm{nm}$, et $\lambda_3 = 1549.72\ \mathrm{nm}$ avec un espacement de canal de 50 GHz. Les flux de données dans SUT_3, fonctionnant à un débit binaire de 1 Gb/s, ont été codés en utilisant une longueur de PRBS de $2^{11} - 1$ et un type de modulation de MZM. Dans cette mesure, une SMF-28 de 20 km a été utilisée pour disperser le SUT_3. Deux modules compensateurs de dispersion ont été concaténés pour accumuler une dispersion totale de $\ddot{\phi} =$ -688.6 $\mathrm{ps/nm}$. La Fig. 12 illustre les traces spectrales pour différentes quantités de dispersion mesurées en utilisant le système RTOM, obtenues en moyennant 718 échantillons consécutifs comparés avec la forme d'onde de référence obtenue à partir d'une mesure spectrale en utilisant un OSA conventionnel avec une bande passante de résolution de 0.1 nm (~12.5 GHz). Il est observé qu'augmenter la quantité de dispersion améliore la résolution de fréquence, résultant en une forme d'onde de sortie qui suit la forme d'onde de référence avec plus de détails.

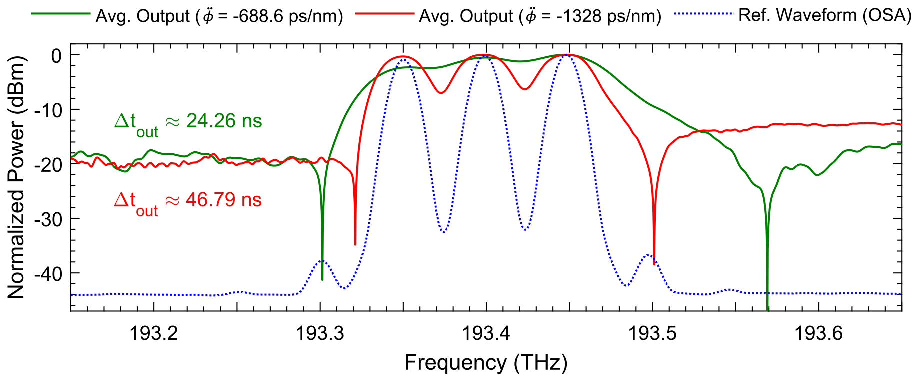

Fig. 12 Effet de la dispersion sur la résolution de fréquence du système RTOM. Les canaux DWDM ont un espacement de 50 GHz, fonctionnant à un débit binaire de 1 Gb/s avec une modulation MZM. L'échantillonnage temporel est réalisé en utilisant les paramètres suivants: $\Delta t_p = 100\ \mathrm{ps}$ et $T_R = 208.7\ \mathrm{ns}$.

Cependant, cette modification se traduirait nécessairement par une réduction du taux de mise à jour de mesure du RTOM. Cela découle du fait qu'une plus grande quantité de dispersion prolonge la durée du spectre mappé dans le temps Δt_{out}, nécessitant une période d'échantillonnage plus longue T_R. Étant donné que le taux de mise à jour de mesure du système RTOM est inversement lié à T_R, cet ajustement implique un taux de mise à jour plus lent. En considérant l'ensemble de la bande C, supportant 88 canaux avec un espacement de 50 GHz, des quantités de dispersion de $\ddot{\phi} = -688.6\ \mathrm{ps/nm}$ et $\ddot{\phi} = -1328\ \mathrm{ps/nm}$ résultent en des spectres mappés dans le temps de sortie avec des durées temporelles de $\Delta \mathrm{t_{out}} = 24.26\ \mathrm{ns}$ et $\Delta \mathrm{t_{out}} = 46.79\ \mathrm{ns}$, respectivement.

Comme observé sur la Fig. 12, sous une quantité de dispersion de $\ddot{\phi} = -688.6\ \mathrm{ps/nm}$, les canaux DWDM ne sont pas nettement séparés. Dans ce cas, en augmentant l'espacement des canaux de 50 GHz à 100 GHz, tout en maintenant la valeur de dispersion à $\ddot{\phi} = -688.6\ \mathrm{ps/nm}$, les canaux deviennent plus distincts. Cette caractéristique est démontrée dans la Fig. 9, montrant la trace spectrale RTOM dérivée de la moyenne de 239 échantillons consécutifs. Le $\mathrm{SUT_4}$ analysé ici est un signal à 4 canaux avec des longueurs d'onde centrales situées à $\lambda_1 = 1556.1\ \mathrm{nm}$, $\lambda_2 = 1542.4\ \mathrm{nm}$, $\lambda_3 = 1541.6\ \mathrm{nm}$, et $\lambda_4 = 1540.94\ \mathrm{nm}$. $\mathrm{Ch_1}$ et $\mathrm{Ch_4}$ fonctionnent à un débit binaire de 2.5 Gb/s, codés en utilisant une longueur de PRBS de $2^{31} - 1$, tandis que $\mathrm{Ch_2}$ et $\mathrm{Ch_3}$ fonctionnent à 25 Gb/s, codés en utilisant une longueur de PRBS de $2^{17} - 1$. Le $\mathrm{Ch_1}$ emploie le DML pour la modulation, et les canaux restants utilisent le MZM. La période d'échantillonnage du système RTOM est $T_R = 208.7\ \mathrm{ns}$. Pour une meilleure visualisation, une vue agrandie de $\mathrm{Ch_2}$ à $\mathrm{Ch_4}$ est également affichée ici. La comparaison de la Fig. 13 avec la Fig. 12 indique clairement comment l'augmentation de l'espacement des canaux améliore la distinction des canaux au même niveau de dispersion.

Enfin, nous démontrons la capacité unique du système RTOM dans le suivi en temps réel d'un signal de données d'entrée dynamique qui subit des changements rapides à l'échelle de la microseconde. À cet effet, le SUT d'entrée est en outre modulé avec une fonction de variation d'intensité de type carré judicieusement conçue, dans laquelle des changements sont introduits tous les 14 périodes d'analyse du système RTOM, chacune avec une durée de $T_R = 69.565\ \mathrm{ns}$. Ces changements impliquent l'ajustement des niveaux de puissance du SUT, y compris l'activation/désactivation de tous les canaux. Le $\mathrm{SUT_5}$ analysé dans la Fig. 14 est composé de deux canaux de données situés à $\lambda_1 = 1550.52\ \mathrm{nm}$ et $\lambda_2 = 1550.12\ \mathrm{nm}$, correspondant à un espacement de canal de 50 GHz. Les flux de données sont des signaux NRZ-OOK à un débit binaire de 10 Gb/s, codés en utilisant un PRBS de $2^{15} - 1$ et une modulation MZM. La Fig. 14(a) présente l'évolution mesurée du spectre. Le résultat obtenu à partir d'une mesure OSA conventionnelle est montré dans la Fig. 14(b), révélant la limitation de l'OSA en termes de vitesse pour le suivi des changements. La trace temporelle de sortie mesurée dans la Fig. 14(a) confirme la vitesse de mesure sans précédent du système RTOM permettant de suivre avec précision les changements spectraux dans le SUT à l'échelle de la microseconde. Le résultat est obtenu en moyennant tous les 14 périodes d'analyse consécutives, c'est-à-dire $69.565\ ns \times 14$. L'inverse de cette durée correspond au taux de mise à jour de mesure du système, qui est de 1 MHz. Un OSA typique nécessite environ 200 ms pour mesurer la bande C avec une bande passante de résolution de 0.1 nm, représentant une durée approximativement 10^4 fois plus longue que toutes les mesures consécutives effectuées dans la Fig. 14(a).

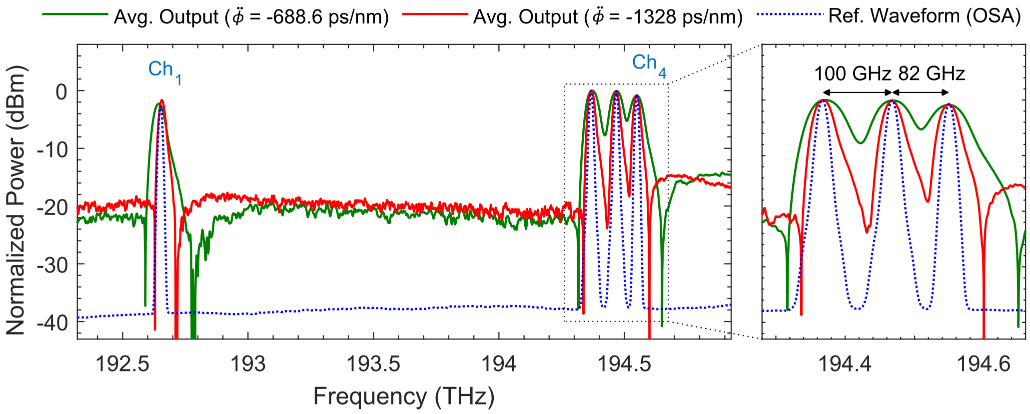

Fig. 13 Amélioration de la distinction des canaux DWDM avec l'augmentation de l'espacement des canaux à différents montants de dispersion. L'échantillonnage temporel est réalisé à $T_R = 208.7$ ns avec une largeur d'impulsion d'échantillonnage de $\Delta t_p = 100$ ps.

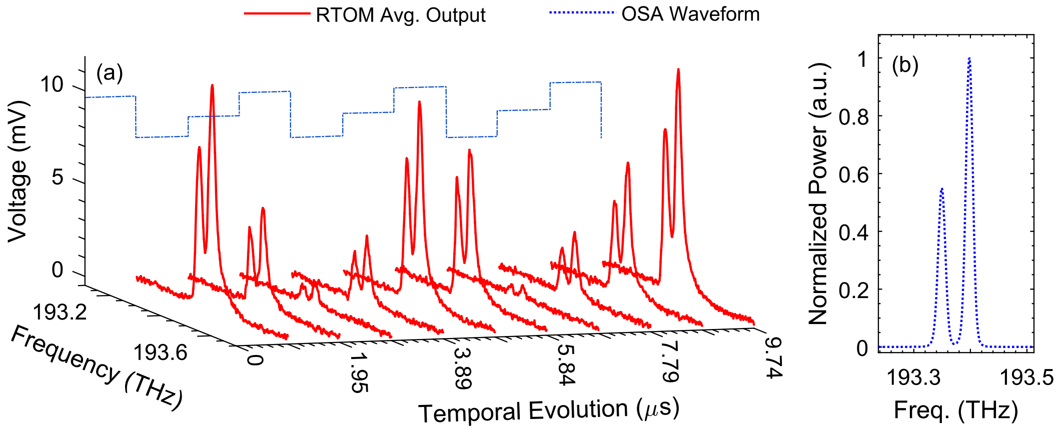

Fig. 14 (a) Forme d'onde de sortie RTOM obtenue pour le SUT_5 dynamique, changeant tous les 14 échantillons. (b) Forme d'onde obtenue à partir d'un OSA conventionnel pour tous les échantillons de SUT_5. L'espacement des canaux est de 50 GHz, et l'échantillonnage temporel est réalisé avec une période de $T_R = 69.565$ ns.

0.6. Conclusion

Dans cette thèse, nous nous sommes concentrés sur le suivi en temps réel du spectre optique évolutif des signaux DWDM au sein des liens de télécommunication et avons introduit un schéma nouveau et efficace à cet effet. Le système proposé, désigné sous le nom de RTOM, qui utilise l'échantillonnage temporel en conjonction avec le D-FTM, fournit une méthode simple pour discerner la présence et l'intensité relative de multiples canaux DWDM à travers toute la bande C de télécom optique (1530-1565 nm). Le système RTOM démontre une performance robuste dans une large gamme de conditions, incluant différents formats de modulation (MZM et DML), des débits binaires (allant de 1 Gb/s à 25 Gb/s), et des espacements de canaux DWDM (50 GHz et 100 GHz). De plus, il offre la résolution nécessaire pour discerner des canaux séparés par quelques dizaines de GHz, une précision, et des taux de mise à jour des mesures rapides et sans précédent dans la gamme des MHz, ce qui est des ordres de grandeur mieux que les OSAs. Cette polyvalence souligne l'applicabilité pratique du système dans une gamme d'environnements de réseau optique. Ainsi, les caractéristiques clés du système RTOM incluent: (1) un temps de réponse rapide; (2) la simplicité de mise en œuvre en utilisant des composants d'optique linéaire facilement disponibles, en particulier un modulateur Électro-Optique (EO) et un morceau de fibre; (3) une large gamme de surveillance; (4) une fine résolution; (5) l'adaptabilité à divers formats de modulation et débits binaires sans aucun besoin de modification; et (6) une intégration potentielle sur des puces photoniques. Bien que cette recherche démontre principalement des résultats pour les signaux non return to zero on-off keying (NRZ-OOK) dans la bande C, la méthodologie du système pourrait être applicable à d'autres larges bandes de fréquences (par exemple, les bandes O, S et L) et des signaux avec divers formats de codage.

Références

[1] "Proximion AB, white paper "Optical Layer Monitoring" (2013). Available: https://www.proximion.com/hubfs/bu-pr/white-paper/optical-layer-monitoring/100499-D-LDO-WISTOM-White-Paper-Optical-Layer-Monitoring-web.pdf."

[2] Z. Dong, F. N. Khan, Q. Sui, K. Zhong, C. Lu, and A. P. T. Lau, "Optical Performance Monitoring: A Review of Current and Future Technologies," *Journal of Lightwave Technology,* vol. 34, no. 2, pp. 525-543, 2016.

[3] A. E. Willner, Z. Pan, and C. Yu, "Optical performance monitoring," *Optical fiber telecommunications VB*, pp. 233-292: Elsevier, 2008.

[4] R. Salem, M. A. Foster, and A. L. Gaeta, "Application of space–time duality to ultrahigh-speed optical signal processing," *Advances in Optics and Photonics,* vol. 5, no. 3, 2013.

[5] J. Azana, and M. A. Muriel, "Real-time optical spectrum analysis based on the time-space duality in chirped fiber gratings," *IEEE Journal of Quantum Electronics,* vol. 36, no. 5, pp. 517-526, 2000.

[6] C. Wang, "Dispersive Fourier Transformation for Versatile Microwave Photonics Applications," *Photonics,* vol. 1, no. 4, pp. 586-612, 2014.

[7] L. Romero Cortés, D. Onori, H. Guillet de Chatellus, M. Burla, and J. Azaña, "Towards on-chip photonic-assisted radio-frequency spectral measurement and monitoring," *Optica,* vol. 7, no. 5, 2020.

[8] T. T. Wong, A. K. Lau, K. K. Wong, and K. K. Tsia, "Optical time-stretch confocal microscopy at 1 µm," *Optics letters,* vol. 37, no. 16, pp. 3330-3332, 2012.

[9] R. E. Saperstein, N. Alić, D. Panasenko, R. Rokitski, and Y. Fainman, "Time-domain waveform processing by chromatic dispersion for temporal shaping of optical pulses," *JOSA B,* vol. 22, no. 11, pp. 2427-2436, 2005.

[10] J. Hult, R. S. Watt, and C. F. Kaminski, "High bandwidth absorption spectroscopy with a dispersed supercontinuum source," *Optics express,* vol. 15, no. 18, pp. 11385-11395, 2007.

[11] B. Wetzel, A. Stefani, L. Larger, P.-A. Lacourt, J.-M. Merolla, T. Sylvestre, A. Kudlinski, A. Mussot, G. Genty, and F. Dias, "Real-time full bandwidth measurement of spectral noise in supercontinuum generation," *Scientific reports,* vol. 2, no. 1, pp. 882, 2012.

[12] J. Azaña, L. Chen, M. Muriel, and P. Smith, "Experimental demonstration of real-time Fourier transformation using linearly chirped fibre Bragg gratings," *Electronics Letters,* vol. 35, no. 25, pp. 2223-2224, 1999.

[13] W. Liu, W. Li, and J. Yao, "Real-time interrogation of a linearly chirped fiber Bragg grating sensor for simultaneous measurement of strain and temperature," *IEEE Photonics Technology Letters,* vol. 23, no. 18, pp. 1340-1342, 2011.

[14] S. Dobner, and C. Fallnich, "Dispersive Fourier transformation femtosecond stimulated Raman scattering," *Applied Physics B,* vol. 122, no. 11, 2016.

[15] M. H. Asghari, Y. Park, and J. Azaña, "Complex-field measurement of ultrafast dynamic optical waveforms based on real-time spectral interferometry," *Optics Express,* vol. 18, no. 16, pp. 16526-16538, 2010.

[16] Y. Liu, W. Ni, L. Yang, S. Huang, H. Liu, Y. Sun, R. Xia, Y. Yao, L. Yan, Y. Luo, Z. Xu, G. Xu, Q. Sun, X. Tang, and P. P. Shum, "Real-time spectral interferometry enables ultrafast acoustic detection," *Applied Physics Letters,* vol. 123, no. 21, 2023.

[17] A. Tae-Jung, P. Yongwoo, and J. Azaña, "Ultrarapid Optical Frequency-Domain Reflectometry Based Upon Dispersion-Induced Time Stretching: Principle and Applications," *IEEE Journal of Selected Topics in Quantum Electronics,* vol. 18, no. 1, pp. 148-165, 2012.

[18] C. Wang, and J. Yao, "Ultrahigh-Resolution Photonic-Assisted Microwave Frequency Identification Based on Temporal Channelization," *IEEE Transactions on Microwave Theory and Techniques,* vol. 61, no. 12, pp. 4275-4282, 2013.

[19] K. Goda, and B. Jalali, "Dispersive Fourier transformation for fast continuous single-shot measurements," *Nature Photonics,* vol. 7, no. 2, pp. 102-112, 2013.

[20] K. Krupa, K. Nithyanandan, U. Andral, P. Tchofo-Dinda, and P. Grelu, "Real-Time Observation of Internal Motion within Ultrafast Dissipative Optical Soliton Molecules," *Phys Rev Lett,* vol. 118, no. 24, pp. 243901, Jun 16, 2017.

[21] Dispersion Compensation Units.

Available: https://www.bccshop.fi/downloads/products/d/dc-ph-19/DC-PH.pdf.

[22] FRM5W232FY-InGaAs-APD/Preamp Receiver.

Available: https://datasheetspdf.com/pdf-file/657864/EudynaDevices/FRM5W232FY/1.

CONTENTS

LIST OF FIGURES

LIST OF TABLES

LIST OF ABBREVIATIONS

QoS	Quality of Service
SLA	Service-Level Agreement
WDM	Wavelength-Division Multiplexing
D-FTM	Dispersive Frequency-to-Time
RTOM	Real-Time Optical Monitoring
MZM	Mach-Zehnder Modulator
MEMS	Microelectromechanical System
RF	Radiofrequency
FWHM	Full-Width at Half Maximum
OPM	Optical Performance Monitoring
EDFA	Erbium-Doped Fiber Amplifier
DWDM	Dense-Wavelength-Division Multiplexing
QAM	Quadrature Amplitude Modulation
QPSK	Quadrature Phase-Shift Keying
PBC	Polarization Beam Controller
PBS	Polarization Beam Splitter
DCF	Dispersion-Compensating Fiber
LCFBG	Linearly Chirped Fiber Bragg Grating
CD	Chromatic Dispersion
PMD	Polarization-Mode Dispersion
SPM	Self-Phase Modulation
XPM	Cross-Phase Modulation
IFFT	Inverse Fast Fourier Transform
MPI	Multiple Path Interference
BER	Bit Error Rate
OSNR	Optical Signal-to-Noise Ratio
VSB	Vestigial Sideband
DSP	Digital Signal Processing
OSA	Optical Spectrum Analyzer
EO	Electro-Optic
LC	Liquid Crystal
LPF	Low-Pass Filter
SRS	Stimulated Raman Scattering
FWM	Four-Wave Mixing
FFT	Fast Fourier Transform
ML	Machine Learning
IoT	Internet of Things
GVD	Group-Velocity Dispersion
SMF	Single-Mode Fiber
TX	Transmitter
RX	Receiver
SUT	Signal Under Test
TOD	Third-Order Dispersion
PD	Photodetector
RTO	Real-Time Oscilloscope
ER	Extinction Ratio
PD-BW	Photodetector Bandwidth
MMI	Multi-Mode Interference

NRZ	Non-Return-to-Zero
OOK	On-Off-Keying
PASTA	Parametric Spectro-Temporal Analyzer
AWG	Arbitrary Waveform Generator
APD	Avalanche Photodiode
ROSA	Receiver Optical Subassembly
TIA	Transimpedance Amplifier
DML	Directly Modulated Laser
EML	Electro Absorption Modulated Laser
CW	Continuous Wave
SFP	Small Form Factor Pluggable
PC	Polarization Controller
PF	Polarization Filter
SiP	Silicon Photonics
WBG	Waveguide Bragg Grating
PRBS	Pseudo-Random Bit Sequence
O/E	Optical-to-Electrical
LCWBG	Linearly Chirped Waveguide Bragg Grating

1 INTRODUCTION

This chapter introduces the concept of performance monitoring in fiber optic networks, highlighting its essential role in today's high-capacity communication systems. It begins with an overview of optical performance monitoring (OPM), examining various techniques for monitoring the optical spectrum, their capabilities, and limitations. Following this, the chapter outlines the objectives of this thesis.

1.1 Background review

Fiber-optic communication has experienced tremendous growth over the past decade, primarily driven by an escalating demand for higher capacity. This growth is fueled by an exponential increase in the Internet traffic, both in terms of user numbers and bandwidth consumption. The trend of ever-increasing data traffic is set to continue, profoundly influencing the future of telecommunications. To meet these enormous bandwidth requirements, fiber-optic communication networks have evolved significantly. A key milestone in this evolution is the advent of wavelength-division-multiplexing (WDM) technique in combination with erbium-doped fiber amplifiers (EDFAs) [1]. WDM enables the simultaneous transmission of multiple data streams through a single optical fiber, with each stream occupying a distinct wavelength, significantly expanding the network's total data capacity, as shown in Fig. 1.1 [2]. For instance, using WDM, it is possible to accommodate ~40 channels in the C-band using a channel spacing of 100 GHz (0.8 nm). By employing dense-WDM (DWDM) technique, which utilizes a narrower channel spacing down to 12.5 GHz, the transmission of even more channels becomes feasible.

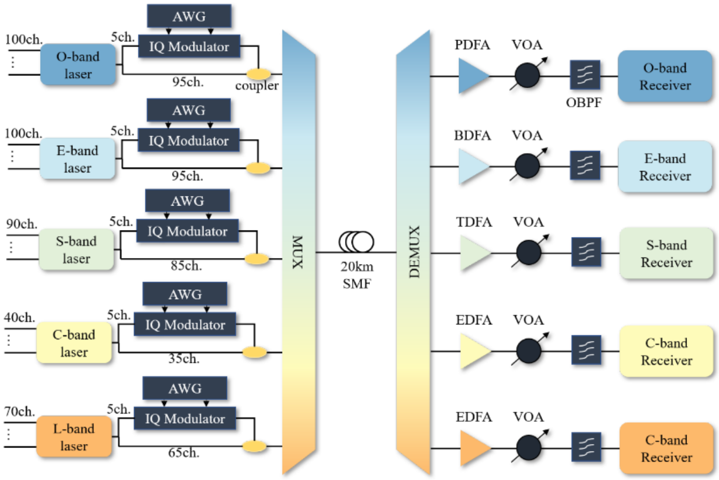

Fig. 1.1 Schematic of WDM transmission system [2].

Fig. 1.2 illustrates the current trend in telecommunications to enhance the bandwidth of a single optical fiber through narrowing the spacing between channels and elevating the data transmission rates [3]. Alongside conventional DWDM, the integration of advanced modulation formats such as quadrature amplitude modulation (QAM) and quadrature phase-shift keying (QPSK), which improves the channel utilization and capacity, has played a vital role in enhancing spectral efficiencies [4]. Additionally, the adoption of polarization multiplexing technology, as depicted in Fig. 1.3, and the development of elastic optical networks highlighted in Fig. 1.4, have marked significant strides in managing network resources more efficiently, especially in response to fluctuating traffic patterns [5]. These advancements have enabled modern networks to support remarkably high data rates.

However, these advancements also introduce new challenges in network management. The increase in data rates and the corresponding rise in network complexity have heightened the potential for service disruptions [6]. In systems where data is transmitted at extremely high rates, even a brief interruption can result in significant data loss, making network reliability a paramount concern. Moreover, the growing complexity of networks elevates the likelihood of parameter deviations that could potentially disrupt the entire network operation. This complexity not only reduces the mean-time-to-failure but also prolongs the mean-time-to-repair in case of network issues. In this context, the commitment of service providers to deliver consistent, high-quality services underscores the necessity for sophisticated monitoring mechanisms and rapid fault localization [6].

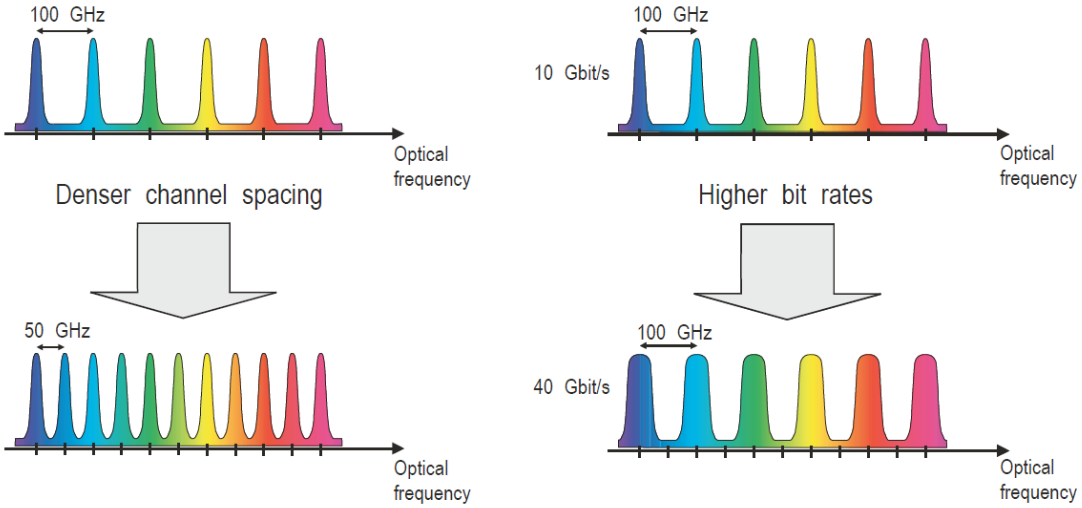

Fig. 1.2 The trend in telecommunication to meet the bandwidth requirement [3].

Future fiber optics networks are expected to be energy-efficient, robust, reconfigurable, flexible, reliable, and secure [6, 7]. Achieving these characteristics necessitates real-time, accurate, and consistent measurement and monitoring of network performance parameters, paths, and data streams [6]. In this regard, optical performance monitoring (OPM) devices play an indispensable role. Current fiber-optic networks lack the capability to gather real-time information about the network's physical state and the quality of the optical signals passing through different fiber links [8]. This deficiency compels network designers to maintain considerable safety margins to ensure reliability. However, this approach leads to underutilization of valuable network resources, a notable inefficiency in modern communication infrastructures. As networks evolve to become increasingly dynamic, the demand for advanced monitoring and management technologies grows more critical. Thus, the advancement of OPM technologies, as an integral part of optical networks, is a key focus area, offering the potential to evolve and enhance next generation optical networks.

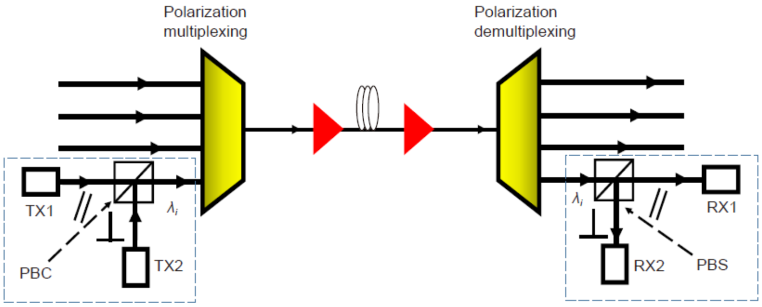

Fig. 1.3 Schematic representation of polarization multiplexing technology. PBC: polarization beam controller, PBS: polarization beam splitter, TX: transmitter, and RX: receiver [9].

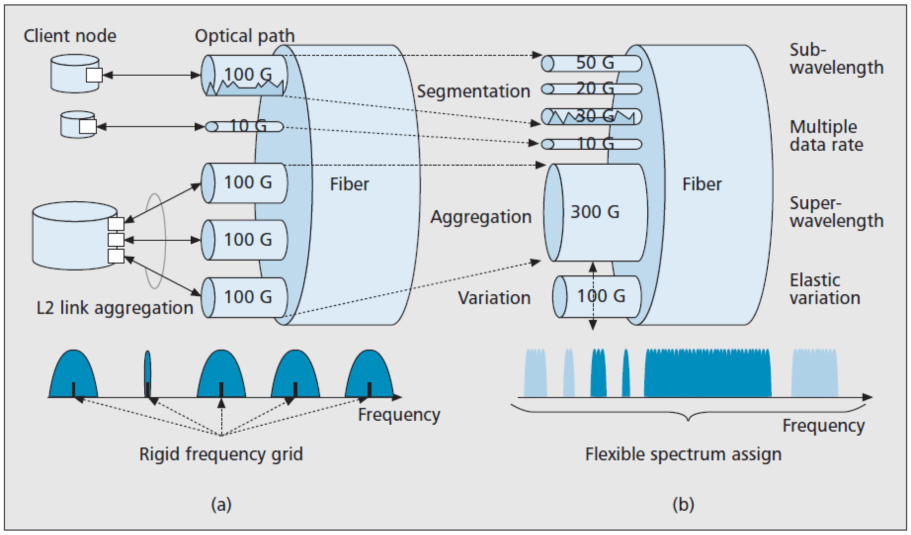

Fig. 1.4 Spectral allocation in (a) a conventional optical network, (b) an elastic optical network [10].

1.2 Optical performance monitoring (OPM)

Optical communication systems are currently undergoing a phase of rapid capacity expansion, evolving into increasingly complex, transparent, and dynamic networks [6, 11]. The total system capacity is determined by the maximum bit rate achievable for information transmission. These systems incorporate multiple modulation formats and different data rates to meet diverse users' demands. In this advanced paradigm, fiber-optic networks are susceptible to a range of transmission impairments such as chromatic dispersion (CD) and polarization-mode dispersion (PMD) that may significantly impact network performance [12, 13]. Fig. 1.5 shows a summary of optical network impairments [5]. These impairments can lead to a loss of optical power and encompass a variety of issues, such as fiber breaks, failures of network components, and errors in network equipment installation. Moreover, some impairments, while not necessarily diminishing the optical signal power, can severely distort the signal. Factors such as environmental changes, component drift, and rapid reconfigurations of network paths contribute to the variability of these impairments over time, underlining the dynamic nature of modern networks [13]. In addition, fiber impairments are subject to complex interactions between linear and nonlinear fiber effects, influenced by factors such as signal power, data rate, and data modulation format. Such complexities necessitate sophisticated monitoring and management strategies to ensure the optimal performance of these high-capacity optical networks.

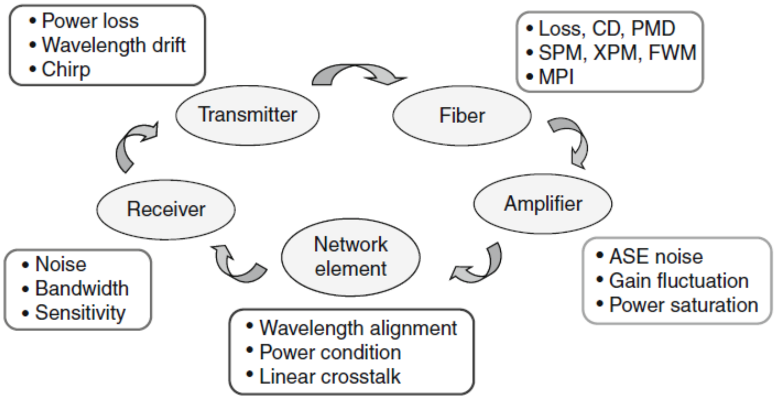

Fig. 1.5 Overview of optical network impairments. CD: chromatic dispersion, PMD: polarization-mode dispersion, SPM: self-phase modulation, XPM: cross-phase modulation, FWM: four-wave mixing, and MPI: multiple path interference [5].

Given the enormous amount of data traffic each fiber carries, even brief service disruptions can result in catastrophic consequences. For robust and stable operation of high-capacity networks, it is advisable to deploy monitoring systems that can detect accumulated impairment from each specific degrading effect. Early detection of signal degradation facilitates proactive measures, such as adjusting laser wavelengths or tuning compensators to prevent more severe network issues [6, 13]. OPM emerges as a pivotal technology for the control, management, and maintenance of both current and future high-speed, reconfigurable optical networks [5]. Functions necessitating OPM include, but are not limited to, amplifier control, channel identification, and signal health assessment [9]. Fig. 1.6 illustrates a future self-managed optical network featuring integrated OPM [4].

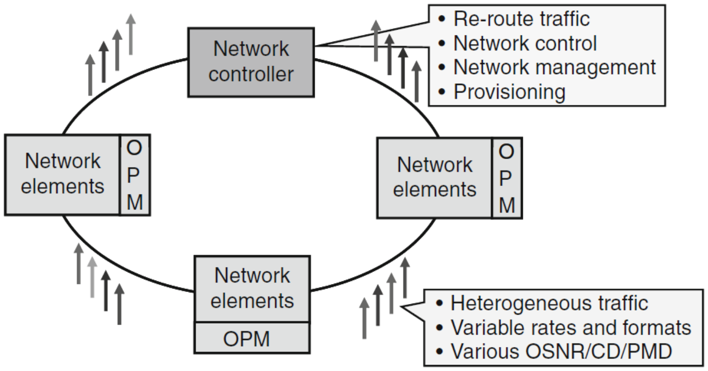

Fig. 1.6 A self-managed optical network equipped with OPM [6].

Performance monitoring has been a fundamental aspect of fiber-optic transmission systems since their inception, for example quality-of-service (QoS) measurements, being conducted in electrical domain following the optical-to-electronic (O/E) conversion of the monitored signal [8]. However, the efficient operation of dynamic DWDM networks necessitates the monitoring of key performance parameters directly within the optical domain [3]. This monitoring mechanism must be capable of continuously providing precise, real-time information about the health of network and integrity of each individual DWDM channel's data signal. The incorporation of such a monitoring mechanism throughout the optical network can enable a range of crucial and advanced network functionalities. These include adaptive impairments compensation, reliable network operation, efficient resources allocation, and Impairment-Aware routing [5, 8].

As mentioned earlier, transmission impairments vary over time due to the continuous reconfiguration of network paths. The nature of dynamic networks introduces variability in these impairments. Consequently, compensation techniques in such networks must be inherently adaptive, capable of responding to these fluctuating conditions. The key to implementing effective adaptive compensation lies in obtaining accurate information about the extent of impairments caused by each network link. OPM serves as an essential tool in this regard through assessing the degradation caused by the optical link. The insights gained from OPM about the network's performance can be leveraged to generate feedback signals for the adaptive compensation of these impairments. As OPM is providing continuous, real-time insights into the physical condition of an optical network, it can pinpoint the location and underlying causes of the faults. Additionally, it gathers detailed information regarding the extent and distribution of individual impairments within the network. This level of detail enables network operators to proactively identify when data signals begin to degrade. Thus, network providers can implement preventive measures timely, addressing potential problems before they escalate into serious issues that could significantly impair system performance. Such proactive management, enabled by OPM, is key to maintaining reliable network operation [14].

OPM also plays a crucial role in the efficient utilization of network resources within dynamic optical networks. For instance, if OPM indicates that the link quality is exceptionally high, this information can be relayed to the transmitter. The transmitter can then reduce the signal power while still adhering to the desired bit error rate (BER) requirements. Such a reduction in transmitted optical power not only conserves energy but also enhances the signal's robustness against nonlinear distortions, which are often a concern in high-power transmissions. Conversely, in scenarios where the BER starts to exceed acceptable thresholds, OPM enables network operators to make informed decisions. For example, they can increase the transmitted power of each channel, thereby boosting the optical signal-to-noise ratio (OSNR) to bring performance back within specifications. Furthermore, OPM can inform decisions to elevate data rates through higher modulation formats when the OSNR is observed to be sufficiently high. This adaptability, guided by OPM, allows for a more dynamic and responsive management of network resources, leading to a more efficient and effective optical network operation [8].

In existing static optical networks, data-routing algorithms typically direct traffic along the shortest paths or those satisfying certain minimum QoS constraints, such as delay, packet loss, and data rate [15]. However, these algorithms are less effective in dynamic optical networks, where they fail to consider the variable physical state of the network. To enhance routing capabilities in such environments, it is essential to update routing tables by incorporating optical layer parameters. These parameters include fiber length, signal distortion, amplifier noise, and transients. In such scenario, by feeding the information obtained through OPM into the network control systems, different weights can be assigned to all potential paths, taking into account a variety of parameters. Subsequently, routing decisions can be made based on these weighted calculations [13, 16]. Fig. 1.7 depicts the integration of OPM in optical networks, enabling adaptive compensation for impairments, ensuring reliable network operation, and facilitating impairment-aware routing.

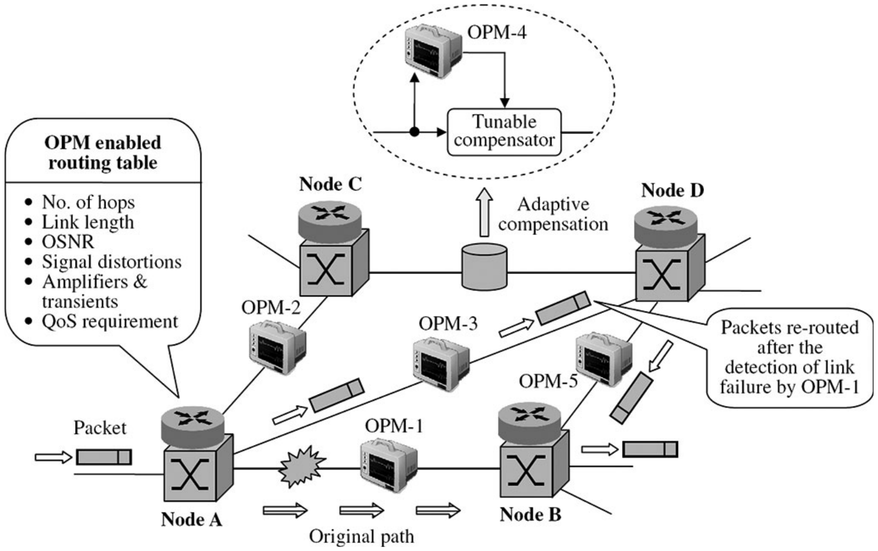

Fig. 1.7 Adaptive impairments compensation, ensuring reliable network operation, and facilitating impairment-aware routing via OPM integration in optical networks [8].

1.2.1 Desirable features of OPM techniques

The desirable characteristics of a given OPM technique depend on various factors, including the type of optical network where OPM module will be deployed, the nature and extent of impairments in the network, data rates, implementation costs, and the intended level of intelligence to be integrated into the OPM modules. Some common features that are typically expected from OPM techniques include [1,3]:

1. Fast response time:

In static optical networks, the response time of OPM techniques may be aligned with the network's restoration time, typically around 50 ms. However, in future dynamic optical communication systems that utilize high data rates and undergo frequent changes in network configurations and traffic patterns, the response time becomes increasingly crucial. OPM must have a response time significantly shorter than the network's reconfiguration interval to detect and address issues in real-time, thereby preventing or minimizing service disruptions. Most current OPM techniques generally require a duration ranging from about 100 ms to several tens of seconds to perform a complete measurement across the entire C-band, depending on the desired measurement resolution.

2. Accuracy, sensitivity, and dynamic range:

The effectiveness of compensation for impairments in dynamic optical networks is closely linked to the accuracy of the monitoring technique employed. These techniques must meet specific accuracy requirements and demonstrate high sensitivity across the entire monitoring range. They should also have a broad monitoring range to facilitate the appropriate compensation of network impairments that exhibit a wide dynamic range. The accuracy, sensitivity, and dynamic range of a monitoring technique can depend on several factors, such as the methodology used in the OPM module and the amount of signal power tapped from the optical link for monitoring purposes.

3. Multi-channel operation:

OPM techniques in WDM networks need to have the capability for simultaneous monitoring of multiple data channels. This can be achieved either through a parallel arrangement of monitoring devices or by employing a tunable optical filter for sequential monitoring of individual channels. The parallel approach, while offering simultaneous monitoring of all channels, requires a greater number of devices, leading to increased hardware costs. Conversely, the sequential method, although more hardware-efficient, can introduce measurement latency, particularly in systems with a large number of data channels. This trade-off between cost and performance efficiency is a critical consideration in the design and implementation of OPM techniques in WDM networks.

4. Operation at low input power:

For monitoring purposes, a portion of the signal power is tapped from the optical link. The OPM module needs to operate efficiently by utilizing only a minimal fraction of the signal power, while still fulfilling the accuracy and sensitivity requirements. Generally, the power used for monitoring should not exceed a small percentage of the total signal power.

5. Multi-impairment monitoring:

In an optical network where various impairments may coexist, employing separate techniques for monitoring each impairment can significantly increase costs. Therefore, it is essential for the monitoring techniques to have the capability to simultaneously and independently monitor multiple network impairments, ensuring cost-effectiveness and efficiency.

6. Data rate and modulation format transparency:

Future optical networks are anticipated to support various data rates and different modulation formats across individual channels. OPM techniques must adapt to these variations, eliminating the need for frequent modifications of monitoring modules to keep pace with evolving network characteristics.

7. Cost-effectiveness:

Given that OPM may be required at various network points, the cost should be comparatively lower than that of traditional monitoring equipment. This cost is often influenced by the complexity of the monitoring technique employed. Cost efficiency can be achieved by employing techniques capable of monitoring multiple impairments across several data channels and accommodating a range of data rates and modulation formats.

8. Passiveness:

OPM technique must operate without impacting the normal functioning of the optical network. This requires that the OPM technique neither alters network components during monitoring nor introduces extra signals into the network, as such signals could potentially interfere with the data signal, leading to a deterioration in data signal quality.

1.2.2 Overview of OPM techniques in fiber-optics networks

An illustrative example of a fiber-optic network equipped with OPM capabilities is presented in Fig. 1.8 [5]. OPM, in particular, involves a set of measurements conducted on optical signals at various points in the network to maintain network integrity and operational efficiency. In general, physical layer monitoring is closely tied to the design of the physical network. Fig. 1.9 illustrates the spectrum of monitoring applications required in modern optical networks, spanning from standard power monitoring to long-term degradation tracking [3]. Since different parameters may necessitate distinct monitoring devices, OPM is significantly constrained by the existing optical monitoring technologies.

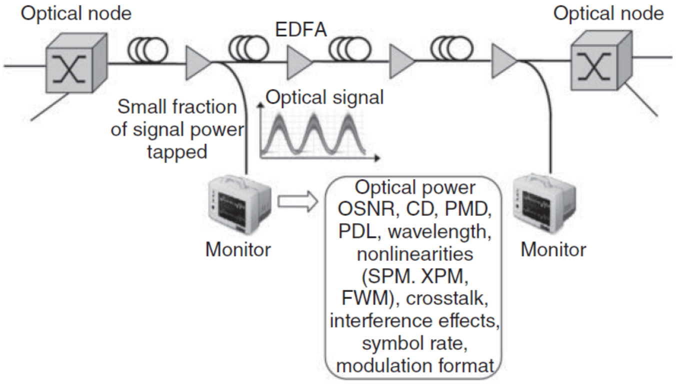

Fig. 1.8 A fiber-optic transmission network outfitted with OPM capabilities [5].

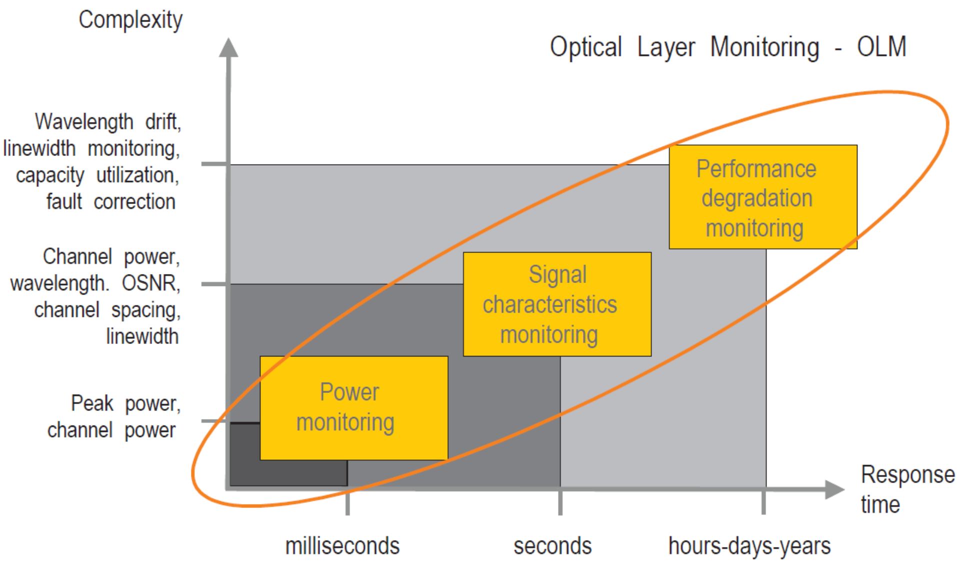

Fig. 1.9 Modern optical networks necessitate a variety of Optical Layer Monitoring applications, extending from standard power monitoring to long-term degradation monitoring [3].

Potential physical layer measurements that can be conducted on an optical signal might include [13]:

1. optical spectrum (i.e., channel wavelength and spectral shape)
2. amplitude power spectrum (RF spectrum)
3. average and peak power (per wavelength or aggregate)
4. pulse/bit shape
5. timing jitter
6. intensity/field autocorrelation (including higher order)
7. amplifier noise, gain and distortion
8. pump laser relative intensity noise transfer
9. amplitude histogram (synchronous and asynchronous)
10. Q-factor/eye diagram/bit error rate (i.e., V-curve measurements)
11. crosstalk and interference effects
12. chromatic dispersion (CD)
13. polarization state and polarization-dependent effects

14. polarization mode dispersion (PMD)
15. optical filter distortion
16. signal chirp and phase characteristics
17. optical signal-to-noise ratio (OSNR)
18. fiber nonlinearity-induced distortion and crosstalk

OPM encompasses a broad range of methodologies, and in recent years, a multitude of techniques for monitoring optical signal quality parameters in fiber-optic communication networks have been developed [5, 8, 13]. In general, these monitoring techniques can be broadly categorized into analog or digital methods. Digital OPM techniques employ high-speed electronic logic to process the digital information encoded within the optical waveform. Characteristics of the optical signal are inferred from measurements made on the digital signal. These digital methods exhibit a strong correlation with BER but typically fall short in effectively isolating the effects of individual impairments [5, 13]. Conversely, analog measurement techniques approach the optical signal as an analog waveform, focusing on measuring its specific characteristics. These measurements are usually protocol-independent and can be further categorized into time-domain, frequency-domain, and polarization-domain methods, based on whether the monitoring information is derived from the signal waveform, signal spectrum, or signal polarization, respectively [8].

Time-domain monitoring techniques are categorized into synchronous and asynchronous sampling-based methods, depending on whether the sampling rate is synchronized with the symbol rate [8]. Synchronous sampling techniques necessitate clock recovery, a process that becomes increasingly complex, particularly in networks supporting multiple data rates. Eye-diagram and Q-factor monitoring are examples of common synchronous sampling-based techniques that qualitatively illustrate the cumulative effects of all impairments on signal quality [13]. Fig. 1.10 illustrates an example of a Q-factor monitoring system [6]. The eye-diagram measurement lacks the capability to quantify the effects of individual impairments, and Q-factor monitoring is widely utilized in practice because of its strong correlation with BER. Asynchronous sampling-based techniques, such as amplitude histograms and single-channel sampling, are considered appealing because they eliminate the need for clock information. Additionally, they are capable of monitoring multiple impairments simultaneously, making them a cost-effective solution [5].

Frequency-domain methods are divided into measurements of the optical spectrum and the amplitude power spectrum (RF spectrum) [13]. Optical spectrum analysis techniques often employ an optical filter, which is tuned across the channel bandwidth, allowing for the recording of optical power. These techniques can be used to monitor multiple WDM channels, out-of-band OSNR, total optical power, and wavelength drift, but they lack the capability to monitor CD and PMD. Fig. 1.11 depicts a transparent WDM network equipped with OSNR monitor [17].

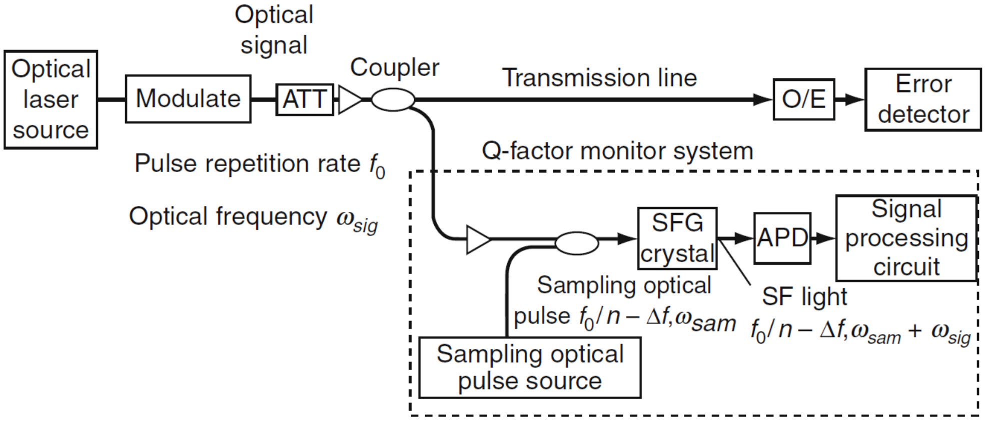

Fig. 1.10 An example of a Q-factor monitoring technique [6].

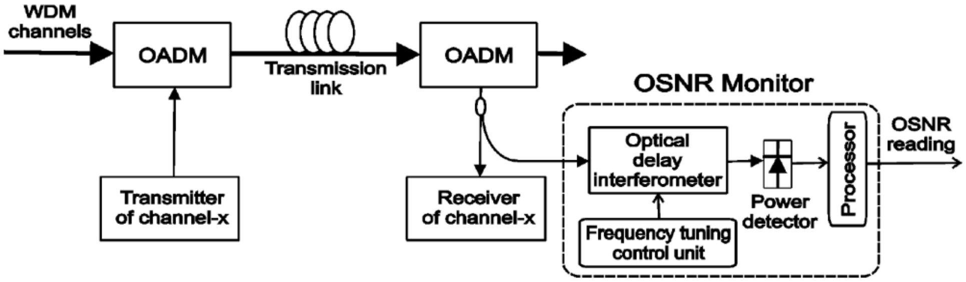

Fig. 1.11 Schematic of an OSNR monitor used in a transparent WDM network [17].

Given that the optical filter requires tuning to scan the entire WDM spectrum, a process that may take some time, such techniques can introduce measurement latency. RF spectrum techniques offer a more accurate estimation of signal quality compared to optical spectrum-based methods, as they analyze the spectrum of the signal encoded on the optical carrier [5]. These techniques can utilize inherent clock tones present in the spectrum of various modulation formats, or they can insert pilot tones of different frequencies in each channel at the transmitter. Clock tones-based monitoring techniques are capable of measuring CD and PMD and are data rate and modulation format dependent. Conversely, pilot tones-based schemes have the ability to measure a variety of parameters, including wavelength, OSNR, CD, and PMD, and are independent of both data rate and modulation format [8]. Fig. 1.12 shows CD monitoring using vestigial sideband (VSB) filtering [13].

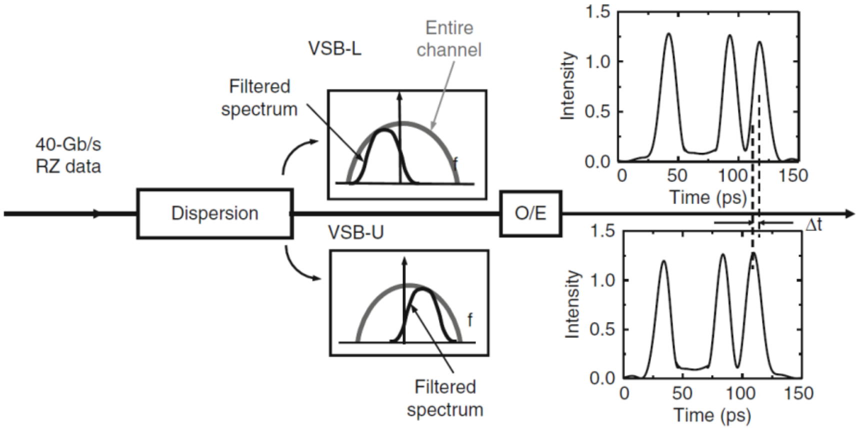

Fig. 1.12 CD monitoring using optical VSB filtering [13].

Polarization-domain monitoring techniques leverage the polarization properties of the optical signal. Changes in polarization characteristics, resulting from various channel degradations, can be effectively used to monitor these impairments. These techniques are capable of monitoring signal and noise powers, and consequently, OSNR, which can be achieved through polarization nulling. Additionally, they can assess PMD by measuring degree-of-polarization (DOP) of the received signal. These techniques offer the advantage of being transparent to data rates and modulation formats. However, their applicability is limited in the context of polarization-multiplexed signals, which significantly restricts their use in coherent transmission systems [5, 8].

In this research work, the focus is on optical spectrum monitoring, which involves measuring DWDM channel power, presence, and wavelength, as shown in Fig. 1.13. Optical power at a specific wavelength is a fundamental parameter in any fiber network. This power can significantly decrease due to factors like fiber attenuation and losses at various points such as fiber connectors, splices, couplers, or in cases of fiber breaks [8]. Monitoring other parameters or impairments depends on the measurement of optical power. In WDM systems, information regarding the power of each channel is required to dynamically equalize the power through a feedback mechanism, thereby ensuring stable system performance [18]. Similarly, wavelength measurement provides critical information about the precise positioning of the optical signal within its designated channel. By providing real-time data on these essential parameters, OPM enables network operators to maintain optimal performance, minimize downtime, reduce network operation and maintenance costs, and effectively manage the complexities inherent in modern fiber-optic networks.

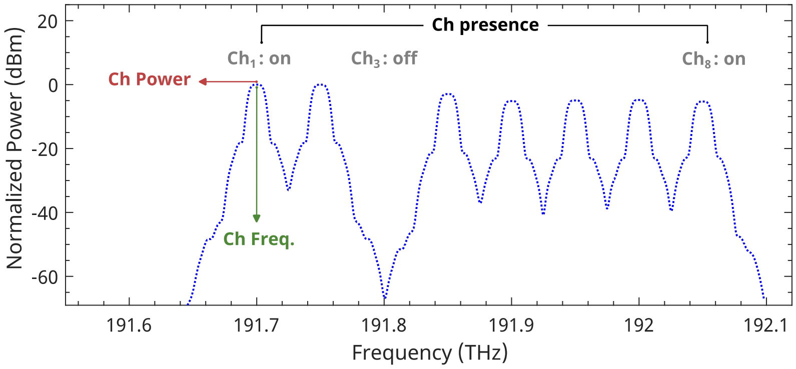

Fig. 1.13 OSA trace of the data being transmitted used as a reference waveform to obtain signal information such as DWDM channels power, presence, and wavelength.

1.3 Optical spectrum monitoring techniques and their limitations

The development of critical signal analysis and processing technologies is becoming increasingly essential to support next-generation ultrahigh-speed optical communication systems, particularly optical access networks [19]. These networks provide a fiber connection between service providers and end users, exploiting WDM strategies to meet the ever-increasing demand for higher capacity at the cost of imposing complexity to the system. Typically, a WDM channel occupies a bandwidth of 50-100 GHz, with channels aggregating to cover the entire transmission bandwidth, e.g., ~ 4 THz along the optical fiber communication C-band (i.e., 1530-1565 nm). By dividing the overall transmission bandwidth into narrower signal channels, the WDM approach enables the implementation of the signal analysis and processing at the individual channel level using versatile electronic-based digital signal processing (DSP) [20, 21]. However, the individual channel bandwidth in a WDM scheme is still sufficiently broad, posing a significant challenge for the real-time implementation of many key signal analysis and processing tasks.

Monitoring the health and performance of fiber-optic networks at the physical layer level is typically carried out by tracking the frequency spectrum of the data signals across different WDM channels. The main goal is to identify the WDM channels present at any given time across the frequency band of interest and their relative intensity, as illustrated in Fig. 1.13. Accordingly, future communication systems require an increased level of agility and versatility to adapt quickly and efficiently to the changing network conditions [22, 23]. To address this crucial requirement, developing cost- and energy-efficient signal analysis and processing tools with real-time capabilities and extremely low latencies is of paramount importance. Several optical spectrum monitoring schemes, mainly based on conventional optical spectrum analysis principles, have been proposed and developed over the years [3, 24-37]. The photodiode array optical spectrum analyzer (OSA) [24] using a diffraction grating as depicted in Fig. 1.14, and Fabry–Pérot interferometer OSA [25] consisting of a silicon mirror cavity were proposed for WDM performance monitoring. However, these methods are constrained by the need for mechanically moving parts in the grating, complicated fabrication processes of cavities, and the requirement of expensive devices or complex data processing. An arrayed waveguide grating-based OSA was proposed to attain high-precision measurements without moving parts [26]. The development of microelectromechanical system (MEMS)-based OSA [27, 28], Liquid crystal (LC)-based Fourier OSA (LC FOSA) [29], and OSA using tilted fiber grating [30, 31] showed some progress toward improving the measurement speed and achieving a cost effective method.

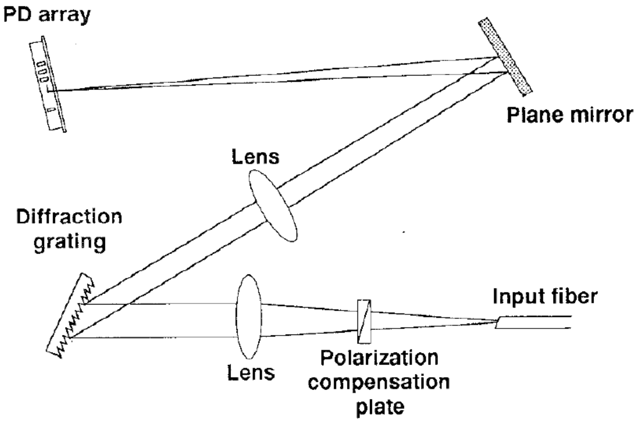

Fig. 1.14 Optical configuration of photodiode array OSA [24].

A high performance scanning filter, known as WISTOM, without using any moving parts and based on an acoustic-optic actuator as well as a chirped fiber Bragg grating was then proposed for WDM optical networks with the capability of handling both optical performance and channel monitoring along with less than 100 μs scanning time [3], as illustrated in Fig. 1.15. Nonetheless, these methods still face limitations, preventing them from keeping pace with the rapid development of high-speed optical communication systems. In particular, these WDM signal monitoring methods [24-31] suffer from slow update rates (typically in the kHz range and lower), which makes real-time measurements impossible. Specifically, available methods cannot be easily adapted to track spectral changes that may occur in a microsecond scale or faster. In OSA based monitoring techniques, the time required for scanning and completing a measurement across the entire C-band is about 100 ms to several tens of seconds, depending on the measurement resolution [11]. In addition, these methods are generally costly and are often based on bulky as well as inefficient designs, e.g., free-space optics, which may not be easily optimized for integration, potentially posing challenges for in-line monitoring tasks along the optical fiber links.

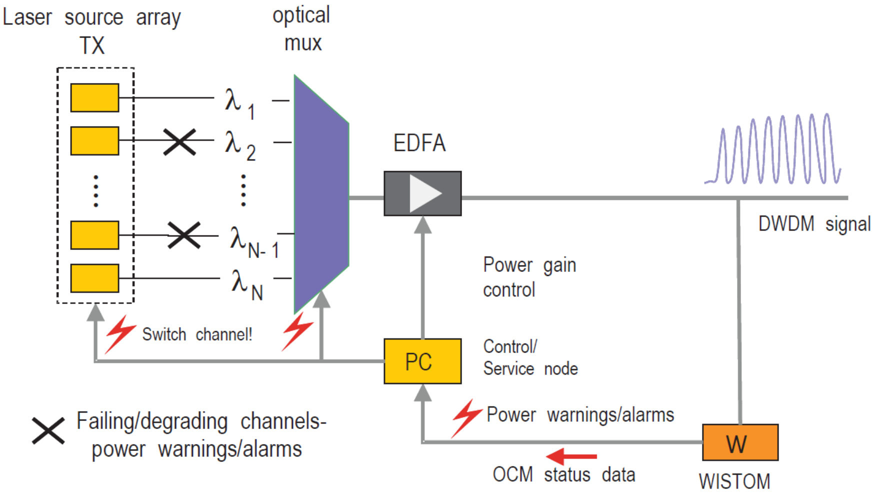

Fig. 1.15 Application of WISTOM as a power monitor [3].

Current mainstream monitoring schemes in optical networks predominantly use direct or coherent detection methods for high-speed signals [6]. These schemes employ DSP algorithms to monitor the performance of WDM channels. Direct detection schemes without optical filters at the receiver end analyze a small portion (less than 5%) of the optical signal using DSP algorithms, providing a low-cost assessment of channel performance [6]. However, a notable drawback of these monitoring schemes is that they inherently lose a significant channel characteristics information, resulting in a substantial reduction in the accuracy. In contrast, coherent detection methods, using a tunable filter or a diffraction grating spectrometer, acquire spectral information in the channel or within a specific wavelength range. In addition, these methods offer high recognition resolution and a broad monitoring range for analyzing spectral information, optical power, modulation format, OSNR, and other key monitoring parameters. However, their requirement of using expensive tunable lasers, complex structural requirements, and limitations associated with monitoring channels on a one-by-one basis make them less viable for widespread application in WDM networks [6].

To solve these problems, advancements have led to the development and exploration of monitoring techniques such as parametric spectro-temporal analyzer (PASTA) [32], optical labels

[34], and pilot tone based OPM [35]. The PASTA system employs a time-lens focusing mechanism and offers a measurement frame rate of 100 MHz, as illustrated in Fig. 1.16. However, its application is somewhat limited due to a narrow spectral observation range, typically around 5 to 10 nm [32]. Optical label monitoring technologies provide detailed channel information, significantly enhancing the capability to assess the working state and optimize resource utilization within WDM networks [34], as shown in Fig. 1.17. Despite their advantages, these technologies encounter challenges such as stimulated Raman scattering (SRS) and CD effect. Mitigating these effects, often requires dividing the entire wavelength channels into several sub-channels, a process that usually necessitates the use of expensive optical filters, thereby increasing both complexity and cost. Furthermore, the use of high-frequency pilot tones introduces a different challenge. In long-distance fiber transmissions, large CD can result in significant power fading of these pilot tones, which severely hampers the monitoring performance. In addition, pilot tones may interfere with the data signal, necessitating modification at the transmitter end, an approach that can be both complex and costly [36]. The optical labeling scheme that employs subcarrier index modulation (SIM) demonstrates efficient demodulation of labeling signals. However, this technique requires the implementation of large-scale Inverse Fast Fourier Transform (IFFT) and Fast Fourier Transform (FFT), contributing to considerable circuit complexity. Additionally, monitoring channel optical power becomes challenging due to the SRS effect, which restricts the flexibility in adjusting the transmission rate of label signals, thereby adding to operational limitations [37]. Monitoring techniques have also adopted machine learning (ML) algorithms for enhanced performance. While these methods are innovative, they necessitate extensive pre-processing and dataset training, thereby increasing their implementation complexity compared to conventional DSP methods [33, 38].

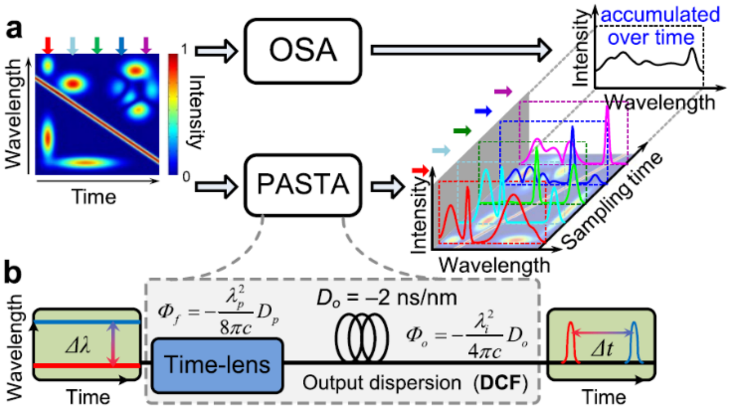

Fig. 1.16 The PASTA system obtaining the spectral evolution through a time-lens focusing mechanism [32].

In light of these considerations, OPM technologies for WDM networks, characterized by their large scale, complex structures, and continuous expansion, still faces significant challenges. The primary task lies in designing spectrum monitors that are not only fast and compact but also cost effective and easy to deploy across the network. Moreover, these monitors need to be capable of covering the entire communication band, such as the C-band, and potentially even broader ranges. Successfully achieving this combination of speed, affordability, comprehensive coverage, and ease of deployment is a critical task for ensuring effective performance monitoring in complex WDM networks.

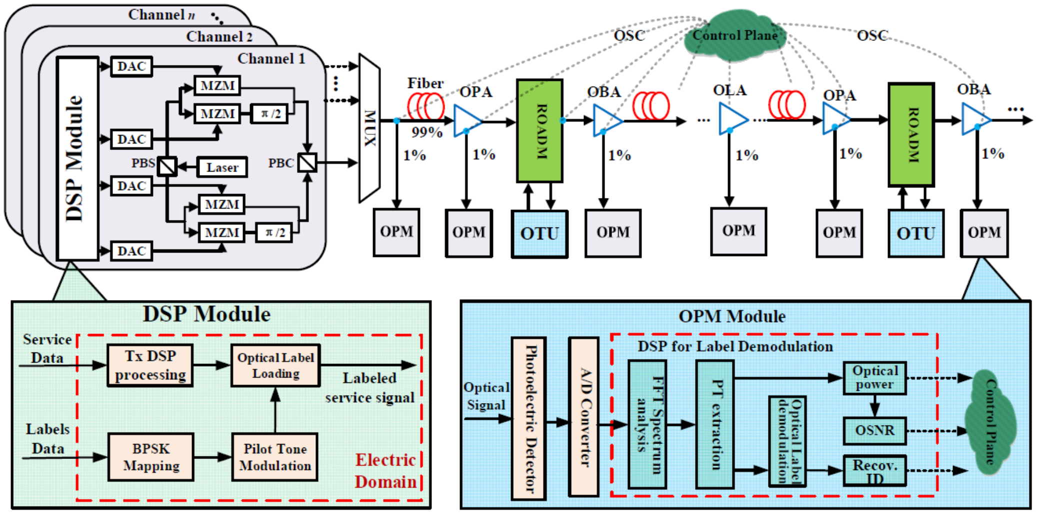

Fig. 1.17 Diagrammatic representation of the optical label enabled OPM scheme [34].

1.4 Presentation of thesis objectives and organization

With the advent of cloud services, 4K video streaming, 5G technology, and the Internet of Things (IoT), there is an undeniable trend towards diversification in both the speed and types of future telecom services. Given these developments, optical fiber communication networks face the challenge of accommodating future growth in various aspects, such as modulation formats, DWDM channel size, number of optical carriers, and other optical parameters [39]. An essential capability for these networks is the detection of impairments and the identification of threats, whether intentional or accidental. Currently, there is a deficiency in the measurement science and metrology of networks, leading to overbuilding and inefficient resource utilization [6]. In DWDM networks, monitoring key parameters directly in the optical layer is of great importance. This is where optical spectrum monitoring comes into play. The desired features of an optical monitoring system depend on the system's intelligence, complexity, and bit rates. Achieving a right balance among monitoring coverage, sensitivity, and cost is essential. An ideal optical spectrum monitoring system should provide advantages such as fast response time and minimal latency, simplicity in implementation, cost-effectiveness, applicability to various formats without monitor modification, fine resolution, wide monitoring range, and integration potential onto photonic chips [6].

The objective of this Master’s thesis is to take advantage of dispersive Fourier transformation to propose and develop a novel and simple real-time optical spectrum monitoring system compatible with the dynamic spectral analysis of telecommunication data signals. In particular, we explore here the use of dispersive Fourier transformation [40-43]—or dispersive frequency-to-time mapping (D-FTM)—for real-time WDM signal monitoring for the first time to our knowledge. In the D-FTM technique, the spectrum of a signal is directly mapped into time using linear group-velocity dispersion (GVD), provided that a temporal far-field condition is met [44]. Despite the broad application of D-FTM [45-52], its potential in monitoring telecom data signals has remained unexplored. This is because D-FTM is limited to processing time-restricted waveforms (e.g., femtosecond/picosecond pulses), rendering it incompatible with continuous signals, such as telecom data streams. Here, we introduce a novel approach to adapt D-FTM for continuous data signals, involving a suitably designed temporal sampling of the telecommunication data signal under test. We aim to theoretically study and experimentally demonstrate this proposed system. The operation of the proposed system is investigated over the entire C-band, e.g., comprising 88 channels with 50 GHz channel spacing. Employing the D-FTM technique allows us to have real-time measurements of the telecom signal spectrum. A central conclusion of our research is the demonstration of system design principles essential for capturing the necessary data to execute the intended optical monitoring tasks. Our approach surpasses previous methodologies by facilitating real-time monitoring of optical signal spectra with unprecedented measurement update rates extending into the MHz range.

This thesis consists of two main parts. The first part delves into the design considerations, discussing the design trade-offs and deriving key equations and conditions of the proposed monitoring system. It also determines the optimal design parameters through comprehensive numerical simulations. This part also includes a thorough evaluation of the system's performance based on these simulations, providing a theoretical understanding of its capabilities and limitations. The second part involves experimental validation to assess the system's performance and capabilities. This hands-on approach allows us to validate the theoretical findings from the first part and provides real-world insights into how the system operates under various conditions.

Specifically, chapter 1 reviews optical spectrum monitoring, its background, significance, and the development of various methods. The major contributions of this research work is then summarized. Chapter 2 delves into the foundational concept and operational principles of the proposed method, including an exploration of key design trade-offs. It begins with a concise review of the D-FTM concept, followed by an examination of its application areas and limitations with continuous signals. The chapter then provides a detailed description of our proposed scheme. Chapter 3 presents results from theoretical analyses and numerical simulations conducted to determine the optimal design parameters for real-time optical spectrum monitoring of DWDM signals. It also explores the system's performance with dynamic DWDM signals, discussing how various design parameters influence the system's dynamic range. Chapter 4 details experimental results for DWDM signals across various bit rates and modulation formats, accompanied by a comprehensive analysis of the key findings. Finally, chapter 5 concludes the thesis, reflecting on the implications of these findings and discussing potential avenues for future work.

2 BACKGROUND CONCEPTS AND OPERATING PRINCIPLES

This chapter provides a comprehensive overview of the fundamental concepts and operational principles underlying the proposed system. Initially, it delves into the concept of dispersive Fourier transformation, detailing its application and inherent constraints when applied to continuous signals. Subsequently, the design and functionality of the proposed system along with the technique employed to overcome dispersive Fourier transformation's limitation are introduced.

2.1 Dispersive Fourier transformation

The fundamentals of dispersive Fourier transform—or dispersive frequency-to-time mapping (D-FTM)—are based on the analogy between Fresnel diffraction and temporal dispersion, also known as space-time duality [53]. In free-space optics, the Fourier transform of a wave's transverse profile can be derived within the context of far-field propagation. The space-time duality enables a similar process in the time domain. Once a given signal propagates through a medium exhibiting a certain amount of second-order dispersion, also referred to as group-velocity dispersion (GVD), e.g. an optical fiber, the frequency spectrum of the signal launched at the input is directly mapped along the time domain [41, 43, 44]. This process is depicted in Fig. 2.1. Various kinds of dispersive media have been used for D-FTM implementation [44]. The simplest and commonly used dispersive element is single-mode fibers (SMFs), exhibiting a relatively modest GVD (~17 ps/nm/Km at 1550 nm) [54, 55]. Dispersion-compensating fibers (DCFs) can provide higher GVD values (e.g. 120 ps/nm/Km at 1550 nm) [56, 57], and linearly chirped fiber Bragg gratings (LC-FBGs) offer a compact attractive alternative with a large amount of GVD [44, 58, 59].

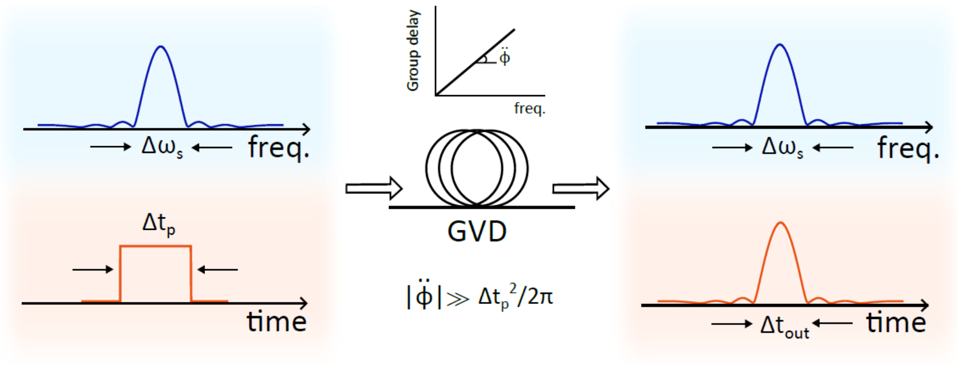

Fig. 2.1 Schematic illustrating the frequency-to-time conversion within a dispersive medium.

GVD: group-velocity dispersion ($\ddot{\phi}$), Δt_p: time-width duration of input signal under test (SUT), $\Delta\omega_s$: SUT full bandwidth, Δt_{out}: time-mapped spectrum duration.

A dispersive medium can be modeled as a linear time-invariant (LTI) system, with its transfer function defined as follows [41]:

$$H(\omega) = |H(\omega)|\exp(-j\phi(\omega)) \tag{2.1}$$

where $|H(\omega)|$ and $\phi(\omega)$ represent the magnitude and spectral phase response of the dispersive medium at angular frequency ω, respectively. In the vicinity of central frequency of interest ω_0, the phase response $\phi(\omega)$ can be expressed using a Taylor series expansion, given as:

$$\phi(\omega) = \phi_0 + \dot{\phi}_0(\omega - \omega_0) + \frac{1}{2}\ddot{\phi}_0(\omega - \omega_0)^2 + \frac{1}{6}\dddot{\phi}_0(\omega - \omega_0)^3 + \cdots \tag{2.2}$$

where $\phi_0 = \phi(\omega_0)$ is the phase constant at the carrier angular frequency, $\dot{\phi} = \frac{d\phi(\omega)}{d\omega}|_{\omega=\omega_0}$ is the group delay, $\ddot{\phi} = \frac{d^2\phi(\omega)}{d\omega^2}|_{\omega=\omega_0}$ denotes the GVD, and $\dddot{\phi} = \frac{d^3\phi(\omega)}{d\omega^3}|_{\omega=\omega_0}$ is defined as the third-order dispersion (TOD). Under the second-order dispersion approximation, where the phase terms above the second-order are neglected within the spectral bandwidth of interest, the transfer function $H(\omega)$ takes the form [41, 43] :

$$H(\omega') \cong |H(\omega)| \exp(-j\phi_0) \exp(-j\dot{\phi}_0\omega') \exp\left(-j\tfrac{1}{2}\ddot{\phi}_0\omega'^2\right) \tag{2.3}$$

where ω' is used to replace $\omega - \omega_0$ in Eq. (2-2). Assuming a constant magnitude response across the desired spectral bandwidth $\Delta\omega$, centered at the optical carrier frequency ω_0, we can focus on the phase response. The phase constant ϕ_0 and the group delay $\dot{\phi}$ do not affect the signal shape and can be ignored, allowing one to focus on the signal distortion induced by the GVD. The related impulse response, denoted as $h(t)$, can then be obtained by taking the inverse Fourier transform of this transfer function as [41, 43] :

$$h(t) = \tilde{F}^{-1}[H(\omega')] \propto \exp\left(j\tfrac{1}{2\ddot{\phi}_0}t^2\right) \tag{2.4}$$

Let $x(t)$ and $y(t)$ denote the complex envelopes of the input and output optical signals of the dispersive element, characterized by the impulse response $h(t)$, respectively. Assuming the dispersive element has a bandwidth that covers the full spectrum of the input optical signal, the relationship between the output and the input is established by the convolution operation, $y(t) = x(t) * h(t)$. Given the impulse response in Eq. (2.4), the output pulse can be redefined as:

$$y(t) = \int_{-\infty}^{+\infty} x(t')h(t - t')dt' \propto \int_{-\infty}^{+\infty} x(t') \exp\left(j\frac{1}{2\ddot{\phi}_0}(t - t')^2\right) dt'$$

$$\propto \exp\left(j\frac{t^2}{2\ddot{\phi}_0}\right)\int_{-\infty}^{+\infty} x(t')\exp\left(j\frac{1}{2\ddot{\phi}_0}t'^2\right)\exp\left(-j\frac{1}{\ddot{\phi}_0}tt'^2\right)dt' \qquad (2.5)$$

where t' is the integral variable. When the GVD is sufficiently strong such that:

$$\left|\ddot{\phi}\right| \gg \Delta t_p^2/2\pi \qquad (2.6)$$

where Δt_p is the total duration of the input signal, then the output signal can be approximated to:

$$y(t) \propto \exp\left(j\frac{t^2}{2\ddot{\phi}_0}\right)\int_{-\infty}^{+\infty} x(t')\exp\left(-j\frac{t}{\ddot{\phi}_0}t'\right)dt' \propto \exp\left(j\frac{t^2}{2\ddot{\phi}_0}\right)\left[X(\omega)\right]_{\omega=\frac{t}{\ddot{\phi}_0}} \qquad (2.7a)$$

$$X(\omega) = \tilde{F}[x(t)] \qquad (2.7b)$$

In a first approach, one can consider that group delay depends linearly on the frequency whose slope defines second-order GVD, $\ddot{\phi}$. The group delay characteristic of the medium causes different frequency components of the input signal travel at different speeds, allowing each spectral component to be mapped to a different time delay at the output of the dispersive medium [41]. Hence, under the condition of inequality (2.6), which is also known as temporal Fraunhofer– or temporal far-field–condition, the output signal becomes proportional to a scaled replica of the frequency spectrum (Fourier transform) of the input signal, except for a time-dependent quadratic phase factor [41]. Specifically, the signal's frequency spectrum is mapped along the temporal domain, with a frequency-to-time mapping relation given by [41]:

$$\omega = \frac{t}{\ddot{\phi}_0} \qquad (2.8)$$

While the D-FTM principle has been extensively used in a variety of science and engineering domains—such as real-time spectroscopy [48], interferometry [45, 52], reflectometry [49], high-speed microwave spectrum sensing [50], ultrafast metrology and imaging [46, 51], and many others [43]—its application to monitoring telecom data signals has not been explored thus far. The main challenge lies in the inherent constraint of D-FTM to analyze only time-limited duration (Δt_p) waveforms (e.g., femtosecond/picosecond pulse-like waveforms), imposed by the far-field condition requirement. Consequently, this method is unsuitable for the analysis of continuous signals, such as telecommunication data streams. However, in this work, we introduce a simple yet innovative approach to overcome this limitation, enabling the effective use of D-FTM for continuous signal analysis, the details of which will be elaborated in the subsequent section.

2.2 Proposed optical spectrum monitoring scheme

In this work, we propose a real-time optical monitoring (RTOM) system based on simple and practical linear fiber-optics components that leverage D-FTM for real-time monitoring of dense-wavelength-division-multiplexed (DWDM) signals. As discussed in section 2.1, D-FTM directly maps the spectrum of a given signal along the time domain employing linear GVD, provided that the temporal far-field condition is satisfied [44]. However, D-FTM functions with transform-limited optical pulses only (e.g., femtosecond/picosecond pulses), posing a limitation for continuous signal analysis. To overcome this intrinsic limitation, we propose incorporating a properly designed temporal truncation module prior to the frequency-to-time mapping process. This module periodically selects a short section of the continuous telecommunication data signal every certain period of time through electro-optic (EO) modulation. With this integration, D-FTM becomes adaptable to continuous data signals, opening avenues for its application in real-time telecom monitoring.

The schematic of the proposed design for the RTOM system is shown in Fig. 2.2. This is composed of three main units, namely, (i) a periodic temporal sampling unit, (ii) a group velocity dispersive element, and (iii) a high-speed photodetection device. The periodic temporal sampling unit can be implemented through EO intensity modulators, such as a Mach-Zehnder modulator (MZM) configuration [60]. The incoming dynamic data signal, referred to in this work as the signal under test (SUT), is a DWDM telecom data signal. This SUT may encompass both upstream and downstream signals within a telecommunication link, and is assumed to be band-limited with a full bandwidth denoted by $\Delta\omega_s$, comprising all transmitted wavelength channels through the link. In the analysis conducted here, we assume the SUT covers at least the entire C-band without loss of generality. The signal's temporal duration is not subject to additional constraints (e.g., the SUT can be infinitely long). A small portion of the SUT is tapped off the fiber employing a 90:10 2×2 coupler. Then, the upstream and downstream signals are combined using a 50:50 coupler and fed into the RTOM system for monitoring. The SUT is first sampled/truncated using a MZM driven by a periodic radiofrequency (RF) pulse train with a repetition period of T_R, before D-FTM is performed. The sampling pulses have a full-width at half maximum (FWHM) time-width duration of Δt_p, which has to be sufficiently long such that to capture enough data signal information while satisfying the far-field condition for the chosen GVD. The amplitude modulator bandwidth determines the minimum full-width time duration of the sampling pulses. The output of the sampling unit in Fig. 2.2 illustrates the temporally sampled SUT along with its associated frequency spectrum. Subsequently, the sampled signal propagates through the group velocity dispersive unit, thereby time mapping the frequency spectrum of each of the truncated signal sections along the corresponding time analysis window, each with a duration not exceeding the sampling period T_R.

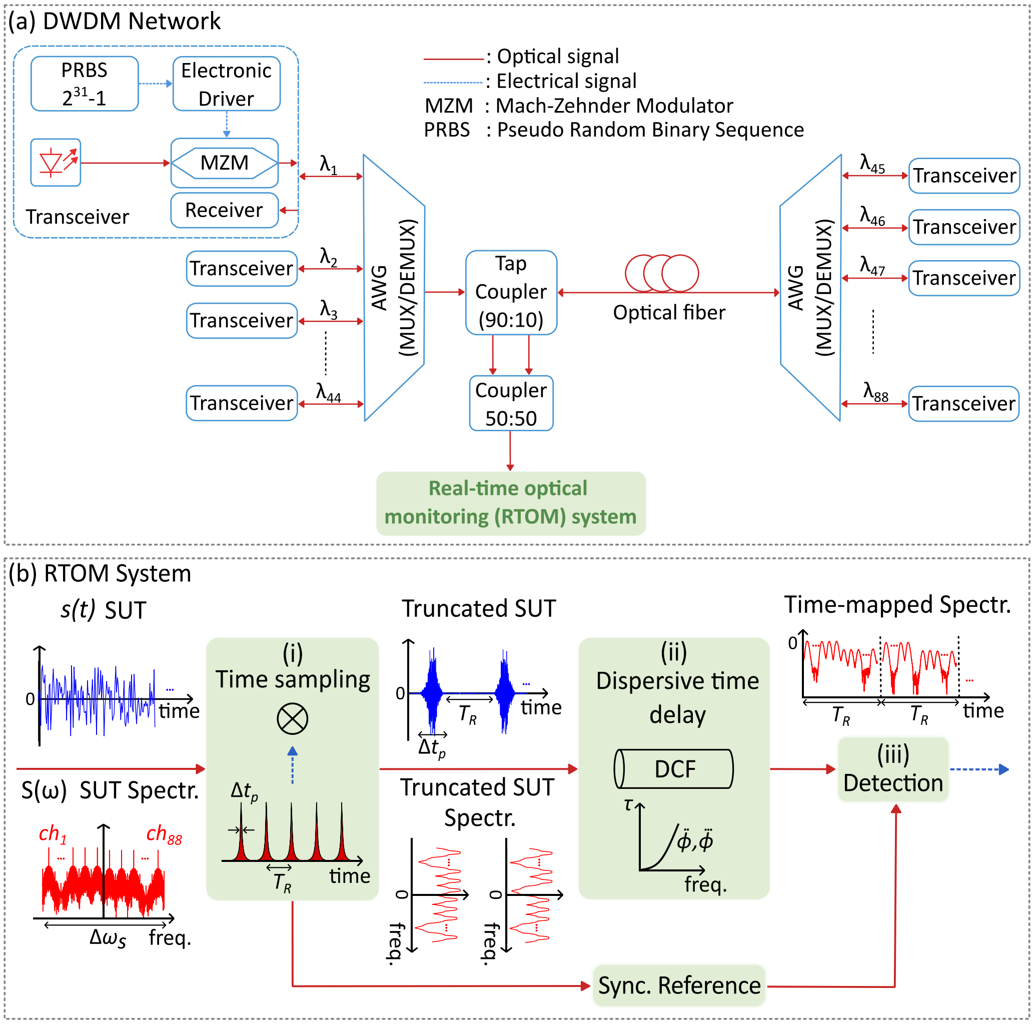

Fig. 2.2 (a) A DWDM network. (b) Schematic of the proposed design for real-time optical monitoring (RTOM) system.

As elaborated in section 2.1, to achieve the frequency-to-time mapping process, one can use a dispersive element providing a linear group delay as a function of frequency [41]. However, practical implementations require consideration of higher-order dispersion effects. Therefore, apart from the so-called GVD, the TOD effect of the dispersive medium is considered in this work for simulations part. In this case, the group delay of the dispersive delay unit, τ, incorporating higher-order dispersion (up to TOD) can be expressed as [61]:

$$\tau = \frac{d\phi(\omega)}{d\omega} = \dot{\phi} + \ddot{\phi}\omega + \frac{1}{2}\dddot{\phi}\omega^2 \tag{2.9}$$

According to Eq. (2.9), when the sampled SUT with a temporal duration of Δt_p goes through the dispersive medium, the spectral components of this signal are temporally realigned [41]. The temporal Fraunhofer approximation ensures that the dispersion effect is strong enough in this realignment process to temporally separate the sampled SUT spectral components. Therefore, the frequency spectrum of the sampled SUT is mapped from the frequency domain to the temporal domain. For a dispersive medium with these variations, the time-to-frequency mapping relation is obtained by simply finding the roots of the quadratic equation of the group delay (i.e. Eq. (2.9)) as follows [61]:

$$\omega' = \frac{-\ddot{\phi} \pm \sqrt{\ddot{\phi}^2 + 2\dddot{\phi}(t-\dot{\phi})}}{\dddot{\phi}} \tag{2.10}$$

where t is the real measured time relative to the center of the output signal, ω' is the relative recovered frequency through mapping, and the sign $\pm$ corresponds to the cases of positive and negative GVD, respectively. The term $t - \dot{\phi}$ is replaced with t for simplicity in this Eq. It should be noted that Eq. (2.10) represents the time-to-frequency mapping relation taking the effect of higher-order dispersion up to TOD into account. A general time-to-frequency mapping relation incorporating all higher-order dispersion terms can be found in [62]. As mentioned earlier, for real-time Fourier transformation to occur, it is necessary to satisfy the temporal Fraunhofer condition. Our proposed system, however, does not have to comply with this condition strictly and can operate under a relaxed Fraunhofer regime, such that the temporal Fraunhofer condition can be generally replaced by the following inequality:

$$|\ddot{\phi}| \geq \Delta t_p^2 / 2\pi \tag{2.11}$$

The system produces a waveform in real-time that follows the spectra of consecutive truncated SUT mapped along a slot of duration T_R, which is captured with a single high-speed photodetector (PD) attached to a real-time oscilloscope (RTO). A moving mean of the power spectral density of the single truncated SUT (done by multiplying an ideal single sampling pulse with the SUT), mapped along the time domain following the law defined in Eq. (2.9), provides a synchronized reference waveform for comparison with the output temporal waveform in dB scale for the simulation results (chapter 3). In the experimental phase of the study, detailed in chapter 4, a waveform obtained from an OSA serves as the reference waveform. An OSA typically measures the power distribution of an optical signal over a specific resolution bandwidth, providing an averaged power reading over a certain period. In contrast, our real-time monitoring system samples the signal at a very fast rate, capturing the instantaneous power levels of the optical signal and any rapid fluctuations between samples. This means we will see the rapid fluctuations in power that might occur from one sample to the next. Hence, to make a meaningful comparison between the results of the RTOM system and the reference OSA, we propose averaging together the outputs of the RTOM system, i.e. multiple consecutive sampled spectra. Using this strategy, the evolving power spectrum of the SUT is obtained by emulating the OSA's behavior. Moreover, adopting this averaging approach, rather than relying on a single measurement of the SUT, avoids the risk of potential misinterpretation between the signal's binary information and a deactivated DWDM channel during sampling intervals, while also improving the signal-to-noise ratio of the performed measurements.

Two relevant figures of merit of the RTOM system are the achievable frequency resolution and the measurement bandwidth. Considering the frequency-to-time mapping law, in order to obtain a target frequency resolution $\delta\omega_r$, the RTOM detection system must be able to capture the output temporal waveforms with a resolution δt_r of at least:

$$\delta t_r \approx |\ddot{\phi}| \times \delta\omega_r \tag{2.12}$$

The resolution $\delta\omega_r$ must be narrow enough to discern two adjacent DWDM channels in the analyzed system. Similarly, the output time-mapped spectrum of each of the sampled sections of the SUT extends over a temporal duration Δt_{out} as follows:

$$\Delta t_{out} \approx \Delta\omega_s \times |\ddot{\phi}| \tag{2.13}$$

where $\Delta\omega_s$ is the total bandwidth of the SUT. A fundamental design condition is that the sampling period T_R must be longer than the temporal duration of the time-mapped spectrum of each sampled SUT portion to avoid overlap among consecutively mapped sections, i.e., $T_R > \Delta t_{out}$. Thus, the sampling period is assumed to satisfy the following condition:

$$T_R = \Delta t_{out} + Margin \tag{2.14}$$

The system's measurement update rate is ultimately limited by the inverse of the sampling period T_R. This period is directly proportional to the magnitude of the dispersion coefficient and it can be customized to relax the detection bandwidth requirements. In particular, Eq. (2.12) implies that one can use a lower photodetection bandwidth (longer δt_r) by using a higher amount of dispersion ($|\ddot{\phi}|$) while maintaining the same frequency resolution. However, there are two essential trade-offs to consider. The first is that the time-mapped spectrum covers a wider Δt_{out} as the GVD amount is increased. Hence, T_R has to be longer to separate consecutive mapped sections, which translates into a correspondingly reduced measurement update rate. Additionally, increasing dispersion also degrades the output waveform dynamic range as each measured spectrum is mapped over a longer time duration with a correspondingly lower local intensity. The dynamic range here refers to the difference between the signal maximum and the signal minimum just above the system noise floor.

In an optical system, optical power budget evaluates the amount of WDM parallelism and the associated insertion loss to maintain reliable system performance. An essential factor in this context is the power threshold that the photodetector must receive. This threshold, known as detector sensitivity, is the minimum optical power required for the photodetector to function effectively and ensure accurate signal detection. The relation between various device limitations and system-level metrics can be expressed as [63]:

$$P - S \geq IL_{max} + 10\, log_{10}\, n \tag{2.15}$$

where P is the system's optical power limit and S is the detector sensitivity, both values are expressed in dBm. The term IL_{max} denotes the insertion loss of the system in dB, and *n* indicates the number of WDM channels. The optical power budget is $P - S$.

3 THEORETICAL AND NUMERICAL SIMULATION RESULTS

This chapter is devoted to the theoretical and numerical simulation results of the proposed real time optical monitoring (RTOM) system. A comprehensive analysis of the impact of different parameters is conducted here. First, system modeling and design parameters are discussed. Then, the optimum value of design parameters including dispersion, Mach-Zehnder modulator (MZM) extinction ratio (ER) used for temporal sampling, and photodetector bandwidth (PD-BW) is determined. Finally, the system's performance and its potential capabilities are evaluated.

3.1 RTOM system modeling and design parameters

Following the scheme shown in Fig. 2.2, here we discuss the modeling of various parts in detail. The simulation model has been implemented using the MATLAB numerical simulation platform. A wavelength-division-multiplexed (WDM) data stream covering the entire optical telecom C-band (1530-1565 nm), i.e. 88 channels, with a channel spacing of almost 50 GHz is being considered here. The WDM channels are modeled as non-coherently and asynchronously related, meaning the signals on each channel are not necessarily in phase and have a random delay with respect to each other. Thus, a random phase between 0 to 2π and a random delay between 0 to bit period (i.e. 1/bit rate) for each channel signal is considered. For signal generation, 25000 symbols of a binary $2^{31}-1$ pseudo-random bit sequence (PRBS) with a 25 Gb/s bit rate are used to drive the MZM of each of the WDM transmitters. This process creates a non-return-to-zero on-off-keying (NRZ-OOK) signal, shown in the transceiver block in Fig. 2.2. We consider a 5 dB extinction ratio on the NRZ-OOK signal with a 0/-5 dB one-level power for downstream/upstream channels to model a more realistic case. The extinction ratio corresponds to the ratio of one-level power to zero-level power in logarithmic scale. The bandwidth limitation of the transmitter is also considered using a fourth-order Gaussian low-pass filter (LPF) with an electrical bandwidth of $0.8 \times bit\ rate$. Thus, noncoherent and asynchronous channel signals operating under NRZ-OOK modulation data format are generated and multiplexed (by MUX) to emulate the SUT. The temporal sampling unit is implemented using a 10-GHz electro-optic MZM biased at $V_\pi = 5\ \mathrm{V}$, while MZM non-idealities such as finite extinction ratio and bandwidth limitation are also considered. Using an arbitrary waveform generator (AWG), short pulses are generated periodically to sample the SUT. The sampling pulses are Gaussian in shape with a full width at half maximum (FWHM) time-width of $\Delta t_p = 100\ \mathrm{ps}$ and a periodicity of T_R. To prevent interference between consecutively mapped spectra at the system output, one must ensure that the sampling pulses are sufficiently separated, as discussed in chapter 2, section 2.2. The time-mapped spectrum of each of the evaluated truncated SUT temporally covers a certain output duration, Δt_{out}. Assuming the maximum GVD as $\ddot{\phi} = \Delta t_p^2/2\pi = 1591.55\ \mathrm{ps}^2/\mathrm{rad}$, the output waveform temporal duration based on Eq. (2.13) is obtained as $\Delta t_{out} \approx 44\ \mathrm{ns}$. The value of the temporal sampling period must be larger than this time interval, i.e., $T_R > \Delta t_{out}$, according to the Eq. (2.14). The added margin can be adjusted as desired. Hence, the sampling period is set to be $T_R = 200\ \mathrm{ns}$ in this analysis. The dispersive delay unit is implemented using a dispersion compensating fiber (DCF) to provide the required second-order dispersion amount dictated by the design condition in Eq. (2.11). The DCF unit is designed to match a dispersion parameter of $D =$ -16.8 ps/nm.Km and a dispersion slope of $S =$ -0.058 ps/nm^2.Km [64]. The output waveform is captured with an avalanche photodiode (APD) plus oscilloscope, the implementation of which involves an APD receiver optical subassembly (ROSA). The APD-ROSA consists of an APD and a transimpedance amplifier (TIA). The APD is assumed to have a gain of $M = 10$ and its 3 dB bandwidth is modelled as a fourth-order Bessel LPF. The APD noise composed of thermal noise and shot noise with a dark current of $I_d = M \times 3 \times 10^{-9}$ A is also emulated. The APD has a minimum sensitivity of -34 dBm and a maximum overload of -5 dBm. The TIA is modelled by a first-order Butterworth LPF having AC transimpedance of $Z_t = 2500\ \mathrm{ohm}$ as well as equivalent input noise current density of $IN = 7.5\ \mathrm{pA}/\sqrt{\mathrm{HZ}}$ [65]. We consider the APD and TIA bandwidths the same here for simplicity, and refer to both as PD-BW hereafter. The total insertion loss (IL_{max}) of the system is attributed to several components: 4 dB from the MUX/DEMUX, 10 dB from the tap coupler, 3 dB from the 50/50 coupler, 3.5 dB from the MZM, and 6.3 dB from the DCF for an ~80 Km long.

Fig. 2.2(b) presents the schematic of the RTOM system along with a numerical example. Before proceeding, a step-by-step analysis of a realistic numerical example is provided in Fig. 3.1 to illustrate how the RTOM system operates. The incoming WDM signal (SUT) is first sampled using a periodic radiofrequency (RF) pulse sequence with a repetition period of $T_R = 200\ \mathrm{ns}$ and a temporal width of $\Delta t_p = 100\ \mathrm{ps}$ ((i) Time sampling). The truncated SUT and its corresponding spectrum are illustrated after time sampling unit. Then, once the sampled signal propagates through DCF ((ii) Dispersive time delay) with dispersion amount of $\ddot{\phi} = 1591.55\ \mathrm{ps}^2/\mathrm{rad}$, the frequency spectrum of the SUT is directly mapped along the time domain, that is, through the so-called frequency-to-time mapping phenomenon. The RTOM system produces a waveform in real-time that follows the spectra of consecutive sampled SUT sections, each mapped along a slot of duration T_R, which are finally captured using a single high-speed photodetector attached to a real-time oscilloscope for digitization ((iii) Detection).

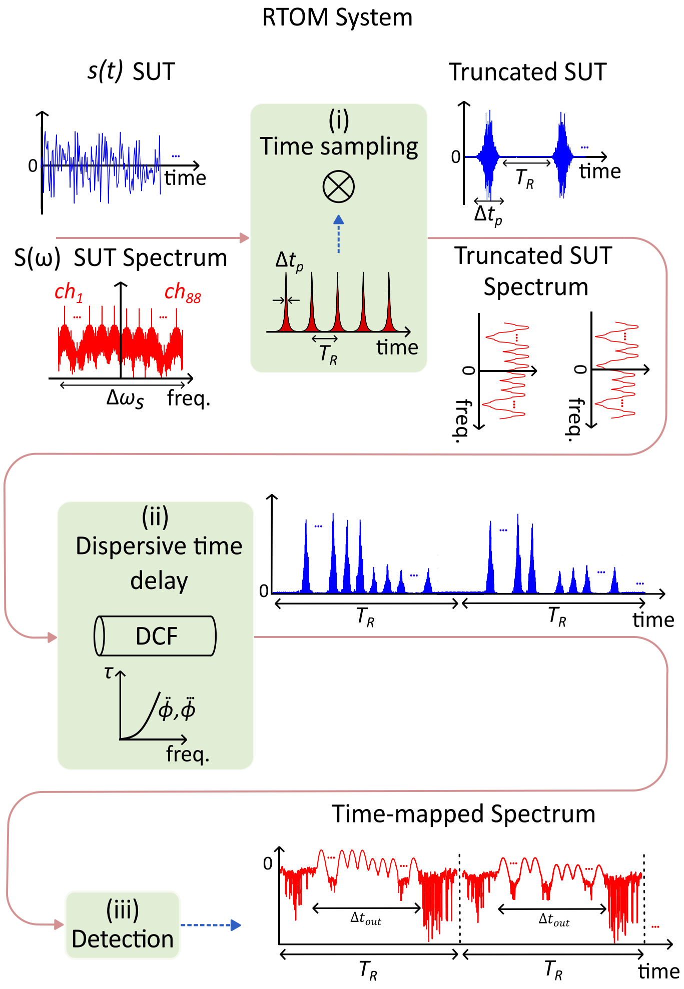

Fig. 3.1 RTOM system operation in each step of analysis.

3.2 RTOM simulation results

This section presents a comprehensive analysis focusing on the impact of various design parameters within the RTOM system. To determine the optimum values for key parameters, such as dispersion, MZM-ER, and PD-BW, we adopt a methodical approach of decoupling the effects of each parameter. This involves isolating the influence of one specific parameter while maintaining near ideal value for the others. We then evaluate the system's performance and capabilities.

3.2.1 Analysis of optimal dispersion value

The simulated input SUT is specifically designed by deactivating some channels and decreasing the one-level power on others to illustrate the sufficient amount of dispersion to capture all changes in the SUT. To this end, Ch_8 and Ch_{55} are deactivated, while Ch_5 and Ch_{10} see reductions in one-level power by -10 dB and -3 dB, respectively. Fig. 3.2. illustrates the system output corresponding to different dispersion values, assuming an MZM-ER of 60 dB and a PD-BW of 2.5 GHz. The figure provides a zoomed-in view of the first sample of the SUT, T_{R1}, for enhanced visualization. A detailed view is also provided for a segment of the output waveform, displaying Ch_1 to Ch_{10}. The moving mean of the single truncated SUT's power spectral density, translated into the time domain according to the frequency-to-time mapping law defined in Eq. (2.9), serves as a reference waveform for comparison with the RTOM output waveform.

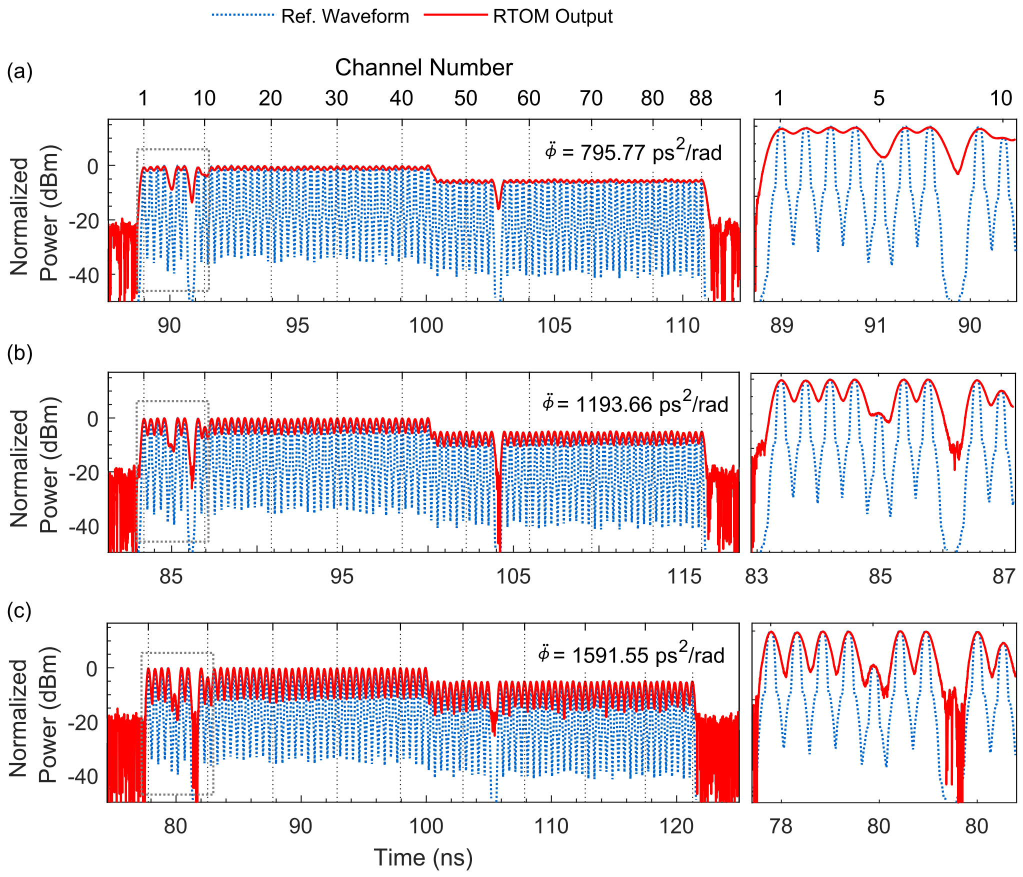

Fig. 3.2 Numerical simulation illustrating the effect of dispersion amount on the RTOM output waveform's evolution.

RTOM Output temporal waveform compared with the reference waveform, considering MZM-ER = 60 dB and PD-BW = 2.5 GHz, for (a) $\ddot{\phi} = 795.77\ \mathrm{ps^2/rad}$ (equivalent loss = 3.62 dB), (b) $\ddot{\phi} = 1193.66\ \mathrm{ps^2/rad}$ (equivalent loss = 4.82 dB), and (c) $\ddot{\phi} = 1591.55\ \mathrm{ps^2/rad}$ (equivalent loss = 6.03 dB).

To determine the required dispersion value, we changed the dispersion amount to see at what point one obtains the needed information, i.e. the Fourier transform of the truncated part of the SUT. As shown in Fig. 3.2(a)-(c), by changing the dispersion value from $\ddot{\phi} = 795.77\ \mathrm{ps}^2/\mathrm{rad}$ to $\ddot{\phi} = 1591.55\ \mathrm{ps}^2/\mathrm{rad}$, the output waveform gradually approaches the reference waveform. In other words, despite not strictly satisfying Fraunhofer's condition here, one can obtain an acceptable amount of frequency-to-time mapped information. Thus, the required dispersion value in the proposed system can be decreased to as low as $\ddot{\phi} \approx \Delta t_p^2/2\pi$ (i.e. $1591.55\ \mathrm{ps}^2/\mathrm{rad}$ which corresponds to ~74 km single mode fiber (SMF) length with 6.03 dB loss).

3.2.2 Analysis of temporal sampling modulator extinction ratio (MZM-ER)

The impact of finite ER of realistic MZMs used for temporal modulation on the RTOM system performance is then investigated, determining the minimum ER required for satisfactory operation. The ER value is defined as the ratio of the maximum to the minimum transmission power. For this analysis, the same SUT as discussed in section 3.2.1 is used. Fig. 3.3 depicts the RTOM system output under different MZM ERs. The system shows a poor performance under ERs of 20 dB and 30 dB. However, an acceptable and very similar result can be obtained with ERs ranging from 40 dB to 60 dB. As a result, an ER = 40 dB is chosen, providing a nearly optimal result concerning the output dynamic range.

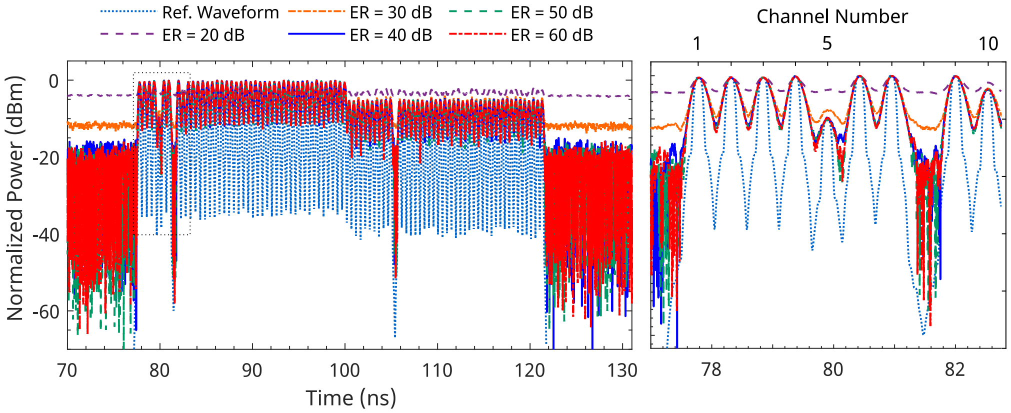

Fig. 3.3 Numerical simulation illustrating the effect of MZM-ER on the RTOM output waveform's evolution, considering $V_\pi = 5$ V, MZM-loss = 3.5 dB, $\ddot{\phi} = 1591.55\ \mathrm{ps}^2/\mathrm{rad}$, and PD-BW = 2.5 GHz.

3.2.3 Evaluation of photodetection system bandwidth (PD-BW)

The next crucial limiting effect that one must consider is the bandwidth of the photodetection system, including both APD and TIA bandwidth. These bandwidths are assumed to be identical in the proposed system for simplicity. To decouple the impact of parameters and study the specific effect of PD-BW, we set other parameters to their best-performing values, i.e. $\ddot{\phi} = 1591.55\ \mathrm{ps^2/rad}$ and MZM-ER = 60 dB. Fig. 3.4 illustrates the output temporal waveform compared with the reference waveform for different PD-BW values. Zooming over Ch$_1$ to Ch$_{10}$ is also displayed. Upon increasing the PD-BW from 1 GHz to 10 GHz, the output waveform follows the reference waveform with more details, such that the output waveform captured at 10 GHz closely resembles the reference waveform. Interestingly, even at a lower bandwidth of 2.5 GHz, the system demonstrates an acceptable trend, as evidenced in Fig. 3.4(b). This finding suggests that while higher bandwidths enhance the alignment between the output and reference waveforms significantly, satisfactory system performance can still be achieved at lower bandwidths. Thus, PD-BW = 2.5 GHz is chosen to achieve a good compromise in terms of cost and performance.

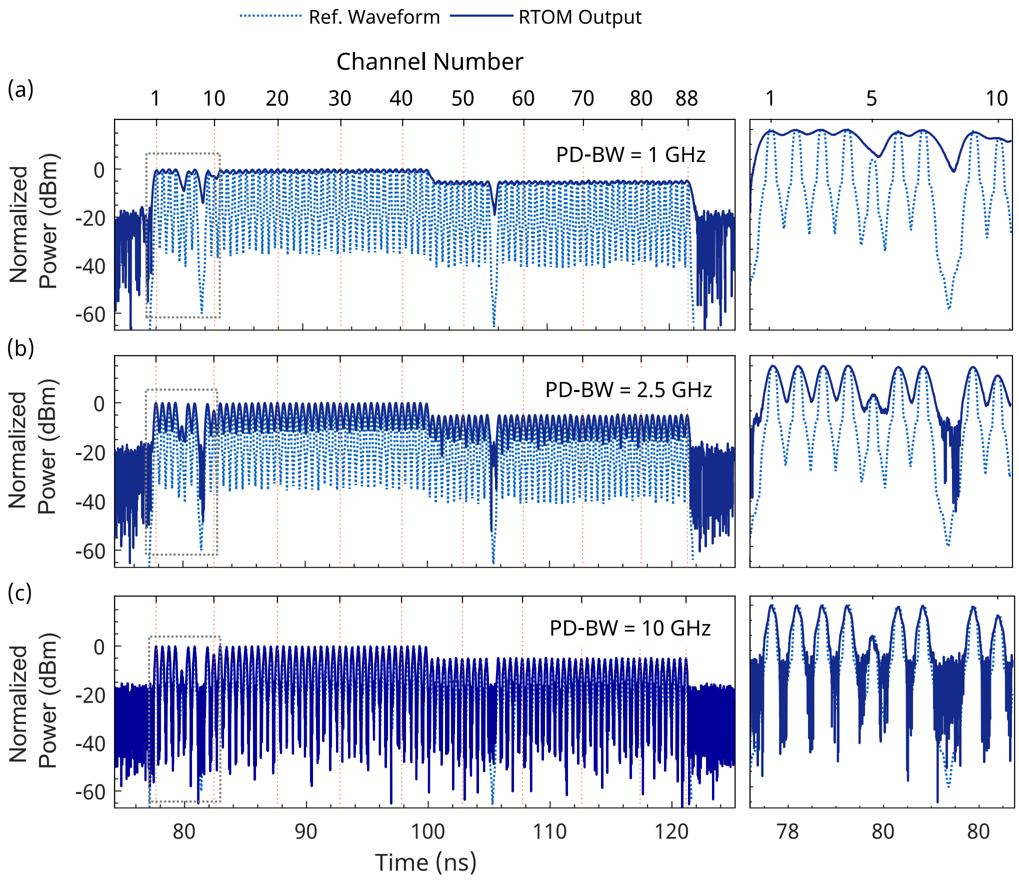

Fig. 3.4 Numerical simulations assessing the impact of different photodetection bandwidth (PD-BW) on the RTOM system's performance.

The output temporal waveform of the RTOM system at PD-BWs of (a) 1 GHz, (b) 2.5 GHz, (c) 10 GHz. Other parameters set at $\ddot{\phi} = 1591.55\ \mathrm{ps^2/rad}$ and $\mathrm{MZM\text{-}ER} = 60\ \mathrm{dB}$.

3.2.4 Analysis of the RTOM system performance

In this subsection, we assess the accuracy of the RTOM system's performance concerning the equivalent frequency and power level of WDM channels. For this analysis, we considered all channels active and adjusted the one-level power of some channels period by period for ten samples, as detailed in Table 3.1. To evaluate the performance accuracy in terms of power defined for WDM channels, we kept all channels active at their default one-level powers (i.e. 0/- 5 dB for downstream /upstream channels). Fig. 3.5 shows the obtained results of this analysis. In both Fig. 3.5(a) and (b), the average value obtained from ten measurements is very close to the nominal value, i.e. 340 MHz for equivalent frequencies and ~-0.4/-5.4 dB for one-level power of downstream/upstream channels. The standard deviation for each channel frequency and one-level power is also very close to zero, i.e. 3 GHz and ~0.4 dB, respectively. This indicates a high degree of precision in the RTOM system's performance.

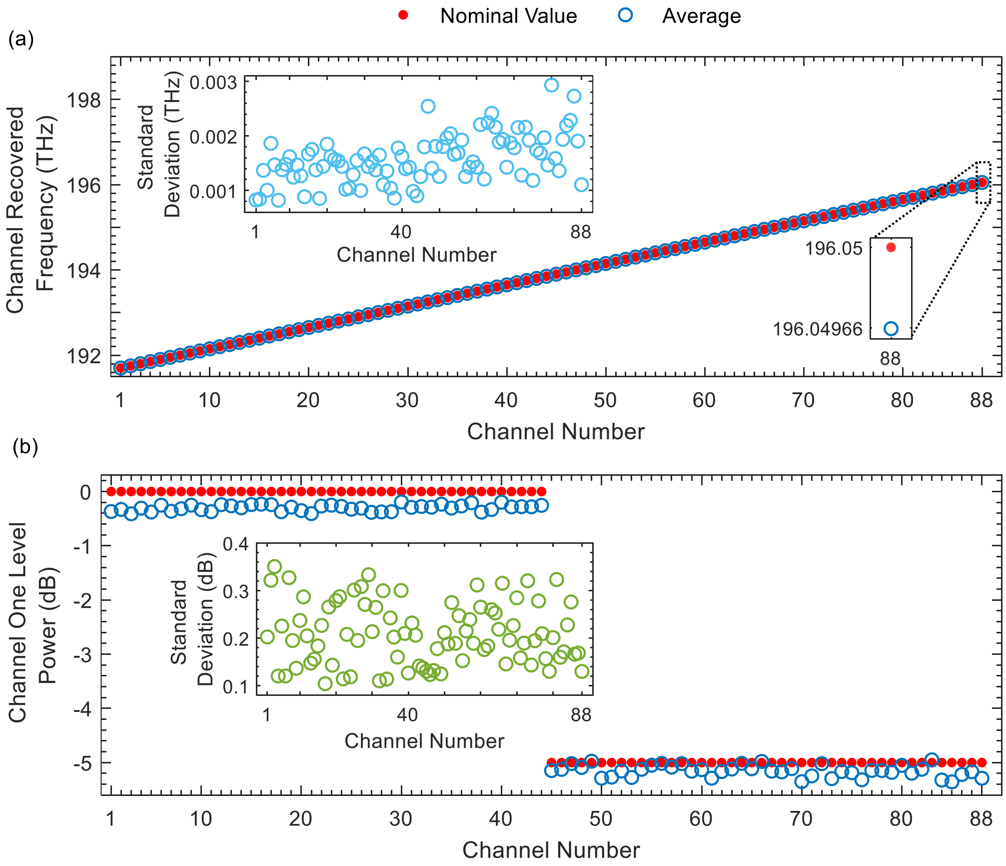

Fig. 3.5 Numerical simulations to evaluate system accuracy considering 10 samples of the SUT. The results obtained with design parameters of $\ddot{\phi} = 1591.55\ \mathrm{ps^2/rad}$, $\mathrm{MZM\text{-}ER} = 40\ \mathrm{dB}$, and $\mathrm{PD\text{-}BW} = 2.5\ \mathrm{GHz}$ for (a) equivalent frequency of WDM channels and (b) one-level power of WDM channels.

Table 3.1 Modification introduced to the power of some channels across ten analysis periods.

Analysis Period	Power Reduced Channels	Power Reduction Amount (dB)
Sample 1 ($\boldsymbol{T_{R1}}$)	Ch_5, Ch_{10}	-10, -5
Sample 2 ($\boldsymbol{T_{R2}}$)	Ch_{20}, Ch_{50}	-7, -3
Sample 3 ($\boldsymbol{T_{R3}}$)	Ch_{40}, Ch_{70}	-7,-3
Sample 4 ($\boldsymbol{T_{R4}}$)	Ch_{25}, Ch_{30}	-10, -7
Sample 5 ($\boldsymbol{T_{R5}}$)	Ch_1, Ch_{88}	-5, -3
Sample 6 ($\boldsymbol{T_{R6}}$)	Ch_4, Ch_{13}	-3, -10
Sample 7 ($\boldsymbol{T_{R7}}$)	Ch_{37}, Ch_{80}	-5, -3
Sample 8 ($\boldsymbol{T_{R8}}$)	Ch_{21}, Ch_{51}	-5, -3
Sample 9 ($\boldsymbol{T_{R9}}$)	Ch_{11}, Ch_{61}	-3, -5
Sample 10 ($\boldsymbol{T_{R10}}$)	Ch_9, Ch_{77}	-5,-3

Having obtained the optimal design parameters for the RTOM system, including $\ddot{\phi} = 1591.55\ \mathrm{ps}^2/\mathrm{rad}$, MZM-ER = 40 dB, and PD-BW = 2.5 GHz, the system was then designed for an optimized condition. To this end, we designed a specific input SUT to demonstrate the unique capability of the RTOM system for real-time capturing changes occurring along the input signal as fast as a nanosecond scale. We introduced variations over time in different WDM channels of the SUT during each analysis period, each lasting a duration of T_R. As described in section 3.1, the channels were set to have random phases ranging from 0 to 2π and random delays ranging from 0 to bit period (i.e. 1/bit rate) with respect to each other. Several modifications were implemented on the SUT. These included reducing the one-level power of some channels in each analysis period, switching specific channels on or off between periods, and altering the phase of reactivated channels randomly from period to period. Table 3.2 documents these modifications in Details. Fig. 3.6 shows the RTOM system's output waveforms, which are the time-mapped spectra for five consecutive samples of the input SUT, compared to their corresponding reference waveforms. Each of the mapped spectra spreads over a single temporal sampling period of 200 ns. The figure has been zoomed in here by cutting out most of the margin added to Δt_{out} in Eq. (2.14) for better visualization. It can be observed that the output temporal waveform and the reference waveform are in remarkable agreement, proving the system's ability to accurately track and reflect all the introduced changes in the SUT.

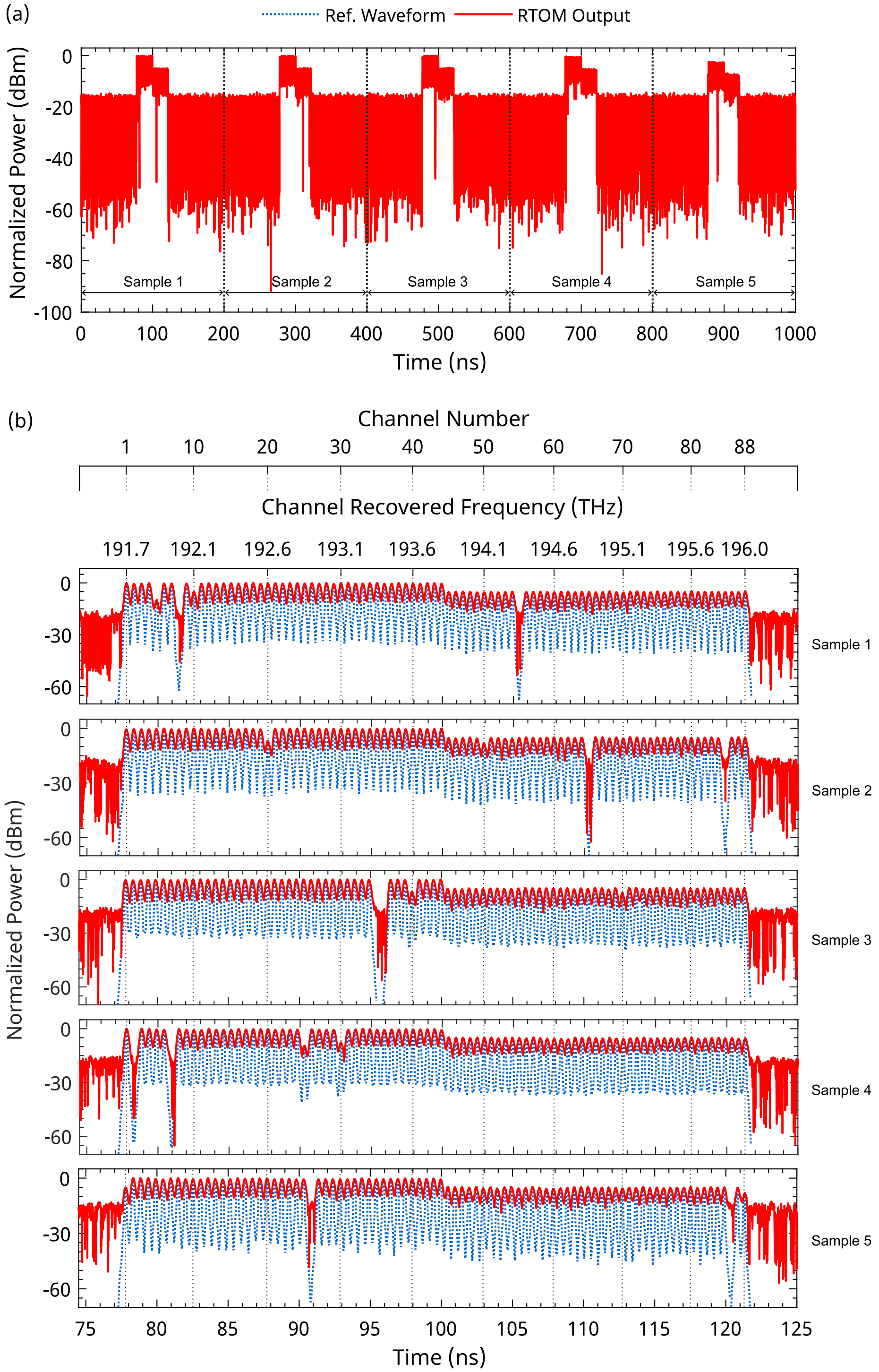

Fig. 3.6 Numerical simulation demonstrating the RTOM system's performance when analyzing a dynamically changing input SUT that varies in each analysis period. (a) System overall output for the varying SUT, (b) System output for each of the five consecutive samples.

Table 3.2 Modification introduced to the WDM channels across each analysis period.

Analysis Period	Deactivated Channels	Power Reduced Channels	Power Reduction Amount (dB)
Sample 1 ($\boldsymbol{T_{R1}}$)	Ch$_{8}$, Ch$_{55}$	Ch$_{5}$, Ch$_{10}$	-10, -5
Sample 2 ($\boldsymbol{T_{R2}}$)	Ch$_{65}$, Ch$_{85}$	Ch$_{20}$, Ch$_{50}$	-7, -3
Sample 3 ($\boldsymbol{T_{R3}}$)	Ch$_{35}$, Ch$_{36}$	Ch$_{40}$, Ch$_{70}$	-7,-3
Sample 4 ($\boldsymbol{T_{R4}}$)	Ch$_{2}$, Ch$_{7}$	Ch$_{25}$, Ch$_{30}$	-10, -7
Sample 5 ($\boldsymbol{T_{R5}}$)	Ch$_{26}$, Ch$_{86}$	Ch$_{1}$, Ch$_{88}$	-5, -3

To simulate a more realistic telecommunications environment, the designed SUT was first dispersed by propagating along a single-mode fiber (SMF), prior to being tapped off the fiber and fed into the RTOM system. This dispersion was implemented considering a 20 Km long SMF with a second-order dispersion coefficient $\beta_2 = -21.7\ \mathrm{ps^2/Km}$ and a dispersion slope $S = 0.032\ \mathrm{ps/nm^2.Km}$. Fig. 3.7 shows the output temporal waveform obtained for the first sample of the dispersed SUT. As expected, the output waveform accurately follows the reference waveform, confirming the system's accuracy and effectiveness in real-world scenarios.

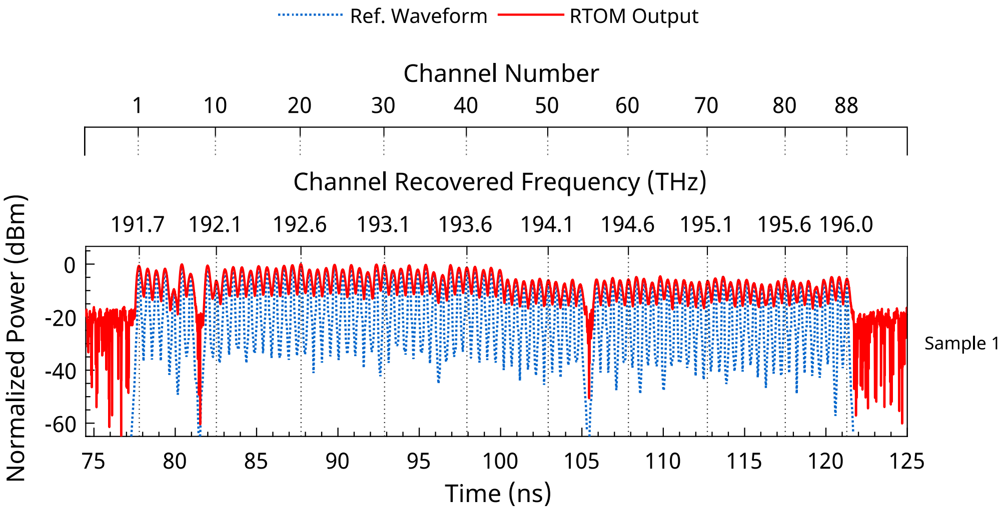

Fig. 3.7 Numerical simulation showing system performance with a dispersed dynamic input SUT changing analysis period to period. The output waveform corresponds to the first sample of the dispersed SUT.

3.2.5 Power budget and dynamic range under various system parameters

Using Eq. (2.15) and considering the system total insertion loss $IL_{max} = 26.8\ dB$, we calculated the system's minimum input power to be $P_{min} = -7.2\ \mathrm{dBm}$ when only a single WDM channel is active. Conversely, with all 88 channels in operation, the maximum input power was established to be $P_{max} = 41.24\,\mathrm{dBm}$. Fig. 3.8 shows how different system parameters influence the output temporal waveform dynamic range, defined as the difference between the signal's maximum and minimum levels just above the system noise floor. The dynamic range have been estimated here assuming a 100% tap coupler ratio. From Fig. 3.8(a), one can infer that TIA noise plays a crucial role concerning the dynamic range, such that increasing the equivalent input noise current density of TIA can significantly decrease the dynamic range. This effect is attributed to the TIA noise setting the noise floor of the photodetection system (APD noise is negligible compared to TIA noise). Consequently, the more TIA noise ROSA has, the higher the noise floor of the photodetection system is, and the more limited the dynamic range becomes. Fig. 3.8(b) highlights the relationship between the MZM-ER and the dynamic range. We can see that an increase in the MZM-ER leads to an enhancement in the dynamic range. Taking the ROSA noise into account, the dynamic range gets saturated around MZM-ER = 40 dB. The PD-BW effect is also illustrated in Fig. 3.8(c).

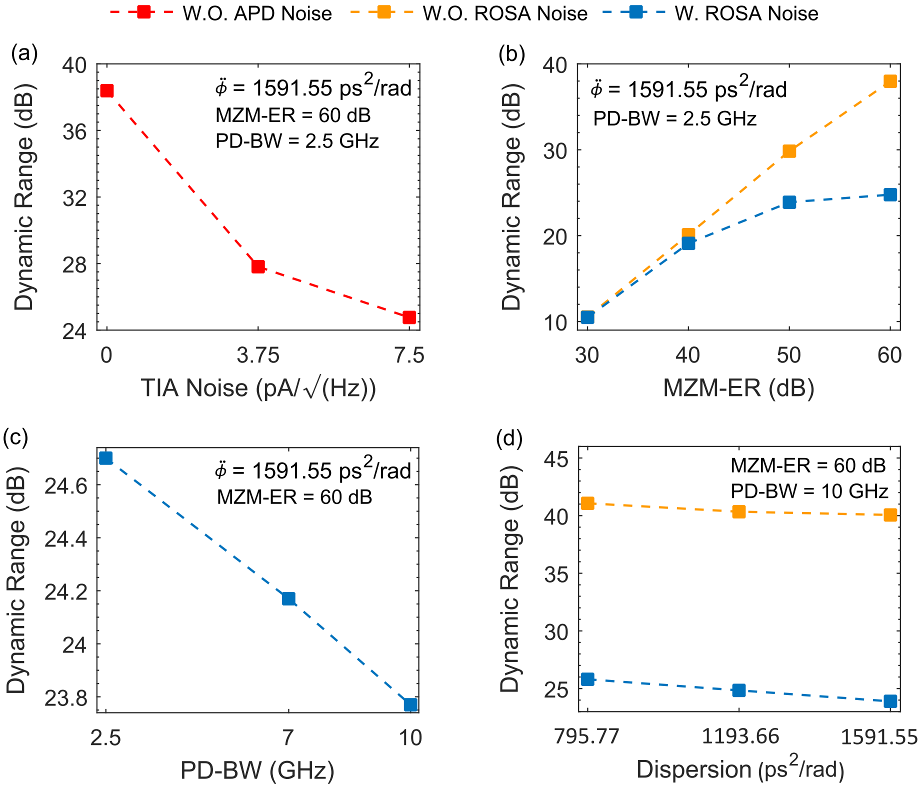

Fig. 3.8 The influence of various system parameters, including (a) TIA noise, (b) MZM-ER, (c) PD-BW, and (d) DCF module dispersion value, on the output temporal waveform dynamic range.

Given the relation between the equivalent input noise of TIA and the PD BW, broadening the BW amplifies the equivalent input noise, thereby reducing the dynamic range. Lastly, Fig. 3.8(d) shows the impact of increased dispersion introduced by DCF on the dynamic range. Increasing dispersion degrades the output waveform dynamic range as each measured spectrum is mapped over a longer time duration with a correspondingly lower local intensity. While this reduction in dynamic range is obvious, it is not as pronounced as the effects of the other parameters.

3.2.6 RTOM system versatility

3.2.6.1 Various transmitter types and bit rates

The results presented so far were based on using a Mach-Zehnder Modulator (MZM) as the optical transmitter. To broaden the scope of our analysis, we then extended our examination to include other transmitter types, specifically directly modulated laser (DML) and electro absorption modulated laser (EML). RTOM Design parameters set to their best value, i.e. $\ddot{\phi} = 1591.55\ \mathrm{ps}^2/\mathrm{rad}$, MZM-ER = 40 dB, and PD-BW = 2.5 GHz. The analyzed SUT is the same as one defined in Fig. 3.6. RTOM system's output temporal waveform for the first sample of the SUT employing DML transmitters and a combination of MZM, EML, and DML transmitters is illustrated in Fig. 3.9(a-b). As expected, the RTOM system demonstrated consistent functionality regardless of the type of optical transmitter employed, underscoring its versatility and robustness in different transmission environments.

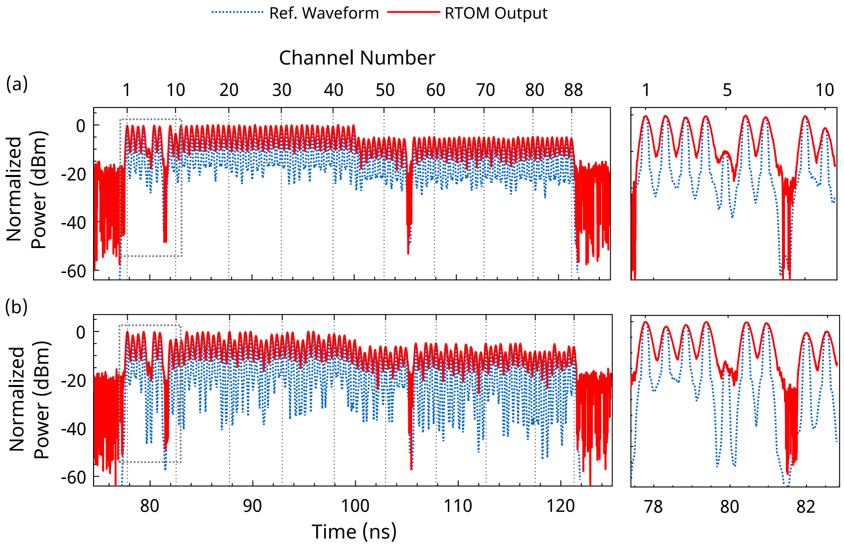

Fig. 3.9 RTOM system output using various optical transmitters. (a) DML transmitters, and (b) a combination of MZM, EML, and DML transmitters.

Furthering our assessment of the RTOM system, we conducted tests across various bit rates to evaluate its adaptability and efficiency under diverse operational conditions. Fig. 3.10(a-d) presents the output waveform for bit rates of 1 Gb/s and 10 Gb/s under two distinct scenarios, i.e., for the first sample of the designed SUT and with a single active channel in operation. These findings confirm the RTOM system's ability to maintain effective and reliable performance across a range of different bit rates, further validating its applicability for versatile communication needs.

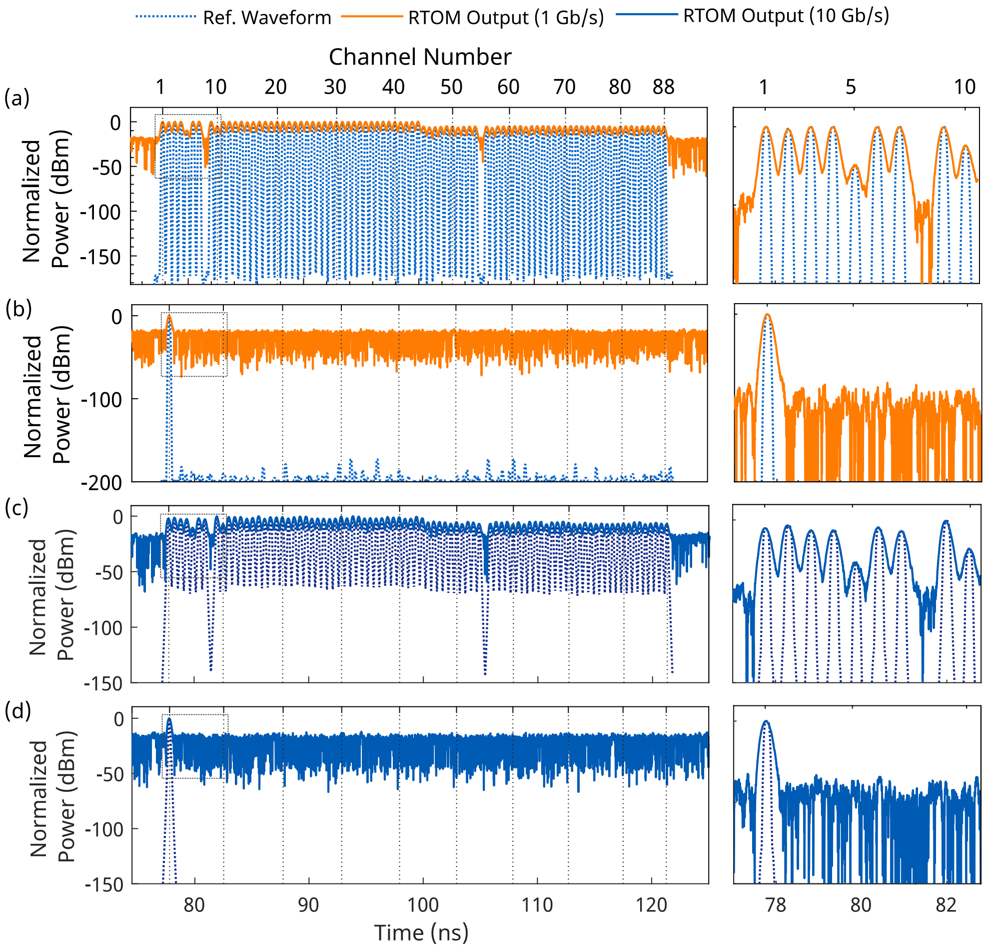

Fig. 3.10 RTOM system's ability to efficiently operate across different bit rates in two scenarios. The system's output waveform at (a) 1 Gb/s, (b) 1 Gb/s (single channel active), (c) 10 Gb/s, (d) 10 Gb/s (single channel active).

3.2.6.2 Complex modulation formats and higher bit rates

Finally, we illustrate the RTOM versatility to analyze coherent modulation formats, such as the quadrature amplitude modulation (QAM) commonly employed in high-capacity optical communication systems. The RTOM performs more efficiently at higher bit rates. A single sample of a higher baud rate signal captures several consecutive symbols, providing the RTOM scheme with more data signal information. Additionally, high-capacity systems have higher per channel bandwidth (~100 GHz). The ability to resolve broader frequency channels implies that the RTOM can be designed to offer a more relaxed frequency resolution, requiring less dispersion amount. Fig. 3.11 presents the numerical analysis for the first sample of a 100 Gb/s 16-QAM signal, covering the entire C-band with 100 GHz channel spacing and ~30 GHz per channel bandwidth. The dispersion amount is set to $\ddot{\phi} = 795.77\ \mathrm{ps}^2/\mathrm{rad}$. The reported results corroborate that the RTOM analysis is agnostic to the modulation format and baud rate, as long as the per channel bandwidth of the data signal is within the design frequency resolution.

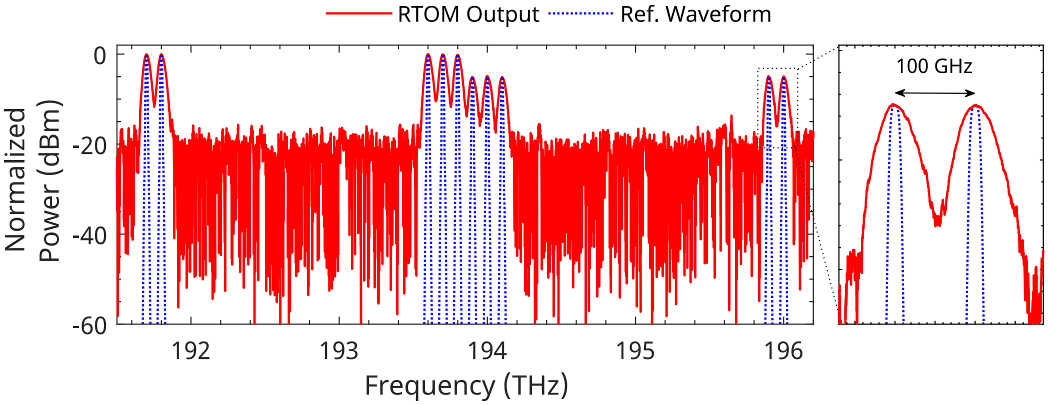

Fig. 3.11 RTOM trace obtained for the SUT with coherent modulation format of 16QAM and 100 Gb/s bit rate, spanning the full C-band.

To explore the RTOM's capabilities in higher bit rate scenarios (i.e. significantly exceeding 100 Gb/s), we also conducted an analysis on a 400 Gb/s 16-QAM data signal with 200 GHz channel spacing across the entire C-band. Fig. 3.12 presents the RTOM result. In this case, the SUT is generated using 40000 symbols obtained from a PRBS of length $2^{31} - 1$. Higher bit rates typically involve broader frequency channels. This aspect works to the advantage of our design as it requires a more relaxed frequency resolution. The need for higher resolution is directly tied to the amount of dispersion required in the system – the finer the resolution needed, the greater the dispersion necessary. However, with broader frequency channels associated with higher bit rates, our system can operate effectively with a lower amount of dispersion. Hence, the dispersion amount is now further reduced to $\ddot{\phi} = 477.46\ \mathrm{ps}^2/\mathrm{rad}$. This reduces the complexity and (potentially) the cost of the system, while still achieving the desired performance in terms of spectral analysis and monitoring. In addition, with this reduced dispersion, the output time mapped spectrum of each sampled section of the SUT extends over a shorter temporal duration (denoted as Δt_{out}). In practical terms, this means that the RTOM system can perform the target optical signal spectrum analysis at a faster rate, thereby enhancing its suitability for real-time monitoring applications where speed is a critical factor. This result demonstrates the system's capability to accurately monitor and analyze signals with complex modulation schemes and high data rates, thereby confirming its applicability to high-capacity coherent scenarios.

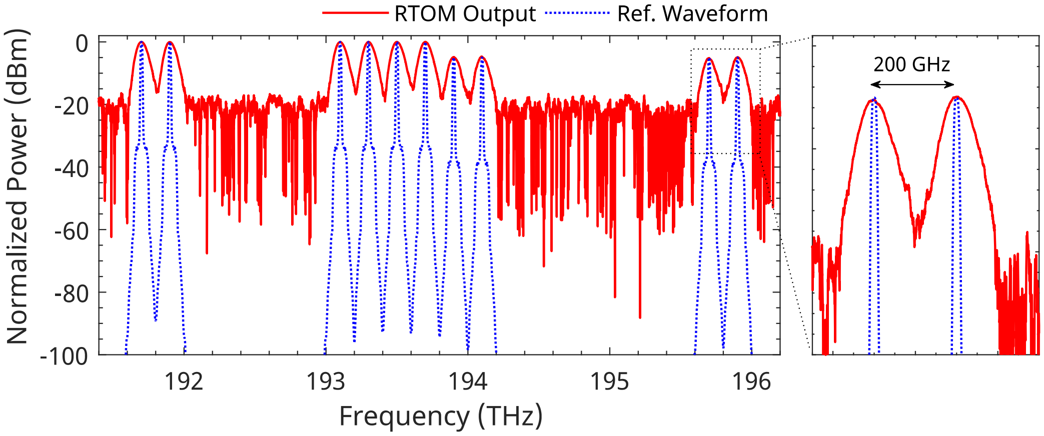

Fig. 3.12 RTOM trace obtained for the SUT with coherent modulation format of 16-QAM and 400 Gb/s bit rate, spanning the full C-band.

4 EXPERIMENTAL RESULTS

This chapter is dedicated to presenting the experimental results of our study, centered on the monitoring of DWDM signals with channel spacing of 50 GHz and 100 GHz. The generated signal under tests (SUTs) for experiments encompass a combination of bit rates, ranging from 1 Gb/s to 25 Gb/s, and different modulation formats including Mach-Zehnder Modulator (MZM) and directly modulated laser (DML). In the experimental setup, we considered two distinct values for key parameters such as dispersion ($\ddot{\phi}$), sampling pulse width (Δt_p), and sampling pulse period (T_R). The comprehensive analysis of the main results is presented through this chapter. Further details and extended examples of certain cases are available in the Appendix section.

4.1 Experimental setup

The setup used for proof-of-concept experiments and its schematic are shown in Fig. 4.1. The system setup is organized into three primary sections: the SUT, the transmission module, and the RTOM system. The RTOM system is composed of a 10-GHz MZM with extinction ratio of ~45 dB, driven by a sampling pulse train with a time width of $\Delta t_p = 100\ \mathrm{ps}$ generated from a 92-GSa/s arbitrary waveform generator (AWG, Keysight M8196A), and a dispersion compensating fiber (DCF) with a dispersion of $\ddot{\phi} = -1328\ \mathrm{ps/nm}$. The detection system consists of a 7-GHz APD-ROSA connected to a 28-GHz RTO (Agilent DSO-X 92804A). The data streams are pseudo random bit sequence (PRBS) non-return-to-zero on-off keying (NRZ-OOK) signals. A tunable continuous wave (CW) laser operating in the C-band (IDPHOTONICS CoBrite), a data signal generator, and a small form factor pluggable (SFP) optical transceiver were utilized to generate the SUT with varying bit rates and modulation formats, including MZM and DML. To modulate the test waveform on the tunable CW laser channels, a 40-GHz MZM driven by another channel of the 92-GSa/s AWG was employed. The data stream was encoded on CW laser channels simultaneously using a single MZM for experimental convenience. The channels from the data signal generator with MZM format and the optical transceiver with DML modulation format were combined and amplified using an Erbium Doped Fiber Amplifier (EDFA PriTel). This signal was then merged with two other channels generated by the CW laser. An EDFA was then utilized to amplify the combined signals, forming the DWDM data signal that serves as the SUT. To produce a more realistic SUT, this amplified DWDM data signal was additionally transmitted through a 2-km single mode fiber (transmission module).

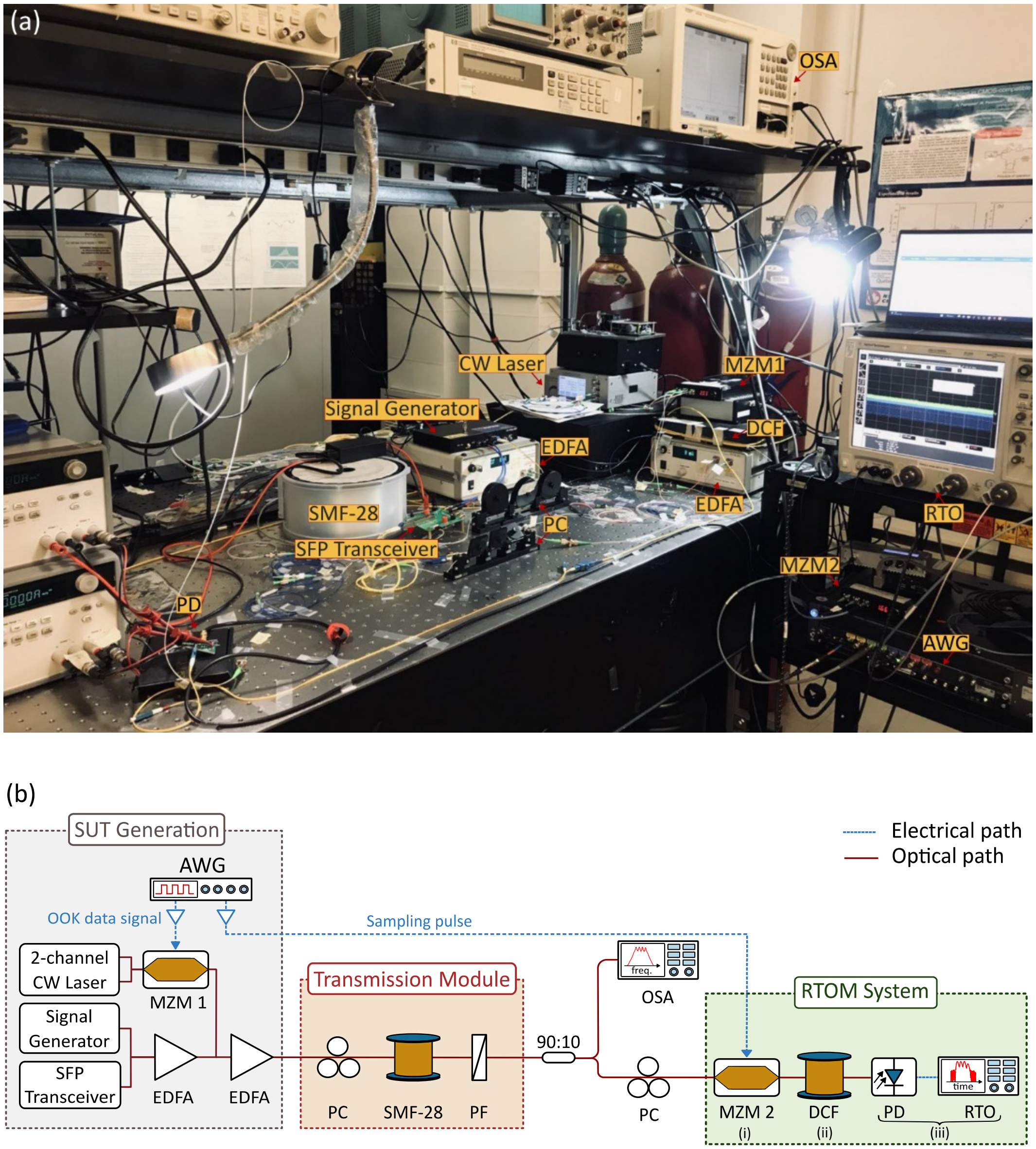

Fig. 4.1 (a) Experimental setup, (b) Experimental setup schematic. The insets show the signal generation and RTOM system.

SUT: signal under test, AWG: arbitrary waveform generator, MZM: Mach Zehnder modulator (MZM 1: 40 GHz, MZM 2: 10 GHz), SFP: small form factor pluggable optical transceiver, EDFA: erbium doped fiber amplifier, PC: polarization controller, SMF-28: single mode fiber, PF: polarization filter, OSA: optical spectrum analyzer, DCF: dispersion compensating fiber, PD: photodetector, RTO: real-time oscilloscope.

A high-resolution optical spectrum analyzer (OSA) was used to obtain the reference waveform. For a more meaningful comparison, we performed post-signal processing on the acquired results. Specifically, the frequency responses from the OSA were smoothed using Gaussian mask convolution to achieve a resolution bandwidth of 12.5 GHz. Additionally, the output temporal waveforms from the RTOM system were filtered through a Gaussian low-pass filter. This filtering process was necessary to eliminate noise originating from the 28-GHz RTO and to adapt the waveforms to a 100 ps pulse width. It should also be mentioned that in the experimental results, the third-order dispersion (TOD) effect was ignored due to its negligible impact. Detailed characterization of the employed DCFs is available in the Appendix section.

4.2 Experimental results and discussion

We first demonstrate the functionality of the RTOM system for simultaneous real-time tracking of the multiple wavelength channels of a SUT possessing different data rates and modulation formats over a wide frequency band, nearly covering the full C-band. We analyze a signal (SUT_1) composed of four data streams located at four different central wavelengths, namely, $\lambda_1 = 1565\ \mathrm{nm}$, $\lambda_2 = 1556.1\ \mathrm{nm}$, $\lambda_3 = 1541.33\ \mathrm{nm}$, $\lambda_4 = 1540.94\ \mathrm{nm}$ with modulation format of DML for Ch_2 and MZM for the other channels. The data streams have a length of $2^{13} - 1$, $2^{31} - 1$, $2^{13} - 1$, and $2^{31} - 1$ at data rates of 1 Gb/s, 25 Gb/s, 1 Gb/s, and 25 Gb/s, respectively (the specifications are summarized in Table 4.1). The SUT_1 is fed to the RTOM system, where it undergoes time sampling using the following parameters: period $T_R = 208.7\ \mathrm{ns}$ and time width $\Delta t_p = 100\ \mathrm{ps}$. As discussed in section 2.2, the time-width duration of the sampling pulses must be sufficiently long to capture enough data signal information while satisfying the far-field condition for the chosen GVD. As demonstrated here, the desired spectral information can be accurately recovered even when the sampling pulse width is significantly shorter than the bit period of the data streams in the SUT. Notice that the sampling time width is about 10 times shorter than the bit period of the streams at 1 Gb/s. Fig. 4.2 shows the spectral trace measured using the RTOM system, obtained from averaging 239 consecutive samples, where it is compared with the reference waveform obtained from a spectral measurement using a conventional OSA with 0.1 nm (~12.5 GHz) resolution bandwidth. As discussed in chapter 2, section 2.2, employing an averaging strategy, which mimics the behavior of optical spectrum analyzers (OSAs), is more effective than relying on a single measurement of the SUT. This approach not only mitigates the risk of misinterpreting binary signal information as a deactivated DWDM channel during sampling but also enhances the signal-to-noise ratio of the measurements. Averaging 239 consecutive samples yields a refresh rate of $208.7\ \mathrm{ns} \times 239$, which is ~50 μs. The inset plot provides a closer look at the output waveform specifically for Ch_3 and Ch_4, separated by 50 GHz. There is a fairly good agreement between the obtained time-mapped spectrum and the reference spectrum, demonstrating the accuracy and reliability of the RTOM system for optical spectrum analysis over a broad frequency range and with sufficient resolution.

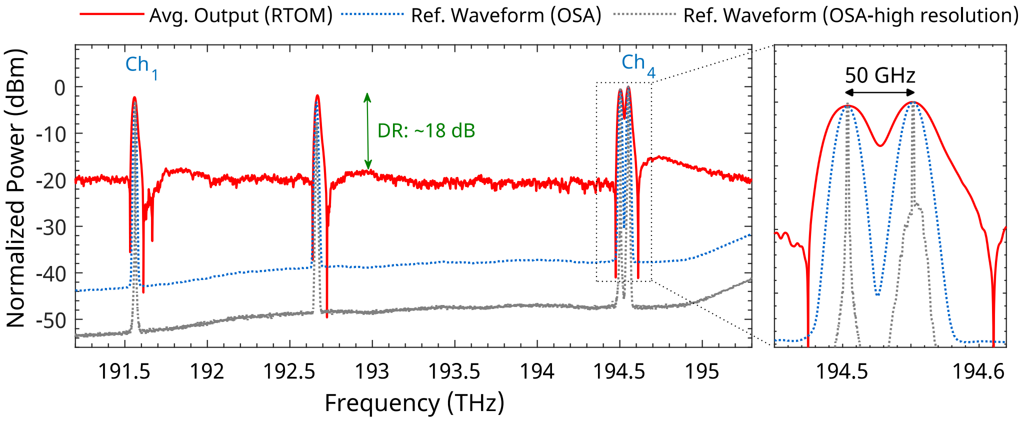

Fig. 4.2 RTOM trace corresponding to the SUT spanning almost the entire C-band.

The SUT consists of four WDM channels operating at different modulation formats (Ch_2:DML, the other channels: MZM) and bit rates (Ch_1-Ch_3: 1 Gb/s, Ch_2-Ch_4: 25 Gb/s). The time sampling parameters are set at $T_R = 208.7$ ns and $\Delta t_p = 100$ ps. The system operates with a dispersion amount of $\ddot{\phi} = -1328$ ps/nm.

Table 4.1 Designed SUTs specifications.

SUT	Channels Wavelength [nm]	Bit Rate [Gb/s]	Modulation Type	PRBS Length
SUT_1	$\lambda_1 = 1565$	1	MZM	$2^{13}-1$
	$\lambda_2 = 1556.1$	25	DML	$2^{31}-1$
	$\lambda_3 = 1541.33$	1	MZM	$2^{13}-1$
	$\lambda_4 = 1540.94$	25	MZM	$2^{31}-1$
SUT_2	$\lambda_1 = 1556.1$	25	DML	$2^{31}-1$
	$\lambda_2 = 1541.73$	1	MZM	$2^{13}-1$
	$\lambda_3 = 1541.33$	1	MZM	$2^{13}-1$
	$\lambda_4 = 1540.94$	25	MZM	$2^{31}-1$
SUT_3	$\lambda_1 = 1550.52$	1	MZM	$2^{11}-1$
	$\lambda_2 = 1550.12$			
	$\lambda_3 = 1549.72$			
SUT_4	$\lambda_1 = 1556.1$	2.5	DML	$2^{31}-1$
	$\lambda_2 = 1542.2$	25	MZM	$2^{17}-1$
	$\lambda_3 = 1541.6$	25	MZM	$2^{17}-1$
	$\lambda_4 = 1540.94$	2.5	MZM	$2^{31}-1$
SUT_5	$\lambda_1 = 1550.52$	10	MZM	$2^{15}-1$
	$\lambda_2 = 1550.12$			
SUT_6	$\lambda_1 = 1550.92$	10	MZM	$2^{15}-1$
	$\lambda_2 = 1550.12$			

The system exhibits a dynamic range of ~18 dB. The obtained result also confirms the versatility of the system in analyzing various modulation formats and specifications, including different bit rates. For additional examples demonstrating the SUT spanning nearly the entire C-band with various bit rate combinations, readers are referred to Fig. A2 in the Appendix. For the examples of the SUT with WDM channels at consistent bit rates and modulation formats, captured using a different sampling pulse period ($T_R = 69.565\ \mathrm{ns}$), consult Fig. A3.

Fig. 4.3 illustrates the capability of the RTOM system to capture intensity changes in the different DWDM channels with an accuracy in the dBm range. In this case, we process SUT_2 composed of four data streams located at central wavelengths of $\lambda_1 = 1556.1\ \mathrm{nm}$, $\lambda_2 = 1541.73\ \mathrm{nm}$, $\lambda_3 = 1541.33\ \mathrm{nm}$, and $\lambda_4 = 1540.94\ \mathrm{nm}$. In terms of modulation formats, Ch_1 employs DML, while the other channels utilize MZM. The data streams for Ch_1 and Ch_4 have a length of $2^{31} - 1$ and operate at a bit rate of 25 Gb/s. Conversely, Ch_2 and Ch_3 are configured with a data stream length of $2^{13} - 1$, operating at a bit rate of 1 Gb/s. These specifications and their arrangement within the SUT are concisely detailed in Table 4.1. Time sampling parameters are period $T_R = 208.7\ \mathrm{ns}$ and time width $\Delta t_p = 100\ \mathrm{ps}$.

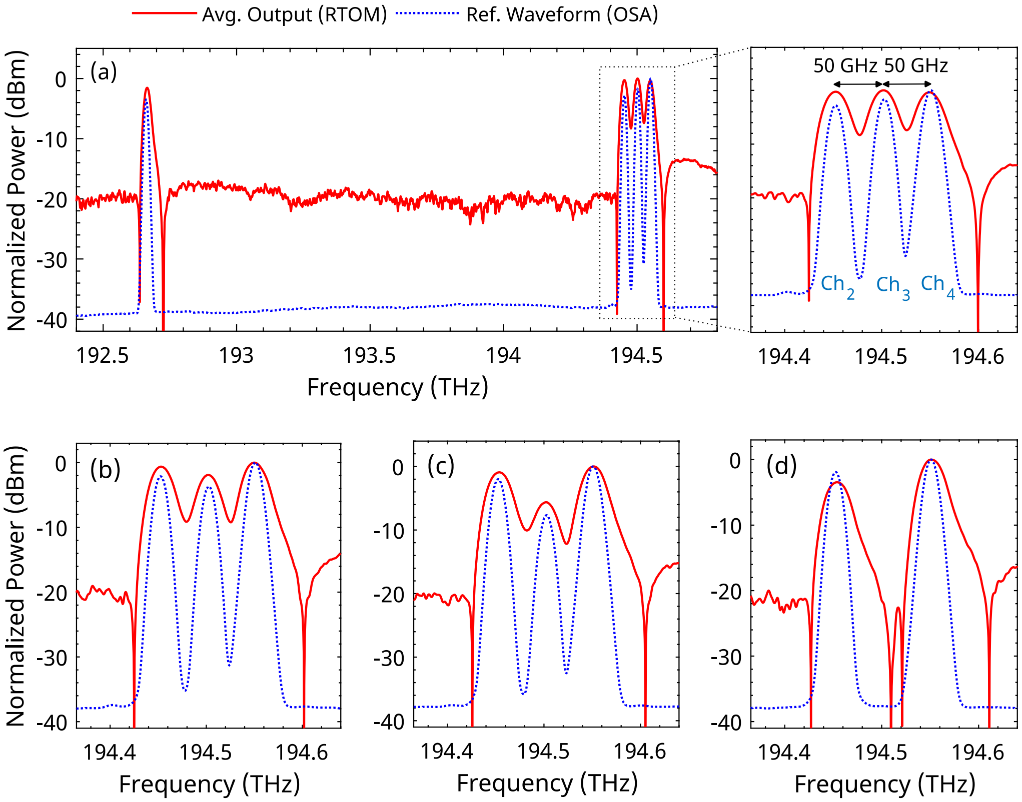

Fig. 4.3 System performance in case of tracking intensity variations in Ch₃. (a) No change, (b) 2 dB attenuation, (c) 6 dB attenuation, (d) Turning off.

Fig. 4.3(a) shows the measured output for SUT_2 compared to its reference spectral waveform (OSA measurement). For better visualization, only a close-up view of Ch_2-Ch_4 is displayed in Fig. 4.3(b-d). Subsequently, in Fig. 4.3(b), the power of Ch_3 is reduced by 2 dB, followed by a 6 dB reduction in Fig. 4.3(c), and finally turning it off in Fig. 4.3(d). As expected, the measured spectral traces, obtained by averaging 239 consecutive samples, accurately follow the reference waveform measured with the OSA. The obtained result clearly indicates that the system is able to track wavelength channels with the required high resolution, such that to clearly resolve the DWDM channels separation of 50 GHz, as denoted by the black arrow in the Fig. 4.3(a) zoom-in plot. The strong asymmetry in the temporal waveforms captured by the RTOM for each channel is mainly attributed to the irregular temporal response of the bandwidth-limited detection system.

To determine the frequency resolution of the RTOM system, we adjusted the resolution bandwidth of the OSA in Fig. 4.3(a) through post-processing. This adjustment was made to ascertain the point at which the waveform produced by the OSA aligns with that obtained from the RTOM system, as illustrated in Fig. 4.4. Consequently, through this comparison, we were able to establish that the RTOM system achieves a frequency resolution of ~0.22 nm, which is equivalent to around 28 GHz.

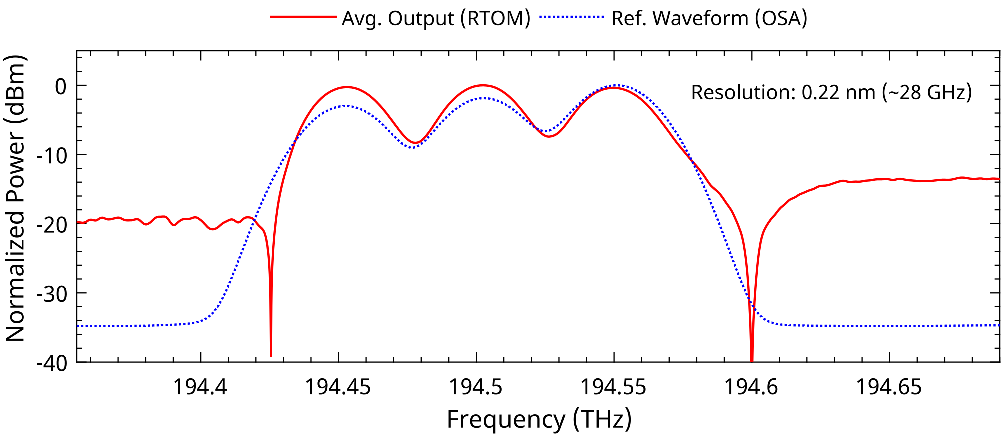

Fig. 4.4 RTOM system frequency resolution.

To achieve a finer frequency resolution, such as approaching the 0.1 nm precision offered by the OSA, a higher amount of dispersion can be used, as expected from Eq. (2-12). To demonstrate this effect, we considered SUT_3 composed of 3 channels located at central wavelengths of $\lambda_1 = 1550.52\ \mathrm{nm}$, $\lambda_2 = 1550.12\ \mathrm{nm}$, and $\lambda_3 = 1549.72\ \mathrm{nm}$ with 50 GHz channel spacing. The data streams in SUT_3, operating at a bit rate of 1 Gb/s, were encoded using a PRBS length of $2^{11} - 1$

and modulation type of MZM. In this measurement, a 20-km SMF-28 was used to disperse the SUT_3. Two dispersion compensating modules were concatenated to accumulate a total dispersion of $\ddot{\phi} = -688.6\ \mathrm{ps/nm}$. Fig. 4.5 illustrates the spectral traces for different dispersion amounts measured using the RTOM system, obtained from averaging 718 consecutive samples compared with the reference waveform obtained from a spectral measurement using a conventional OSA with 0.1 nm (~12.5 GHz) resolution bandwidth. It is observed that increasing the amount of dispersion enhances the frequency resolution, resulting in the output waveform that follows the reference waveform with greater detail. However, this modification would necessarily translate into a reduction in the measurement update rate of the RTOM. This stems from the fact that a higher dispersion amount extends the time-mapped spectrum duration Δt_{out}, necessitating a longer sampling period T_R. Since the measurement update rate of the RTOM system is inversely related to T_R, this adjustment implies a slower update rate. Considering the entire C-band, supporting 88 channels with 50 GHz spacing, dispersion amounts of $\ddot{\phi} = -688.6\ \mathrm{ps/nm}$ and $\ddot{\phi} = -1328\ \mathrm{ps/nm}$ result in output time-mapped spectra with temporal durations of $\Delta \mathrm{t_{out}} \approx 24.26\ \mathrm{ns}$ and $\Delta t_{out} \approx 46.79\ \mathrm{ns}$, respectively. For additional examples of the SUT with a 50 GHz channel spacing, and considering different bit rates and sampling pulse periods, readers are directed to Fig. A4 in the Appendix.

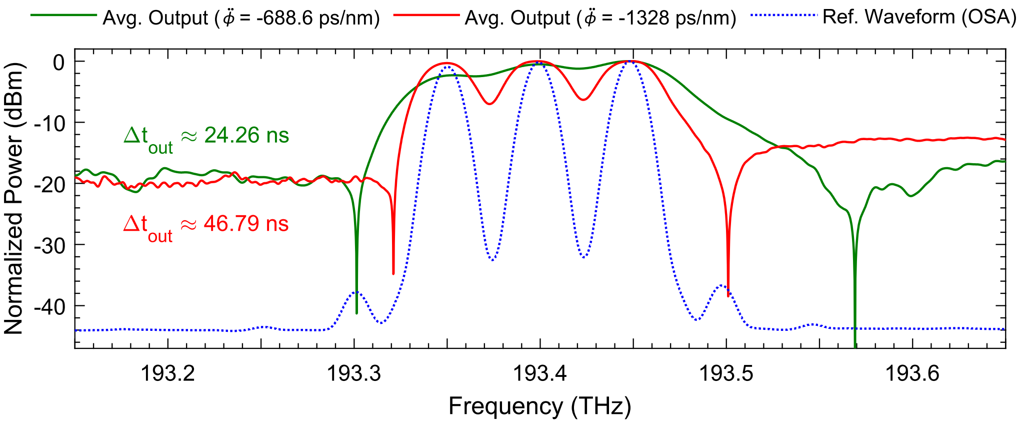

Fig. 4.5 Dispersion effect on the RTOM system's frequency resolution. The DWDM channels have a spacing of 50 GHz, operating at a bit rate of 1 Gb/s with MZM modulation. The time sampling is performed using the following parameters: $\Delta t_p = 100\ \mathrm{ps}$ and $T_R = 208.7\ \mathrm{ns}$.

As observed from Fig. 4.5, under a dispersion amount of $\ddot{\phi} = -688.6\ \mathrm{ps/nm}$, DWDM channels are not distinctly separated. In this case, by expanding the channel spacing from 50 GHz to 100 GHz, while maintaining the dispersion value at $\ddot{\phi} = -688.6\ \mathrm{ps/nm}$, the channels become more distinguishable. This characteristic is demonstrated in Fig. 4.6, showing the RTOM spectral trace derived from averaging 239 consecutive samples. The SUT_4 analyzed here is a 4-channel signal with central wavelengths located at $\lambda_1 = 1556.1\ \mathrm{nm}$, $\lambda_2 = 1542.4\ \mathrm{nm}$, $\lambda_3 = 1541.6\ \mathrm{nm}$, and $\lambda_4 = 1540.94\ \mathrm{nm}$. Ch_1 and Ch_4 operate at a bit rate of 2.5 Gb/s, encoded using a PRBS length of $2^{31} - 1$, while Ch_2 and Ch_3 operate at 25 Gb/s, encoded using a PRBS length of $2^{17} - 1$. The Ch_1 employs DML for modulation, and the remaining channels use MZM. The RTOM system's sampling period is $T_R = 208.7\ \mathrm{ns}$. For better visualization, a zoomed-in view of Ch$_2$ to Ch$_4$ is also displayed here. Comparing Fig. 4.6 with Fig. 4.5 clearly indicate how increasing channel spacing enhances the distinctness of the channels at the same dispersion level.

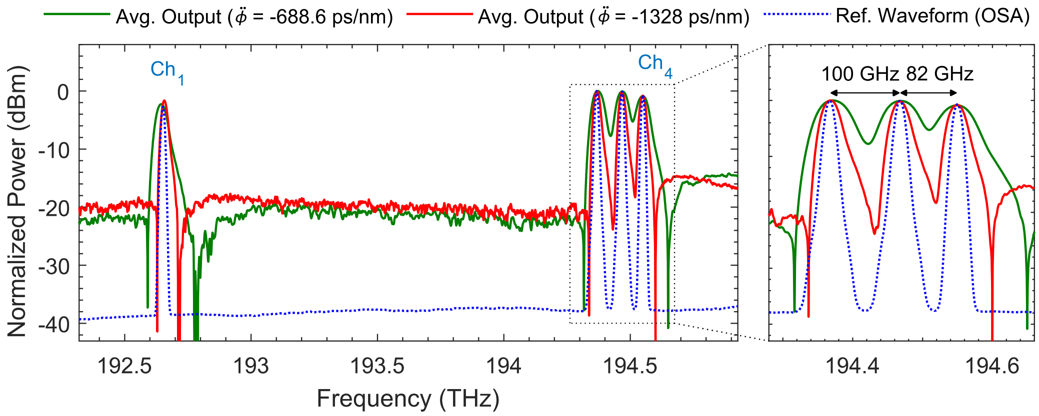

Fig. 4.6 Enhanced distinguishability of DWDM channels with increasing channel spacing at different dispersion amounts. The temporal sampling is conducted at $\boldsymbol{T_R = 208.7\ \mathrm{ns}}$ with sampling pulse width of $\boldsymbol{\Delta t_p = 100\ \mathrm{ps}}$.

Increasing the channel spacing to 100 GHz allows the RTOM system to use a wider sampling pulse width, such as $\Delta \mathrm{t_p} = 250\ \mathrm{ps}$, without compromising its performance. This is demonstrated in Fig. 4.7 by analyzing SUT_4. Despite the increased pulse width, the system's effectiveness remains intact with a dispersion value of $\ddot{\phi} = -1328\ \mathrm{ps/nm}$. However, dispersion amount of $\ddot{\phi} = -688.6\ \mathrm{ps/nm}$ is inadequate for such a wide sampling pulse width. As discussed in chapter 2, section 2.2., RTOM system can effectively operate under a relaxed Fraunhofer regime, i.e. $|\ddot{\phi}| \geq \Delta \mathrm{t_p^2}/2\pi$ (Eq. (2.11)). This highlights the system's flexibility and capacity for fine-tuning and adaptation under specific conditions, underscoring its potential for tailored operational optimization.

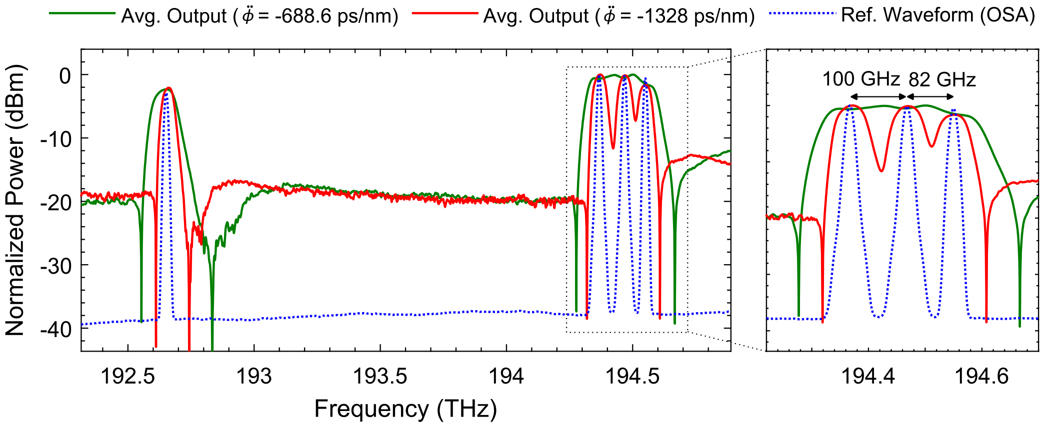

Fig. 4.7 RTOM system's performance with expanded sampling pulse width of $\Delta t_p = 250\ \mathrm{ps}$ and different dispersion values.

Finally, we demonstrate the unique capability of the RTOM system in real-time tracking of a dynamic input data signal that undergoes rapid changes in a microsecond scale. To this end, the input SUT is additionally modulated with a suitably designed square-like intensity variation function, in which changes are introduced every 14 analysis periods of the RTOM system, each with a duration of $T_R = 69.565\ \mathrm{ns}$. These changes involve adjusting the power levels of the SUT, including turning all channels on/off. The SUT_5 analyzed in Fig. 4.8 is composed of two data channels located at $\lambda_1 = 1550.52\ \mathrm{nm}$ and $\lambda_2 = 1550.12\ \mathrm{nm}$, corresponding to a 50 GHz channel spacing. The data streams are NRZ-OOK signals at a bit rate of 10 Gb/s, encoded using a PRBS of $2^{15} - 1$ and MZM modulation. Fig. 4.8(a) presents the measured spectrum evolution. The result obtained from a conventional OSA measurement is shown in Fig. 4.8(b), revealing the OSA limitation in terms of speed for tracking changes. The measured output temporal trace in Fig. 4.8(a) confirms the unprecedented measurement speed of the RTOM system enabling to accurately track spectral changes in the SUT on a microsecond scale. The result is obtained by averaging every 14 consecutive analysis periods, i.e. $69.565\ \mathrm{ns} \times 14$. The inverse of this duration corresponds to the system's measurement update rate, which is 1 MHz. A typical OSA requires ~200 ms to measure the C-band with 0.1 nm resolution bandwidth, representing a duration roughly 10^4 times longer than all the consecutive measurements conducted in Fig. 4.8(a).

System performance and speed considering a 100-GHz channel spacing is also displayed in Fig. 4.9, represents the result for analyzing SUT_6, composed of two data channels located at $\lambda_1 = 1550.92\ \mathrm{nm}$ and $\lambda_2 = 1550.12\ \mathrm{nm}$. The data streams are the same as SUT_5. The measurement traces depicted in Fig. 4.8(a) and Fig. 4.9(a) were captured using a 10-GHZ APD. Due to the relatively poor sensitivity of the APD used for this measurement, the sampled SUT needed to undergo additional amplification via an EDFA before passing through the DCF module. For more examples of the system performance considering a dynamic SUT, please consult Fig. A5 and Fig. A6 in the Appendix.

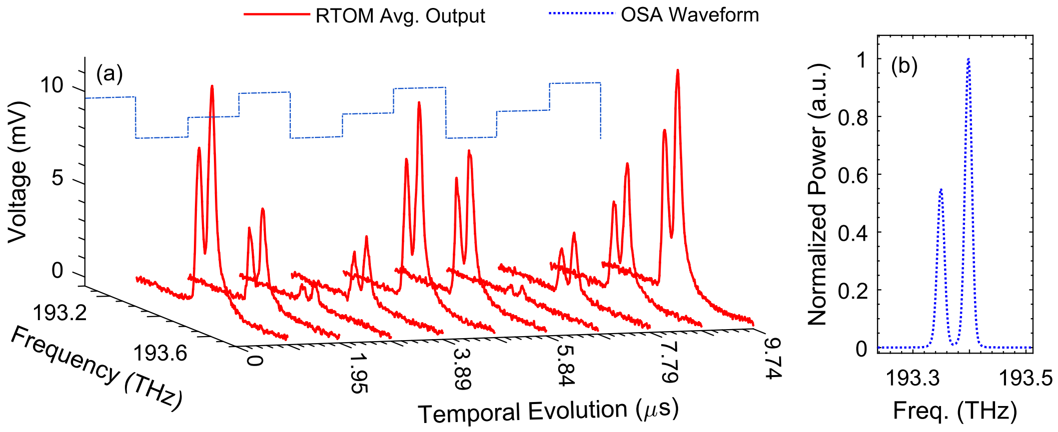

Fig. 4.8 (a) RTOM output waveform obtained for the dynamic SUT_5, changing every 14 samples. (b) Waveform obtained from a conventional OSA for all samples of SUT_5. Channel spacing is 50 GHz, and temporal sampling is performed with a period of $T_R = 69.565$ ns.

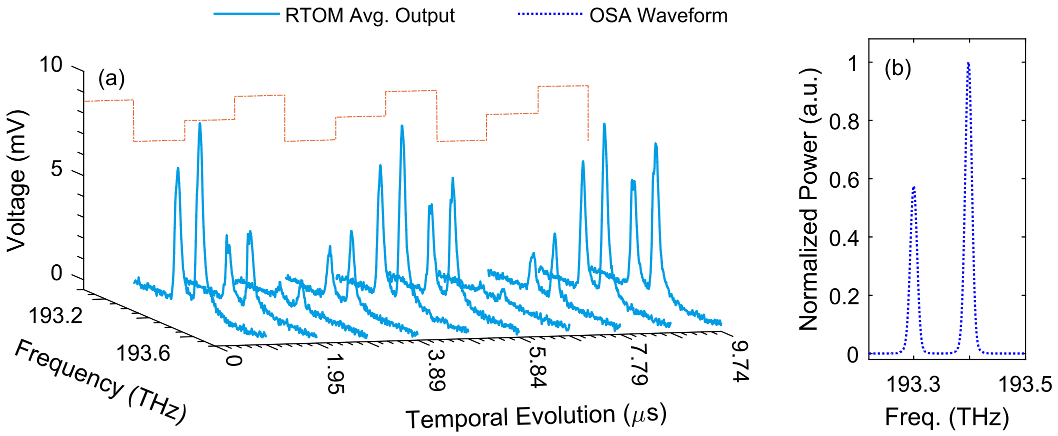

Fig. 4.9 (a) RTOM output waveform obtained for the dynamic SUT_6, changing every 14 samples. (b) Waveform obtained from a conventional OSA for all samples of SUT_6. Channel spacing is 100 GHz, and temporal sampling is conducted with a period of $T_R = 69.565$ ns.

5 CONCLUSION AND FUTURE WORK

5.1 Conclusion

Future optical communication systems are required to accommodate high data rates and dynamically adapt to changing network conditions, in order to fulfill the growing demand for services that require extensive bandwidth [66]. Providing high quality of service (QoS) in optical networks, particularly as they operate at high data rates and capacities, is the driving force behind the growing demand for optical layer monitoring [11]. The efficient operation and effective management of such high capacity optical networks, deploying a WDM approach, rely on performance monitoring techniques, among which optical spectrum monitoring has attracted attention. Identifying WDM channels and their relative intensity is indeed a fundamental objective of optical spectrum monitoring. The necessity for sub-millisecond scale monitoring emerges from several factors tied to the requirements of modern, high-speed, stable, and robust networks. Fluctuations in these networks can occur due to a variety of internal and external factors. Detecting these fluctuations in real time enables immediate corrective actions, thereby ensuring network stability and reliability. Rapid monitoring facilitates the early detection of faults, allowing for the swift activation of backup systems to prevent issue escalation, minimize service disruptions, and maintain high QoS. This is particularly crucial for services requiring ultra-reliable connections, such as autonomous vehicles. In evolving networks, real-time monitoring also supports dynamic resource allocation, adjusting to current network conditions. As networks grow and become more complex, real-time monitoring remains vital to ensure system integrity and optimal optical performance. Therefore, the development of cost-effective and energy-efficient signal analysis and processing tools, capable of real-time operation with extremely low latencies, is of paramount importance.

In this thesis, we focused on real-time monitoring of the evolving optical spectrum of DWDM signals within telecommunication links, and introduced a novel and efficient scheme for this purpose. The proposed system, referred to as RTOM, which utilizes temporal sampling in conjunction with D-FTM, provides a straightforward method to discern the presence and relative intensity of multiple DWDM channels across the entire optical telecom C-band (1530-1565 nm). The RTOM system demonstrates robust performance across a wide range of conditions, including different modulation formats (MZM and DML), bit rates (ranging from 1 Gb/s to 25 Gb/s), and DWDM channel spacings (50 GHz and 100 GHz). In addition, it offers the needed resolution to discern channels separated by a few tens of GHz, accuracy, and unprecedented fast measurement update rates in the MHz range, which is orders of magnitude better than OSAs. This versatility underscores the system's practical applicability in a range of optical network environments. Thus, RTOM system’s key features include: (1) rapid response time; (2) simplicity of implementation using readily available linear optics components, particularly an Electro-Optic (EO) modulator and a piece of fiber; (3) wide monitoring range; (4) fine resolution; (5) adaptability to various modulation formats and bit rates without any need to modification; and (6) potential integration onto photonic chips. While this research primarily demonstrates results for non-return-to-zero on-off keying (NRZ-OOK) signals in the C-band, the system's methodology could be applicable to other broad frequency bands (e.g., O, S, and L bands) and signals with diverse coding formats. The performance of the proposed RTOM scheme versus other alternative technologies is summarized in Table 5.1.

Table 5.1 Performance of RTOM versus different technologies.

OPM Techniques						
Specifications	WISTOM [3]	PASTA [32]	Optical Labels [34, 37]	Pilot Tone [35]	ML [33, 38]	RTOM
Wavelength range	C-band	5 nm	-	-	-	C-band
Frame rate	>10 kHz	100 MHz	-	kHz	kHz	>1 MHz
Resolution	-	0.03 nm	-	-	-	~0.22 nm
Dynamic range	-	-	-	-	-	~18 dB
Polarization	-	sensitive	-	-	-	sensitive
Main Limitation	-	-Highly energy and cost inefficient (based on nonlinear fiber optics)	-SRS and CD effect -Circuit complexity -Limitation in adjusting the transmission rate of label signals	-Requires transmitter modification -Requires additional consideration to isolate CD and PMD effects	-Extensive pre-processing and dataset training	-Polarization sensitivity[1] -Frequency resolution and dispersion trade-off

Previous OPM Techniques						
	Photodiode Array OSA [24]	Fabry–Pérot Interferometer OSA [25]	AWG-based OSA [26]	MEMS-based OSA [27, 28]	LC FOSA [29]	Tilted Fiber Grating-based OSA [30,31]
Main Limitation	-Slow update rates (typically in the kHz range and lower) -Generally costly and are often based on bulky as well as inefficient designs -Challenges for in-line monitoring tasks -Requirement of mechanically moving parts in the grating -Complicated fabrication processes of cavities -Requirement of expensive devices or complex data processing					

[1] It can be solved by solutions provided in next section.

As a rule-of-thumb, the following specifications are required for the design of the RTOM system:

- The time-width duration of the sampling pulses should be long enough to capture adequate data signal information, typically spanning a few bit periods. This ensures that enough data is collected for accurate signal representation while also satisfying the far-field condition in conjunction with the chosen group velocity dispersion (GVD).
- The required dispersion amount is then calculated using Eq. (2.11).
- Considering the frequency-to-time mapping law (Eq. (2.9)), achieving a target frequency resolution $\delta\omega_r$ requires the RTOM detection system to capture the output temporal waveforms with a resolution of at least $\delta t_r \approx |\ddot{\phi}| \times \delta\omega_r$. Exceeding this time resolution significantly may impair noise performance. The frequency resolution $\delta\omega_r$ must be narrow enough to discern two adjacent WDM channels in the analyzed system. Thus, the photodetector bandwidth should be on the order of $1/\delta t_r$.
- The value of the temporal sampling period must be larger than the temporal duration of the time-mapped spectrum of each sampled SUT portion to avoid overlapping among consecutively mapped sections, i.e., $T_R > \Delta t_{out}$, according to the Eq. (2.14).
- The required extinction ratio (ER) for the MZM used for temporal sampling varies depending on the requirements of the specific application of the RTOM system. It has been observed that achieving a 40 dB extinction ratio is realistic in most practical scenarios.

In chapter 1, we have reviewed the importance and necessities of optical performance monitoring along with the limitations of the available monitoring techniques. Then, in chapter 2, we have provided a comprehensive overview of the fundamental concept and operational principles underlying the proposed system. The concept of D-FTM and its constraints for applying to continuous signals were described. Subsequently, the design and functionality of the proposed system along with the temporal sampling technique employed to overcome D-FTM's limitations were introduced. In chapter 3, we have demonstrated the theoretical and numerical simulation results and conducted a comprehensive analysis of the impact of different parameters which helped us to choose the optimal value for design parameters. Then we have evaluated the proposed system’s performance and its potential capabilities. In chapter 4, we have experimentally demonstrated the performance of the proposed system to monitor DWDM signals with different modulation formats and bit rates with channel spacing of 50 GHz and 100 GHz. A comprehensive analysis of the main results has also been presented in this chapter.

5.2 Future work

The research presented in this thesis, while revealing significant strides in monitoring next generation fiber-optic transmission systems, opens avenues for further enhancements and explorations. Key areas identified for future work are as follows.

5.2.1 Polarization management

A major challenge with the proposed system experiments is managing the polarization diversity of the input signals originating from various sources. To address this, we propose multiple solutions: firstly, introducing a secondary path for the alternate polarization; secondly, constructing a passive circuit, potentially in Silicon Photonics (SiP), to split, rotate, and combine the polarizations; thirdly, employing high-speed polarization control devices at the input of the RTOM system to dynamically adjust and rotate through different polarization states; and finally, using polarization independent modulation mechanism for time sampling. The schematic of the RTOM system equipped with a secondary path for the alternate polarization is illustrated in Fig. 5.1.

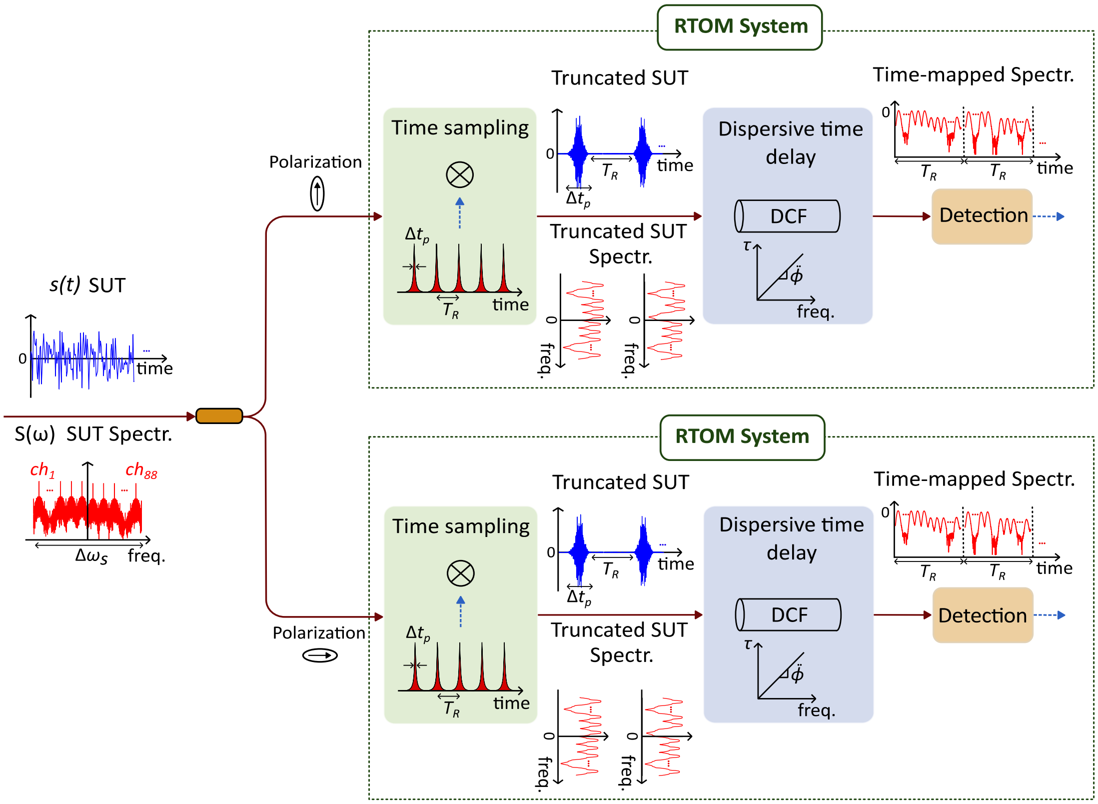

Fig. 5.1 RTOM system schematic equipped with a secondary path for the alternate polarization.

5.2.2 Enhancing frequency resolution

Achieving a finer frequency resolution, comparable to the 0.1 nm precision of an OSA, necessitates the use of higher dispersion. However, this approach leads to a compromise in the measurement update rate of the RTOM system. Balancing precision and speed, especially in applications where both are crucial, will require careful consideration and optimization.

5.2.3 Dynamic range

The dynamic range is a vital aspect in the assessment of optical performance monitoring systems. It is integral for ensuring accurate signal detection, upholding high QoS, and providing network adaptability, particularly with the advancement of optical communication technologies. A broad dynamic range is essential for accurately detecting both weak and strong optical signals, crucial in networks with varying signal strengths due to factors like attenuation, dispersion, and differing optical path lengths. As optical networks evolve and incorporate new channels or adjust transmission power, a monitoring system with a high dynamic range can adapt without performance loss, making it versatile for diverse network setups. With the increasing use of advanced modulation formats exhibiting a wide range of power levels, a high dynamic range is necessary for precise performance assessment. Handling the signal-to-noise ratio efficiently is critical for maintaining transmitted data fidelity and integrity. A broad dynamic range ensures effective monitoring even in noisy environments. In our proposed system, the detection system's noise significantly impacts the dynamic range. Therefore, a deeper investigation into enhancing the dynamic range is warranted.

5.2.4 On-chip integration

On-chip integration is the ultimate step of the development of any signal processing scheme, as it enables the implementation of these concepts into practical devices, particularly in scenarios where the use of bulky components is not feasible. Hence, the proposed scheme would need to be packaged into a small device for widespread application. The dispersive medium length would be an extremely challenging target of the on-chip implementation. Current advanced approaches for achieving second-order dispersion in integrated platforms rely on linearly chirped waveguide Bragg gratings (LCWBGs). In these systems, the grating period or waveguide width is linearly varied along the length of the device, creating a linear group delay profile across the targeted spectral region [67]. However, LCWBGs encounter inherent limitations due to the spectral phase accumulation integral to their design, restricting the maximum GVD that can be compensated for over a designated operational bandwidth. The constraint arises because a greater phase excursion necessitates a proportionally longer device, subsequently enlarging the overall footprint of the device. As alternatives, technologies such as Arrayed Waveguide Gratings [68], Lattice Filters based on Multi-Mode Interference (MMI) Couplers [69], and Single [70] or Multi-Stage Microring Resonators [71] have been explored for residual dispersion compensation in WDM channels [72]. However, these methods commonly face an intrinsic trade-off between usable bandwidth and the extent of GVD compensation achievable. In contrast, devices exploiting the dispersive properties of a coupled-defect waveguide in a photonic crystal can offer substantial GVD compensation in an ultra-compact format [73]. Yet, these devices are not without their challenges, as they are particularly susceptible to high scattering and coupling losses, presenting significant hurdles for practical implementation. One possible solution for compact on-chip dispersive lines would be employing discrete spectral phase filters based on integrated waveguide Bragg gratings (WBGs), in which the target spectral response is implemented in a discretized fashion and bounded in between 0 and 2π [72]. This avoids the spectral phase (or delay) accumulation of conventional dispersive lines, leading to a significant length reduction. The overall bandwidth of this discrete phase filter device can be increased by extending the range of operation to multiple WDM channels by using a phase-only periodic sampling function in the grating equation of the single-channel WBG [72, 74-78]. Using this technique, the implementation complexity in terms of device length and the required spatial resolution or the minimum feature size of the device remains unchanged. Another proposed approach for further compactness involves implementing a multichannel version of a linearly chirped Bragg grating in a waveguide device. After photodetection, the only component needed is an analog-to-digital converter (ADC) with a bandwidth of the order of or larger than that of the photodetector.

REFERENCES

[1] G. P. Agrawal, *Fiber-optic communication systems*: John Wiley & Sons, 2012.

[2] T. Wu, F. Tian, Y. Wu, X. Yue, Y. Gu, Y. Cui, Q. Zhang, and R. Ullah, "Performance Analysis and Power Tilt Mitigation of Ultra-Wideband WDM Transmission Systems." *Photonics*, Vol. 10, No. 5, p. 530, 2023.

[3] “Proximion AB, white paper “Optical Layer Monitoring” (2013).

Available: https://www.proximion.com/hubfs/bu-pr/white-paper/optical-layer-monitoring/100499-D-LDO-WISTOM-White-Paper-Optical-Layer-Monitoring-web.pdf.”

[4] P. J. Winzer, and R.-J. Essiambre, "Advanced optical modulation formats," *Optical Fiber Telecommunications VB*, pp. 23-93: Elsevier, 2008.

[5] X. Zhou, and C. Xie, *Enabling technologies for high spectral-efficiency coherent optical communication networks*: John Wiley & Sons, 2016.

[6] C. C. Chan, *Optical performance monitoring: advanced techniques for next-generation photonic networks*: Academic Press, 2010.

[7] D. Rico, and P. Merino, “A survey of end-to-end solutions for reliable low-latency communications in 5g networks,” *IEEE Access,* vol. 8, pp. 192808-192834, 2020.

[8] Z. Dong, F. N. Khan, Q. Sui, K. Zhong, C. Lu, and A. P. T. Lau, “Optical Performance Monitoring: A Review of Current and Future Technologies,” *Journal of Lightwave Technology,* vol. 34, no. 2, pp. 525-543, 2016.

[9] S. N. Khonina, N. L. Kazanskiy, M. A. Butt, and S. V. Karpeev, “Optical multiplexing techniques and their marriage for on-chip and optical fiber communication: a review,” *Opto-Electronic Advances,* vol. 5, no. 8, pp. 210127-1-210127-25, 2022.

[10] M. Jinno, H. Takara, B. Kozicki, Y. Tsukishima, Y. Sone, and S. Matsuoka, “Spectrum-efficient and scalable elastic optical path network: architecture, benefits, and enabling technologies,” *IEEE communications magazine,* vol. 47, no. 11, pp. 66-73, 2009.

[11] M. S. Islam, and S. P. Majumder, “Optical and higher layer performance monitoring in photonic networks: Progress and challenges,” *2009 11th International Conference on Advanced Communication Technology,* vol. 03, pp. 1591-1596, 2009.

[12] F. N. Khan, T. S. R. Shen, Y. Zhou, A. P. T. Lau, and C. Lu, “Optical performance monitoring using artificial neural networks trained with empirical moments of asynchronously sampled signal amplitudes,” *IEEE Photonics Technology Letters,* vol. 24, no. 12, pp. 982-984, 2012.

[13] D. C. Kilper, R. Bach, D. J. Blumenthal, D. Einstein, T. Landolsi, L. Ostar, M. Preiss, and A. E. Willner, “Optical Performance Monitoring,” *Journal of Lightwave Technology,* vol. 22, no. 1, pp. 294-304, 2004.

[14] A. E. Willner, “The optical network of the future,” *Optics and Photonics News,* vol. 17, no. 3, pp. 30-35, 2006.

[15] Y. G. Huang, J. P. Heritage, and B. Mukherjee, “Connection provisioning with transmission impairment consideration in optical WDM networks with high-speed channels,” *Journal of lightwave technology,* vol. 23, no. 3, pp. 982, 2005.

[16] E. Bouillet, G. Ellinas, J.-F. Labourdette, and R. Ramamurthy, *Path routing in mesh optical networks*: John Wiley & Sons, 2007.

[17] X. Liu, Y.-H. Kao, S. Chandrasekhar, I. Kang, S. Cabot, and L. Buhl, “OSNR monitoring method for OOK and DPSK based on optical delay interferometer,” *IEEE Photonics Technology Letters,* vol. 19, no. 15, pp. 1172-1174, 2007.

[18] A. E. Willner, Z. Pan, and C. Yu, "Optical performance monitoring," *Optical fiber telecommunications VB*, pp. 233-292: Elsevier, 2008.

[19] B. Mukherjee, I. Tomkos, M. Tornatore, P. Winzer, and Y. Zhao, “Springer handbook of optical networks,” 2020.

[20] D. van Veen, and V. Houtsma, "Digital signal processing in optical access systems." p. SpT1E. 1., 2019.

[21] N. Iiyama, J.-i. Kani, K.-i. Suzuki, and A. Ootaka, "Advanced DSP for optical access networks: Challenges and opportunities." p. M3J. 3., 2015.

[22] J. Zou, S. Adrian Sasu, M. Lawin, A. Dochhan, J.-P. Elbers, and M. Eiselt, “Advanced optical access technologies for next-generation (5G) mobile networks [Invited],” *Journal of Optical Communications and Networking,* vol. 12, no. 10, 2020.

[23] X. Liu, and F. Effenberger, “Emerging Optical Access Network Technologies for 5G Wireless,” *Journal of Optical Communications and Networking,* vol. 8, no. 12, 2016.

[24] K. Otsuka, T. Maki, Y. Sampei, Y. Tachikawa, N. Fukushima, and T. Chikama, "A high-performance optical spectrum monitor with high-speed measuring time for WDM optical networks." *In Integrated Optics and Optical Fibre Communications, 11th International Conference on, and 23rd European Conference on Optical Communications*, Vol. 2, pp. 147-150, 1997.

[25] J. Peerlings, A. Dehé, A. Vogt, M. Tilsch, C. Hebeler, F. Langenhan, P. Meissner, and H. L. Hartnagel, "GaAs/AlAs micromachined tunable Fabry-Perot filters for dense wavelength division multiplex systems." *In Integrated Optics and Optical Fibre Communications, 11th International Conference on, and 23rd European Conference on Optical Communications*, Vol. 3, pp. 1-5, 1997.

[26] K. Takada, H. Yamada, and K. Okamoto, “Optical spectrum analyzer using cascaded AWGs with different channel spacings,” *IEEE Photonics Technology Letters,* vol. 11, no. 7, pp. 863-864, 1999.

[27] K. Nakamura, T. Saitoh, and Y. Takahashi, "High-speed optical performance monitor for WDM network using MEMS scanning mirror." In 2003 *IEEE/LEOS International Conference on Optical MEMS*, pp. 97-98, 2003.

[28] T. Saitoh, K. Nakamura, Y. Takahashi, and K. Miyagi, “Optical spectrum analyzer utilizing MEMS scanning mirror,” *IEEE Photonics Technology Letters,* vol. 18, no. 6, pp. 767-769, 2006.

[29] Y. Q. Lu, C. Wong, and S. T. Wu, “A Liquid Crystal-Based Fourier Optical Spectrum Analyzer,” *IEEE Photonics Technology Letters,* vol. 16, no. 3, pp. 861-863, 2004.

[30] Y. Tissot, H. G. Limberger, and R. P. Salathe, “Ultrawide Bandwidth Wavelength Monitor Based on a Pair of Tilted Fiber Bragg Gratings,” *IEEE Photonics Technology Letters,* vol. 19, no. 21, pp. 1702-1704, 2007.

[31] K. Zhou, X. Chen, Z. Yan, A. Adebayo, and L. Zhang, "Optical spectrum analyzer using a 45 tilted fiber grating." *Bragg Gratings, Photosensitivity, and Poling in Glass Waveguides*, p. BW2E. 7, 2012.

[32] C. Zhang, J. Xu, P. C. Chui, and K. K. Wong, “Parametric spectro-temporal analyzer (PASTA) for real-time optical spectrum observation,” *Scientific reports,* vol. 3, pp. 2064, 2013.

[33] D. Wang, M. Zhang, Z. Zhang, J. Li, H. Gao, F. Zhang, and X. Chen, “Machine Learning-Based Multifunctional Optical Spectrum Analysis Technique,” *IEEE Access,* vol. 7, pp. 19726-19737, 2019.

[34] T. Yang, K. Li, Z. Liu, X. Wang, S. Shi, L. Wang, and X. Chen, “Optical Labels Enabled Optical Performance Monitoring in WDM Systems,” *Photonics,* vol. 9, no. 9, 2022.

[35] Z. Jiang, X. Tang, S. Wang, G. Gao, D. Jin, J. Wang, and M. Si, “Progresses of Pilot Tone Based Optical Performance Monitoring in Coherent Systems,” *Journal of Lightwave Technology,* vol. 40, no. 10, pp. 3128-3136, 2022.

[36] K. J. Park, H. C. Ji, and Y. C. Chung, “Optical channel monitoring technique using phase-modulated pilot tones,” *IEEE Photonics Technology Letters,* vol. 17, no. 11, pp. 2481-2483, 2005.

[37] C. Yang, X. Li, M. Luo, Z. He, H. Li, C. Li, and S. Yu, "Optical labelling and performance monitoring in coherent optical wavelength division multiplexing networks." *Optical Fiber Communication Conference*, p. Th2A. 50, 2020.

[38] W. S. Saif, A. M. Ragheb, T. A. Alshawi, and S. A. Alshebeili, “Optical performance monitoring in mode division multiplexed optical networks,” *Journal of Lightwave Technology,* vol. 39, no. 2, pp. 491-504, 2020.

[39] D. Wang, Q. Sui, and Z. Li, “Toward Universal Optical Performance Monitoring for Intelligent Optical Fiber Communication Networks,” *IEEE Communications Magazine,* vol. 58, no. 9, pp. 54-59, 2020.

[40] T. Jannson, “Real-time Fourier transformation in dispersive optical fibers,” *Optics Letters,* vol. 8, no. 4, pp. 232-234, 1983/04/01, 1983.

[41] J. Azana, and M. A. Muriel, “Real-time optical spectrum analysis based on the time-space duality in chirped fiber gratings,” *IEEE Journal of Quantum Electronics,* vol. 36, no. 5, pp. 517-526, 2000.

[42] T. Godin, L. Sader, A. Khodadad Kashi, P.-H. Hanzard, A. Hideur, D. J. Moss, R. Morandotti, G. Genty, J. M. Dudley, A. Pasquazi, M. Kues, and B. Wetzel, “Recent advances on time-stretch dispersive Fourier transform and its applications,” *Advances in Physics: X,* vol. 7, no. 1, 2022.

[43] C. Wang, “Dispersive Fourier Transformation for Versatile Microwave Photonics Applications,” *Photonics,* vol. 1, no. 4, pp. 586-612, 2014.

[44] L. Romero Cortés, D. Onori, H. Guillet de Chatellus, M. Burla, and J. Azaña, “Towards on-chip photonic-assisted radio-frequency spectral measurement and monitoring,” *Optica,* vol. 7, no. 5, 2020.

[45] M. H. Asghari, Y. Park, and J. Azaña, “Complex-field measurement of ultrafast dynamic optical waveforms based on real-time spectral interferometry,” *Optics Express,* vol. 18, no. 16, pp. 16526-16538, 2010.

[46] K. Goda, and B. Jalali, “Dispersive Fourier transformation for fast continuous single-shot measurements,” *Nature Photonics,* vol. 7, no. 2, pp. 102-112, 2013.

[47] H. G. de Chatellus, L. R. Cortés, and J. Azaña, “Optical real-time Fourier transformation with kilohertz resolutions,” *Optica,* vol. 3, no. 1, pp. 1-8, 2016.

[48] S. Dobner, and C. Fallnich, “Dispersive Fourier transformation femtosecond stimulated Raman scattering,” *Applied Physics B,* vol. 122, no. 11, 2016.

[49] A. Tae-Jung, P. Yongwoo, and J. Azaña, “Ultrarapid Optical Frequency-Domain Reflectometry Based Upon Dispersion-Induced Time Stretching: Principle and Applications,” *IEEE Journal of Selected Topics in Quantum Electronics,* vol. 18, no. 1, pp. 148-165, 2012.

[50] C. Wang, and J. Yao, “Ultrahigh-Resolution Photonic-Assisted Microwave Frequency Identification Based on Temporal Channelization,” *IEEE Transactions on Microwave Theory and Techniques,* vol. 61, no. 12, pp. 4275-4282, 2013.

[51] K. Krupa, K. Nithyanandan, U. Andral, P. Tchofo-Dinda, and P. Grelu, “Real-Time Observation of Internal Motion within Ultrafast Dissipative Optical Soliton Molecules,” *Phys Rev Lett,* vol. 118, no. 24, pp. 243901, Jun 16, 2017.

[52] Y. Liu, W. Ni, L. Yang, S. Huang, H. Liu, Y. Sun, R. Xia, Y. Yao, L. Yan, Y. Luo, Z. Xu, G. Xu, Q. Sun, X. Tang, and P. P. Shum, “Real-time spectral interferometry enables ultrafast acoustic detection,” *Applied Physics Letters,* vol. 123, no. 21, 2023.

[53] R. Salem, M. A. Foster, and A. L. Gaeta, “Application of space–time duality to ultrahigh-speed optical signal processing,” *Advances in Optics and Photonics,* vol. 5, no. 3, 2013.

[54] T. T. Wong, A. K. Lau, K. K. Wong, and K. K. Tsia, “Optical time-stretch confocal microscopy at 1 μm,” *Optics letters,* vol. 37, no. 16, pp. 3330-3332, 2012.

[55] R. E. Saperstein, N. Alić, D. Panasenko, R. Rokitski, and Y. Fainman, “Time-domain waveform processing by chromatic dispersion for temporal shaping of optical pulses,” *JOSA B,* vol. 22, no. 11, pp. 2427-2436, 2005.

[56] J. Hult, R. S. Watt, and C. F. Kaminski, “High bandwidth absorption spectroscopy with a dispersed supercontinuum source,” *Optics express,* vol. 15, no. 18, pp. 11385-11395, 2007.

[57] B. Wetzel, A. Stefani, L. Larger, P.-A. Lacourt, J.-M. Merolla, T. Sylvestre, A. Kudlinski, A. Mussot, G. Genty, and F. Dias, “Real-time full bandwidth measurement of spectral noise in supercontinuum generation,” *Scientific reports,* vol. 2, no. 1, pp. 882, 2012.

[58] J. Azaña, L. Chen, M. Muriel, and P. Smith, “Experimental demonstration of real-time Fourier transformation using linearly chirped fibre Bragg gratings,” *Electronics Letters,* vol. 35, no. 25, pp. 2223-2224, 1999.

[59] W. Liu, W. Li, and J. Yao, “Real-time interrogation of a linearly chirped fiber Bragg grating sensor for simultaneous measurement of strain and temperature,” *IEEE Photonics Technology Letters,* vol. 23, no. 18, pp. 1340-1342, 2011.

[60] R. Maram, D. Onori, J. Azaña, and L. R. Chen, “Discretely programmable microwave photonic filter based on temporal talbot effects,” *Optics express,* vol. 27, no. 10, pp. 14381-14391, 2019.

[61] H. Chi, and J. Yao, “All-Fiber Chirped Microwave Pulses Generation Based on Spectral Shaping and Wavelength-to-Time Conversion,” *IEEE Transactions on Microwave Theory and Techniques,* vol. 55, no. 9, pp. 1958-1963, 2007.

[62] H. Xia, C. Wang, S. Blais, and J. Yao, “Ultrafast and Precise Interrogation of Fiber Bragg Grating Sensor Based on Wavelength-to-Time Mapping Incorporating Higher Order Dispersion,” *Journal of Lightwave Technology,* vol. 28, no. 3, pp. 254-261, 2010.

[63] J. Chan, G. Hendry, K. Bergman, and L. P. Carloni, “Physical-Layer Modeling and System-Level Design of Chip-Scale Photonic Interconnection Networks,” *IEEE Transactions on Computer-Aided Design of Integrated Circuits and Systems,* vol. 30, no. 10, pp. 1507-1520, 2011.

[64] Dispersion Compensation Units.

Available: https://www.bccshop.fi/downloads/products/d/dc-ph-19/DC-PH.pdf.

[65] FRM5W232FY-InGaAs-APD/Preamp Receiver.

Available: https://datasheetspdf.com/pdf-file/657864/EudynaDevices/FRM5W232FY/1.

[66] J. S. Zou, S. A. Sasu, M. Lawin, A. Dochhan, J.-P. Elbers, and M. Eiselt, “Advanced optical access technologies for next-generation (5G) mobile networks,” *Journal of Optical Communications and Networking,* vol. 12, no. 10, pp. D86-D98, 2020.

[67] S. Kaushal, and J. Azana, “On-chip dispersive phase filters for optical processing of periodic signals,” *Opt Lett,* vol. 45, no. 16, pp. 4603-4606, Aug 15, 2020.

[68] D. M. Marom, C. R. Doerr, M. A. Cappuzzo, C. Evans Yifan, A. Wong-Foy, L. T. Gomez, and S. Chandrasekhar, “Compact colorless tunable dispersion compensator with 1000-ps/nm tuning range for 40-gb/s data rates,” *Journal of Lightwave Technology,* vol. 24, no. 1, pp. 237-241, 2006.

[69] A. Rahim, S. Schwarz, J. Bruns, K. Voigt, D. I. Kroushkov, M. T. Arnous, C. G. Schaffer, and K. Petermann, “Finite Impulse Response Filter Using 4-Port MMI Couplers for Residual Dispersion Compensation,” *Journal of Lightwave Technology,* vol. 30, no. 7, pp. 990-996, 2012.

[70] K. Y. K. Ong, G. F. R. Chen, P. Xing, H. Gao, and D. T. H. Tan, “Dispersion compensation of high-speed data using an integrated silicon nitride ring resonator,” *Opt Express,* vol. 30, no. 9, pp. 13959-13967, Apr 25, 2022.

[71] C. K. Madsen, G. Lenz, A. J. Bruce, M. A. Capuzzo, L. T. Gomez, T. N. Nielsen, and I. Brener, “Multistage dispersion compensator using ring resonators,” *Optics Letters,* vol. 24, no. 22, pp. 1555-1557, 1999/11/15, 1999.

[72] S. Kaushal, A. Roberge, R. Kashyap, and J. Azana, “Ultra-compact silicon photonics highly dispersive elements for low-latency signal processing,” *Opt Express,* vol. 31, no. 3, pp. 3467-3478, Jan 30, 2023.

[73] K. Hosomi, and T. Katsuyama, “A dispersion compensator using coupled defects in a photonic crystal,” *IEEE Journal of Quantum Electronics,* vol. 38, no. 7, pp. 825-829, 2002.

[74] X. Wang, W. Shi, R. Vafaei, N. A. F. Jaeger, and L. Chrostowski, “Uniform and Sampled Bragg Gratings in SOI Strip Waveguides with Sidewall Corrugations,” *IEEE Photonics Technology Letters*, 2011.

[75] M. W. Puckett, F. Vallini, A. Grieco, and Y. Fainman, “Multichannel Bragg gratings in silicon waveguides with asymmetric sidewall modulation,” *Opt Lett,* vol. 40, no. 3, pp. 379-82, Feb 1, 2015.

[76] T.-H. Yen, C.-J. Wu, C.-J. Yu, and Y.-J. Hung, "Silicon photonics multi-channel Bragg reflectors based on narrowband cladding-modulated gratings." pp. 1-2.

[77] S. Paul, T. Saastamoinen, S. Honkanen, M. Roussey, and M. Kuittinen, “Multi-wavelength filtering with a waveguide integrated phase-modulated Bragg grating,” *Optics Letters,* vol. 42, no. 22, pp. 4635-4638, Nov 15, 2017.

[78] X.-F. Jia, L.-J. Wang, N. Zhuo, J.-C. Zhang, S.-Q. Zhai, J.-Q. Liu, S.-M. Liu, F.-Q. Liu, and Z. Wang, “Multi-wavelength sampled Bragg grating quantum cascade laser arrays,” *Photonics Research,* vol. 6, no. 7, 2018.

Appendix

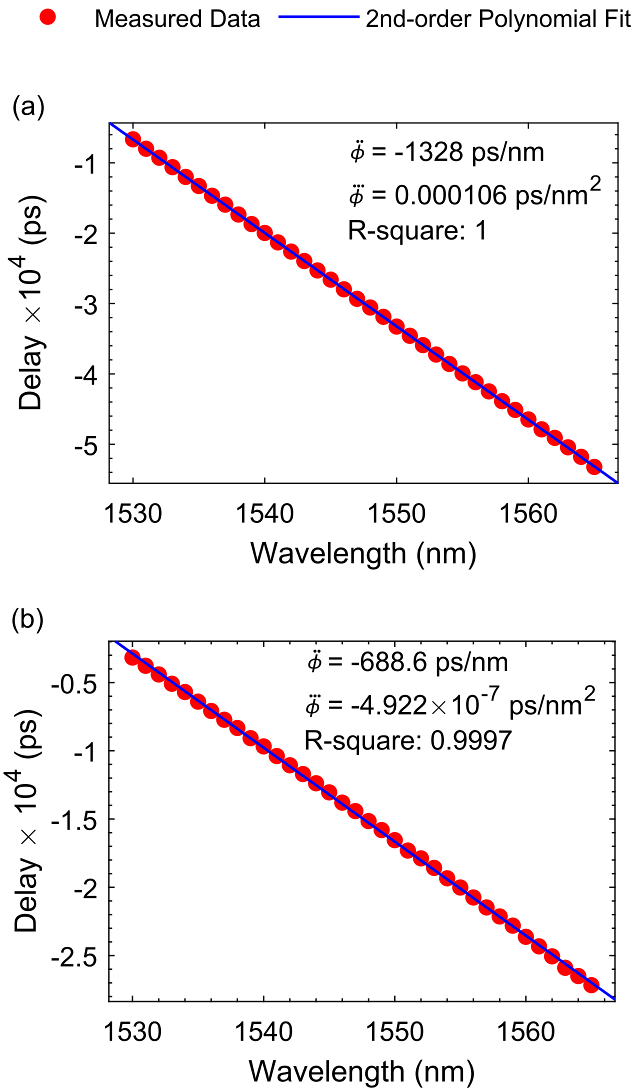

Fig. A1 DCF characterization. (a) DCF1, (b) DCF2.

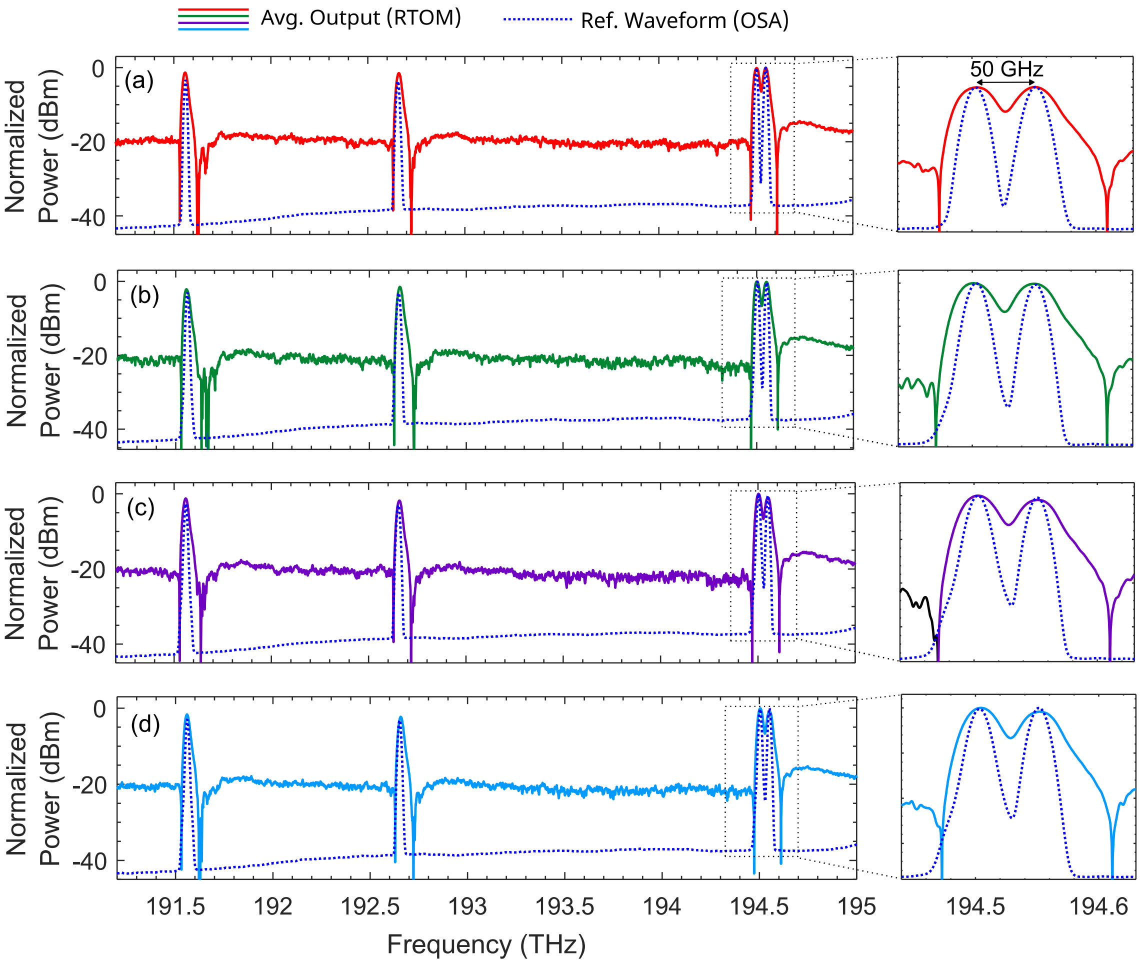

Fig. A2 RTOM spectral analysis across almost the entire C-band.

The SUT is characterized by four WDM channels operating at $\lambda_1 = 1565\ \mathrm{nm}$, $\lambda_2 = 1556.1\ \mathrm{nm}$, $\lambda_3 = 1541.33\ \mathrm{nm}$, $\lambda_4 = 1540.94\ \mathrm{nm}$ with varied modulation formats (MZM, DML, MZM, MZM) and a range of bit rate combinations: (a) 1 Gb/s, 10 Gb/s, 1 Gb/s, 10 Gb/s, (b) 10 Gb/s, 1.25 Gb/s, 10 Gb/s, 1.25 Gb/s, (c) 25 Gb/s, 1.25 Gb/s, 25 Gb/s, 1.25 Gb/s, (d) 25 Gb/s, 5 Gb/s, 25 Gb/s, 5 Gb/s. Temporal sampling is conducted with a period $T_R = 208.7\ \mathrm{ns}$ and time width $\Delta t_p = 100\ \mathrm{ps}$.

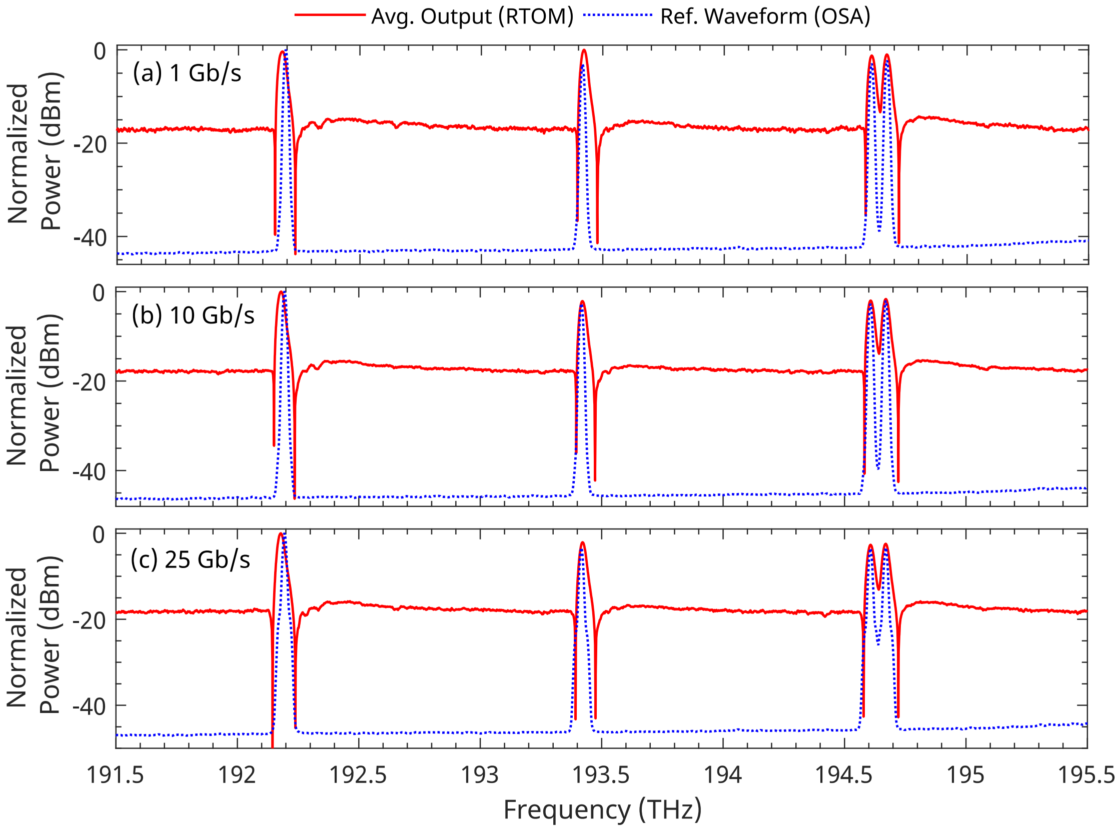

Fig. A3 RTOM trace corresponding to the SUT spanning almost the entire C-band with channels located at different wavelengths.

The SUT consists of four WDM channels located at $\lambda_1 = 1560\ \mathrm{nm}$, $\lambda_2 = 1550\ \mathrm{nm}$, $\lambda_3 = 1540.5\ \mathrm{nm}$, $\lambda_4 = 1540\ \mathrm{nm}$ operating at bit rates of (a) 1 Gb/s, (b) 10 Gb/s, (c) 25 Gb/s. The modulation format of all channels is MZM. Temporal sampling is conducted with a period $T_R = 69.565\ \mathrm{ns}$ and time width $\Delta t_p = 100\ \mathrm{ps}$.

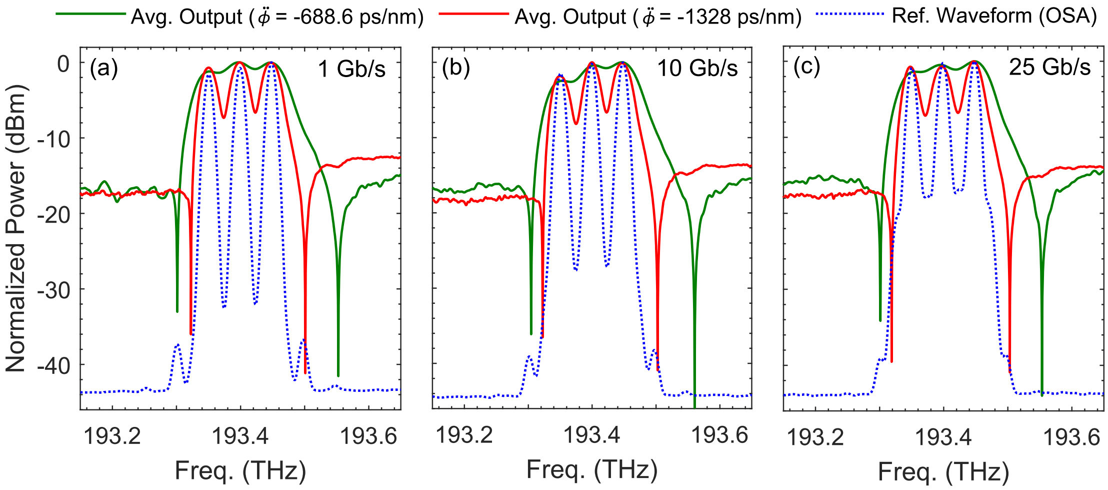

Fig. A4 RTOM trace corresponding to the SUT consisting of three WDM channels with 50 GHz channel spacing under different dispersion values.

The SUT consists of three WDM channels located at $\lambda_1 = 1550.52\ \mathrm{nm}$, $\lambda_2 = 1550.12\ \mathrm{nm}$, and $\lambda_3 = 1549.72\ \mathrm{nm}$ operating at bit rates of (a) 1 Gb/s, (b) 10 Gb/s, (c) 25 Gb/s. The modulation format for all channels is MZM. Temporal sampling is conducted with a period $T_R = 69.565\ \mathrm{ns}$ and time width $\Delta t_p = 100\ \mathrm{ps}$.

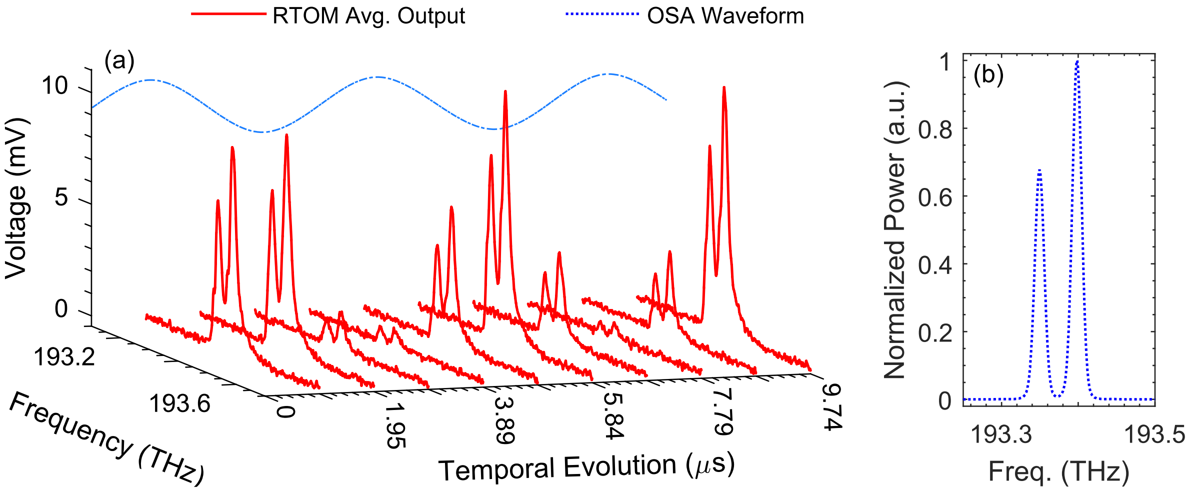

Fig. A5 RTOM waveform obtained for a dynamic SUT changing every 14 samples, with 50 GHz channel spacing.

The SUT consists of two WDM channels located at $\lambda_1 = 1550.52$ nm and $\lambda_2 = 1550.12$ nm operating at a bit rate of 10 Gb/s with MZM modulation format. (a) RTOM output waveform, (b) Waveform obtained from a conventional OSA for all samples. Temporal sampling is conducted with a period $T_R = 69.565$ ns and time width $\Delta t_p = 100$ ps.

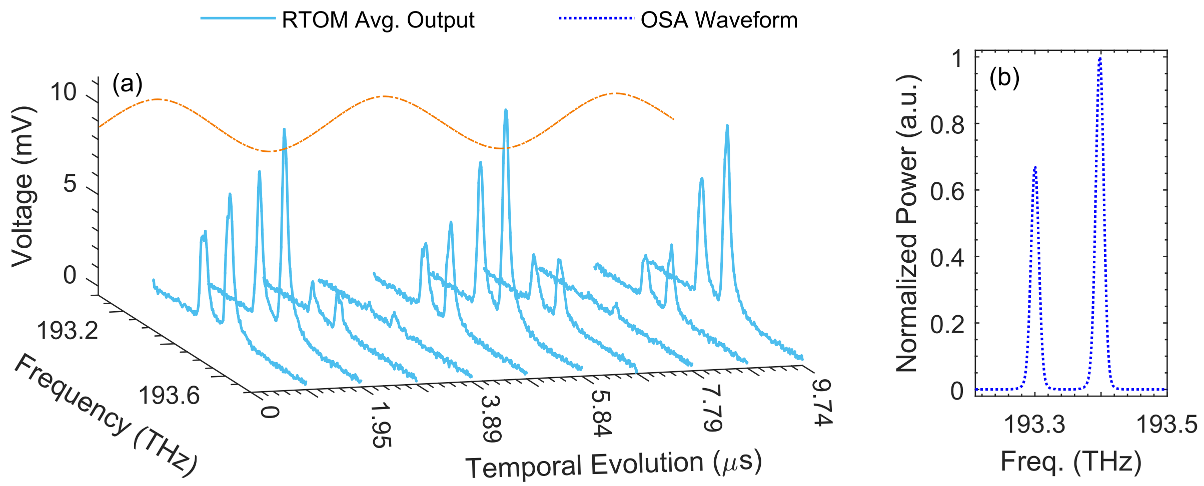

Fig. A6 RTOM waveform obtained for a dynamic SUT changing every 14 samples, with 100 GHz channel spacing.

The SUT consists of two WDM channels located at $\lambda_1 = 1550.92$ nm and $\lambda_2 = 1550.12$ nm operating at a bit rate of 10 Gb/s with MZM modulation format. (a) RTOM output waveform, (b) Waveform obtained from a conventional OSA for all samples. Temporal sampling is conducted with a period $T_R = 69.565$ ns and time width $\Delta t_p = 100$ ps.

Publications

Journal

1. A. Shoeib, M. P. Fernández, C. Rowe, R. Maram, P. Ricciardi, and J. Azaña, "Fiber-optic spectrum monitoring of wavelength-division-multiplexed telecommunication signals with MHz update rates," Optics Letters 49, 1245-1248, 2024.

Conferences

1. A. Shoeib, R. Maram, P. Ricciardi, and J. Azaña, "Real-time Optical Monitoring System Based on Frequency-to-Time Mapping Concept," *in 2023 Photonics North (PN)*, 2023: IEEE, pp. 1-1.
2. A. Shoeib, M. P. Fernández, C. Rowe, R. Maram, P. Ricciardi, and J. Azaña, "Real-time Optical Monitoring of Telecom Data Signals Utilizing Dispersive Fourier Transformation," *in 2023 IEEE Photonics Conference (IPC)*, 2023: IEEE, pp. 1-2.
3. A. Shoeib, M. P. Fernández, C. Rowe, R. Maram, P. Ricciardi, and J. Azaña, "Real-time Monitoring of DWDM Telecom Signals with MHz Update Rate Through Frequency-to-Time Mapping," *in 2024 Conference on Lasers and Electro-Optics (CLEO),* 2024. (accepted)

Patent

1. A. Shoeib, R. Maram, P. Ricciardi, and J. Azaña, " Real-time optical monitoring method and system," U. S. Patent, No. 63/480.371.